

A Study of Order-by-Disorder Phenomenon in Frustrated Magnetic Systems Near Criticality

by

Behnam Javanparast

A thesis
presented to the University of Waterloo
in fulfillment of the
thesis requirement for the degree of
Doctor of Philosophy
in
Physics

Waterloo, Ontario, Canada, 2014

© Behnam Javanparast 2014

I hereby declare that I am the sole author of this thesis. This is a true copy of the thesis, including any required final revisions, as accepted by my examiners.

I understand that my thesis may be made electronically available to the public.

Abstract

Order-by-disorder is the phenomenon of the selection of a long-ranged ordered state by fluctuations in a many-body system. This mechanism, at first sight, seems paradoxical, since fluctuations (disorder) intuitively tend to suppress the order. However, when ObD happens, disorder works in favour of a particular ordered phase. Order-by-disorder can happen where an accidental degeneracy occurs in classical or mean field treatment of a system. These degeneracies, which are not due to exact symmetries of the system, can then be lifted by quantum or thermal fluctuations. The ObD phenomenon is ubiquitous in condensed matter systems with competing or frustrated interactions. Traditionally, the ObD is studied at $T = 0^+$ where the ground state of the system can be selected by quantum fluctuations. The study of ObD at temperature regimes near criticality, $T \lesssim T_c$ where transition happens from the paramagnetic phase to an ordered phase, however, have not received as much attention.

In this thesis, we study the ObD phenomenon in three dimensional frustrated systems close to criticality. We consider 3-component classical Heisenberg spins on pyrochlore lattice and FCC lattice. In the former, the spins interact via a Hamiltonian that can include the most general nearest-neighbour symmetry allowed bilinear interactions, long-range magnetostatic dipole-dipole interaction and second and/or third nearest-neighbour exchange interactions. However, in the latter, the Hamiltonian only consists of long-range magnetostatic dipole-dipole interactions. These two systems, correspond to insulating rare-earth pyrochlore oxides and rare-earth FCC salts. The mean field treatment shows, that accidental $O(4)$ and $U(1)$ symmetries emerge in two different regions of the parameter space of the Hamiltonian of pyrochlore system. While in the FCC system, an accidental $O(3)$ symmetry emerges at the mean field level. We show that fluctuations break these symmetries by respectively introducing cubic (in 4-vector and 3-vector models) and hexagonal anisotropies to the free-energy of the system. To study these system beyond mean field approximation, we use Monte Carlo simulations, spin wave theory and we develop the E-TAP method which is an extended version of the method originally proposed by Thouless, Anderson and Palmer to study fluctuations in spin glasses.

Acknowledgements

My studies at Waterloo provided me with lots of opportunities to learn and grow, personally and intellectually. I would like to express my gratitude to all the people that made this possible.

First, I would like to thank my advisor, Michel J. P. Gingras. His incredible insight, energy, persistence and support motivated me and lit the path that led to this thesis and the corresponding publications. I would like to thank Zihao Hao for stimulating course of collaborations that paved the path in some really sharp turns. I would like to thank Matthew Enjalran and Paul McClarty for their helps with the GTO project, Pawel Stasiak for his kind helps with the Monte Carlo codes, Taoran Lin for our interesting collaboration in muon project and Alexandre Day for exciting discussions and collaboration in ETO-TAP project, the sixth order perturbation, which made my life significantly easier in counting the number of diagrams.

At the end, I would like to give a shout-out to all my friends in Waterloo. You made the grad-life livable.

Dedication

To my family: Maman, Baba and Mona

Table of Contents

List of Tables	x
List of Figures	xi
I	1
I Introductory Matters	1
1 Introduction	2
1.1 Frustration	4
1.2 Order-by-disorder	6
1.3 In this thesis	7
2 Material Review	9
2.1 Rare-earth pyrochlore oxides	9
2.1.1 Isolated CEF ground state	12
2.1.2 Non-isolated CEF ground state	16
2.2 Rare-earth salts with FCC structure	16
3 Methods	21
3.1 Standard mean field theory	21
3.1.1 Direct space s-MFT	22
3.1.2 Reciprocal space s-MFT	23

3.2	Monte Carlo methods	25
3.2.1	Metropolis algorithm	25
3.2.2	Heat bath algorithm	26
3.2.3	Parallel tempering method	28
3.3	Extended TAP method (E-TAP)	29
3.4	Spin wave theory	32
II	Results	35
4	Thermal Selection of Multi-k Partial Order on Pyrochlore Lattice	37
4.1	Introduction	37
4.2	Model and s-MFT treatment	41
4.3	Extended TAP method	45
4.4	Monte Carlo simulations	46
4.5	Discussion	51
5	Emergent $U(1)$ Symmetry Breaking by Thermal Fluctuations – a method exploration	54
5.1	Introduction	54
5.2	Model	56
5.2.1	Ginzburg-Landau (GL) symmetry analysis	58
5.3	E-TAP method and results	61
5.3.1	Method	61
5.3.2	Results	63
5.4	Discussion	64

6	Thermal ObD in $\text{Er}_2\text{Ti}_2\text{O}_7$	67
6.1	Introduction	67
6.2	Model and method	69
6.3	Critical behaviour	71
6.4	Selection of ψ_2 state	74
6.5	Conclusion	77
7	Emergent $O(3)$ symmetry breaking due to fluctuations in a system of point dipoles on FCC lattice	78
7.1	Introduction	78
7.2	s-MFT and GL analysis	79
7.3	The effect of fluctuations	82
7.3.1	Spin wave calculations	82
7.3.2	E-TAP	84
7.3.3	Monte Carlo simulations	84
7.4	Conclusion and future Work	88
8	Conclusion	90
III	APPENDICES	94
A	Pyrochlore Lattice	95
B	Partially Ordered State in s-MFT	97
B.1	Defining primary tools	97
B.2	No crystal electric field	98
B.3	With crystal electric field	101
B.4	Emergent $O(4)$ symmetry up to quartic order in s-MFT	102

C	Second nearest-neighbour effect on the selection of partially ordered states at T_c^{MF}	104
D	ψ_2 and ψ_3 states	107
E	Diagrammatic Approach in E-TAP	108
	E.1 $\langle U^2 \rangle$ calculation	108
	E.2 $\langle U^2 T_2 \rangle$ calculation	110
	E.3 On diagrams	113
F	Transformation Matrix Between Different Representations of mg-Hamiltonian	115
IV	Bibliography	116
	References	117

List of Tables

5.1	Values of a_i in $g_0(j_{\pm\pm}, j_{z\pm})$ multiplied by 10^2	63
5.2	Values of b_j in $g_1(j_{\pm\pm}, j_{z\pm})$ multiplied by 10^4	64
B.1	Spin configurations of a single tetrahedron in $1-\mathbf{k}$ states	97

List of Figures

1.1	Illustration of frustration	5
2.1	Interpenetrating pyrochlore lattices	10
2.2	Oxygen cage around rare-earth site	11
2.3	Illustration of cubic diagonal direction	14
2.4	\hat{d}_{ij} vectors corresponding to DM interaction	15
2.5	Rare-earth FCC salts, illustration of tetrahedral and octahedral environment	18
2.6	Rare-earth FCC salts, DC susceptibility plots	19
4.1	Partially ordered states with $\mathbf{k} = (1/2, 1/2, 1/2)$ propagation vector	38
4.2	Experimental specific heat of $\text{Gd}_2\text{Ti}_2\text{O}_7$	40
4.3	Line degeneracy at critical temperature	42
4.4	Phase diagram of partially ordered states in the anisotropic-couplings parameter space	47
4.5	Monte Carlo results, selection of the partially ordered states	50
4.6	Monte Carlo results, low temperature state	51
4.7	Magnetic diffuse neutron scattering data	52
5.1	Spin configuration of ψ_2 and ψ_3 states	57
5.2	Result of the sixth order E-TAP correction and spin wave calculation	65
6.1	Experimental specific heat of $\text{Er}_2\text{Ti}_2\text{O}_7$	68

6.2	Monte Carlo results: order parameter, its susceptibility and Binder ratio	73
6.3	Monte Carlo results: specific heat and its scaling	75
6.4	Hexagonally anisotropic order parameter	76
7.1	Monte Carlo simulations result by Bouchaud and Zérah	80
7.2	Magnon dispersion, FCC dipolar problem	83
7.3	E-TAP contour plot, FCC dipolar problem	85
7.4	MC-Metropolis-FCC dipolar problem	87
7.5	MC-Heat bath-FCC dipolar problem	89
C.1	T_c soft modes for mg-Hamiltonian with nonzero J_2	106
E.1	The diagram representing $\langle U^2 \rangle$	109
E.2	β^3 and β^4 diagrams that occur in E-TAP expansion	111
E.3	An example of a fused diagram	113

Part I

Introductory Matters

Chapter 1

Introduction

The study of many-body systems is one of the most fascinating areas of physics. It provides us with a rich and compelling playground to explore collective phenomena that emerge from the complicated interactions between the microscopic degrees of freedom associated with the constituents of a system. Although the properties of each building block of a system may be understood separately, their collective behaviour is distinct from the individuals'. In consequence, challenging problems are posed which often promise the discovery of exotic physics accompanied by the development of new problem-solving methods that influences not only the field of condensed matter but also the whole of physics and science in general. Despite their complexity, the behaviour of some of many-body systems can be understood through tractable models that provide milestones towards comprehending more intricate ones. Insulating magnets are one of these types of many-body systems.

Magnetism was discovered in ancient era. But the breakthroughs in explaining this phenomenon was only put forward in the beginning of the twentieth century with the development of quantum mechanics and the discovery of the intrinsic angular momentum (spin) of an electron. The magnetic properties of a solid are directly ascribed to its fundamental building blocks; atoms, molecules or ions where the orbital motion and spin of electrons can generate the magnetic moment¹. In insulating magnetic crystals, the magnetic constituents are ions that sit on an array of lattice sites and interact with each other primarily through an exchange mechanism².

¹Here we focus on electronic magnetic moments and ignore nuclear magnetic moments which are typically smaller in order of magnitude by electron to nuclear mass ratio [1, 2].

²A mechanism to lower the energy of the electrons on neighbouring sites generated by Coulomb repulsion and Pauli's exclusion principle.

In theoretical studies of magnetic materials, a variety of models has been constructed based on this picture³, where different lattice geometries, different types of magnetic moments⁴ and different types of microscopic interactions⁵ have been considered. Although these models may seem too simplistic, they have been successful in explaining the corresponding magnetic phenomena and reproducing basic attributes of real physical systems. In these models, phase transitions are relatively easily studied. The Ising model in two dimensions, was the first exactly solvable model to exhibit a phase transition [3, 4]. Considering the universal behaviour of many-body systems at criticality, magnetic lattice models can be employed as an analogue of more complicated nonmagnetic systems. So not only they are fruitful in the field of magnetism, they can shed light on the broader and more complicated problems of condensed matter physics.

All the above theoretical endeavours go hand in hand with experiments. A multitude of experimental techniques are available to probe both bulk properties by measuring for example, specific heat and magnetic susceptibility, and microscopic properties by performing for instance neutron and X-ray scattering or μ SR⁶ experiments.

Beside the basic science prospects, since insulating magnets fall under the umbrella of magnetic materials, they are the inseparable ingredients in developing modern technologies [5, 6, 7, 8, 9]. In consequence, they can strongly influence our day to day life in the future, which makes the study of their properties worthwhile.

Among insulating magnets, one of the most interesting and abundantly studied cases is that of frustrated systems. In this class of problems the symbiotic relation between theory and experiment is very strong such that, in some cases new experimental avenues are prompted by theoretical proposals. For example the search for materialistic realization of quantum spin liquid is one the best-known examples [10]. This symbiotic relation provides a rich platform for academic research which encourages us to focus on these systems in this thesis.

³Magnetic moments on lattice sites

⁴e.g. Ising, Potts, XY, Heisenberg

⁵e.g. ferromagnetic or antiferromagnetic exchange, magnetostatic dipole-dipole interaction

⁶Muon Spin Resonance/Relaxation/Rotation

1.1 Frustration

Historically⁷, the concept of frustration first appeared in a publication on spin glasses by Toulouse in 1977 [12] and very shortly after by Villain [13]. However, this topic was studied without being labeled as such, in 1935 by Pauling in calculation of the residual entropy of water ice [14] and in 1950 by Houtappel [15] and Wannier [16] in the problem of Ising antiferromagnet on the triangular lattice. Frustration is the inability of a system in minimizing its total classical energy by minimizing all the pairwise interaction energies between each pair of interacting degrees of freedom at the same time [11]. This phenomenon is ubiquitous in many-body systems and in particular, magnets. Frustration can be characterized in two major categories, random and geometrical. Random frustration can happen in two situations; either in a system at thermal equilibrium where there is competition between interacting degrees of freedom that yields modulated spatial correlations e.g. the case of stripes in copper-oxide superconductors [17] or in a system with randomly distributed frozen degrees of freedom, for example the case of magnetic iron atoms in a gold matrix where the interaction between iron ions is mediated by the gold conduction electrons through RKKY⁸ interaction. Geometrical frustration happens when the geometry of the system prevents simultaneous minimization of the energy of all pairwise interactions and can be realized in a lattice made of plaquettes of spins/magnetic moments with odd number of antiferromagnetic exchange interactions. An example of such systems is Ising spins interacting antiferromagnetically via exchange interaction on a triangular lattice with the Hamiltonian:

$$\mathcal{H} = J \sum_{\langle i,j \rangle} S_i S_j. \quad (1.1)$$

Here $J > 0$ for an antiferromagnetic interaction, $S_i = \pm 1$ for Ising spins and i and j are the nearest-neighbour sites on a triangular lattice. The antiferromagnetic interaction energy between nearest-neighbour spins is minimized when they point in opposite directions. On a triangular plaquette, the energy of one of the pairs of spins can not be minimized (see Fig. 1.1). As a result, several configurations can minimize the energy of the plaquette. Since inter-plaquettes interactions are also antiferromagnetic, the classical ground state of the system composed of these plaquettes which is the triangular lattice, possesses an extensive macroscopic degeneracy which grows exponentially with the system size and results in a residual entropy [18]. These degeneracies are accidental rather than a result of symmetries of the Hamiltonian. Thus, they are expected to be lifted by fluctuations

⁷It is said that the phrase "frustration" was first informally brought up by P.W. Anderson at a summer school in Aspen in 1976. [11].

⁸Rudermann-Kittel-Kasuya-Yoshida

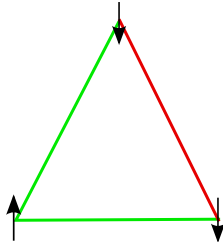


Figure 1.1: Antiferromagnetically coupled spins on a triangle. The red bond is the unsatisfied one.

or perturbative interactions. Antiferromagnetically coupled Heisenberg or Ising spins on triangular lattice, kagome lattice⁹ and pyrochlore lattice¹⁰, are among the most-studied examples of geometrically frustrated systems [18].

In the realm of experiments, a prominent signature of three dimensional frustrated systems is the short-range correlations that manifests themselves by a broad peak of structure factor at a finite wave vector, measured in magnetic neutron scattering [18]. The geometrically frustrated materials generally exhibit a negative Curie-Weiss temperature (Θ_{CW}) which is obtained from the magnetic susceptibility, indicating the presence of antiferromagnetic interactions. In such a case, the system stays paramagnetic even at $T \ll \Theta_{CW}$. Ordering or spin freezing can happen at a lower temperature (T_c) and the degree of frustration is usually qualitatively specified by the ratio $f \equiv |\Theta_{CW}|/T_c$. Another experimental sign of frustration is observation of the residual entropy through specific heat measurements.

Due to the extensive ground state degeneracy, frustrated magnets are expected to exhibit large spin fluctuations which in turn can lead to the emergence of novel short-range ordered states such as spin ice, quantum spin liquids or the exotic phenomenon of order-by-disorder (ObD) in which fluctuations can select a long-range ordered state. Motivated by recent experimental works on the frustrated pyrochlore oxide $Gd_2Ti_2O_7$ [19] and studies on ObD effect in $Er_2Ti_2O_7$ [20, 21], in this thesis, we explore the occurrence of ObD phenomenon.

⁹A network of corner sharing triangles in 2 dimension

¹⁰A network of corner sharing tetrahedra

1.2 Order-by-disorder

Order-by-disorder is the selection of an ordered phase by fluctuations. The concept of order-by-disorder (ObD) was originally proposed by Villain and collaborators as the ordering mechanism in the problem of the two-dimensional frustrated Ising model on a domino lattice [22]. ObD¹¹, at first sight, seems a paradoxical concept since disorder, caused by fluctuations¹², tends to suppress the order in the system. However, when ObD phenomenon happens, fluctuations work in favour of a particular long-range ordered state.

Since the extensive classical degeneracy in frustrated magnets is accidental, the spectrum of fluctuations about different degenerate *ground states* are expected to be different in some cases. When this happens, the ground states with lowest excitation energy have the higher number of zero/soft modes¹³ and as a result higher entropy. Consequently, the system has the tendency to be in a region of the ground state manifold with the highest number of soft modes which in turn lifts the extensive degeneracy. Therefore fluctuations enhance the order in such cases and the ObD phenomenon occurs in the $T \rightarrow 0$ regime. The nature of these fluctuations is thermal at finite but low temperatures ($T = 0^+$) and quantum mechanical at $T = 0$.

ObD can also occur at finite temperatures, *away from the $T = 0^+$ regime*. In this temperature regime, most often the simplest starting point to obtain a qualitative understanding of the essential physics, is the mean field approximation¹⁴. In systems with competing or frustrated interactions, mean field approximation may yield a number of states with *degenerate minimum free energy below the mean-field critical temperature*, T_c^{MF} [24]. These accidental degeneracies, which are not due to exact symmetries of the Hamiltonian describing the interactions, can be lifted by the effects of thermal fluctuations[22] and the ObD phenomena occurs at $T = T_c^-$.

In the previous investigations of the ObD phenomenon, the primary focus had been to identify the mechanism of selection of the *ground state* by taking into account the harmonic quantum spin fluctuations about a classical long-range ordered states [20, 21, 25, 26, 27, 28, 29, 30, 31]. However, the problem of the selection by ObD mechanism at temperatures near the critical temperature has not received as much attention. In this thesis we focus on this temperature regime. Although there has been some numerical

¹¹ObD phenomenon is also realized in the context of ultra-cold-atom systems where an impurity potential through Anderson localization mechanism creates disorder which leads to order [23].

¹²Ignoring the disorder originating from impurities and crystal defects

¹³A certain organized motion of spins which costs zero energy

¹⁴A method that replaces the many-body problem with a simpler problem of a one-body system interacting with an averaged field. The corresponding details are discussed in Chapter 3.

studies on the ObD at $T \lesssim T_c$ [20, 30, 32, 33], an analytical study specifying the role of the microscopic interactions in the ObD mechanism in this temperature regime has, to the best of our knowledge, not yet been pursued and is of considerable interest. In principle, the long-range order selected by ObD can be different for $T = 0^+$ and $T \lesssim T_c$ regimes. This occurs, for example, in the case of Heisenberg spins on the pyrochlore lattice interacting via nearest-neighbour antiferromagnetic exchange and indirect Dzyaloshinskii-Moriya interaction¹⁵ [34]. There are interesting cases in which the ObD mechanism is at play only in the selection of the long-range ordered state at $0 \ll T \lesssim T_c$ regime [35]. Consequently, from a fundamental viewpoint, it is thus highly desirable to study the role of fluctuations beyond s-MFT at temperatures close to the critical region ($T = T_c^-$).

1.3 In this thesis . . .

In this thesis, we investigate the problem of ObD away from the $T = 0^+$ regime. We focus on two types of frustrated models: anisotropic Heisenberg spins on a pyrochlore lattice and dipolar Heisenberg spins on face-centred-cubic (FCC) lattice. These models are used to study the magnetic rare-earth pyrochlore oxides [11] and the rare-earth FCC salts [36], respectively. We show that, in these systems, accidental $U(1)$, $O(3)$ and $O(4)$ symmetries emerge at the level of a mean field approximation. We then study how thermal fluctuations can break these symmetries in the $T \lesssim T_c$ regime by introducing hexagonal and cubic anisotropy terms in the free-energy of the system.

The rest of the thesis is organized as follows. In Chapter 2, we review the properties of rare-earth pyrochlore oxides and rare-earth FCC salts as potential platforms for exhibiting ObD phenomenon. In Chapter 3, we review the methods we used in this thesis to tackle the problem of ObD in different temperature regimes.

We then continue to present the results of our investigations in Part II of the thesis.

In Chapter 4, we study the emergence of $O(4)$ symmetry in the mean field theory treatment of the most general bilinear Hamiltonian on the pyrochlore lattice (referred to as mg-Hamiltonian, for brevity). We show how thermal fluctuations break this accidental symmetry which occurs in a certain region of the parameter space of the mg-Hamiltonian, by introducing a cubic anisotropy. The work presented in this chapter is motivated by the peculiar ordered phase of the rare-earth oxide compound $\text{Gd}_2\text{Ti}_2\text{O}_7$ [19].

¹⁵An antisymmetric, anisotropic exchange interaction between two spins on a lattice bond with no point of inversion that is induced by spin-orbit coupling.

In Chapter 5, we investigate the ObD phenomenon in a different region of the parameter space of mg-Hamiltonian where in the mean field approximation, a $U(1)$ accidental symmetry emerges. We study how thermal fluctuations can break this symmetry that exists at mean field level, by introducing a hexagonal anisotropy which we explore at $T = T_c^-$. This study was motivated by recent investigations on the rare-earth oxide $\text{Er}_2\text{Ti}_2\text{O}_7$ [20, 21, 30, 32, 33]. In Chapter 6, we focus on the mg-Hamiltonian with its coupling constants tuned to the ones corresponding to $\text{Er}_2\text{Ti}_2\text{O}_7$ amended by long range dipolar interactions and we explore its critical properties and the ObD selection at $T = T_c^-$ via Monte Carlo simulations.

In Chapter 7, we investigate the emergence of the $O(3)$ symmetry at the level of mean field approximation in a system of point dipoles on a FCC lattice. We show how thermal and quantum fluctuations break this symmetry by introducing a cubic anisotropy.

Finally, in Chapter 8, we offer concluding remarks of the thesis.

Chapter 2

Material Review

In this chapter we briefly review two groups of magnetically frustrated materials that are potential platforms for the realization of the ObD phenomenon.

2.1 Rare-earth pyrochlore oxides

Rare-earth pyrochlore oxides are magnetic materials with the chemical formula $R_2^{3+}M_2^{4+}O_7$. R^{3+} and M^{4+} ions form two distinct interpenetrating pyrochlore lattices; a structure of corner sharing tetrahedra¹ (See Fig. 2.2).

R^{3+} , M^{4+} or both can be magnetic in these compounds. To proceed, we consider the cases where only the R^{3+} ions are magnetic, for example R can be Gd, Tb, Dy, Ho, Er, Yb and M^{4+} ions are non-magnetic transition metals for instance, M =Ti. Since we are interested in the magnetic properties of these systems, we focus on the pyrochlore lattice formed by R^{3+} ions. If the nearest-neighbour exchange interaction between R^{3+} ions is antiferromagnetic, these systems are highly frustrated. We also note that in all these cases, the compound is insulating.

To continue, we consider the single-ion properties of R^{3+} . In rare-earth ions, the spin-orbit interaction (SOI) is large² and is given by

$$\mathcal{H}_{\text{SO}} = \pm\zeta(LS)\mathbf{S} \cdot \mathbf{L}, \quad (2.1)$$

¹One can also view the pyrochlore lattice as a non-Bravais lattice that consist of a tetrahedral basis on the FCC lattice sites.

²Of the order of several 10^3 K [37]

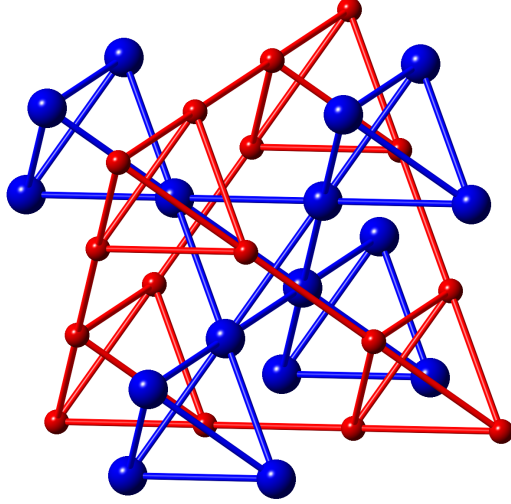


Figure 2.1: The blue and red spheres form two distinct network of corner-sharing tetrahedra which are interpenetrating.

where $+$ and $-$ respectively corresponds to a less or more than half-filled f -subshells and ζ is determined by a radial integral corresponding to the $4f$ subshell³. As a result, the total angular momentum $\mathbf{J} = \mathbf{L} + \mathbf{S}$ is the good quantum number. The values of L and S in Eq. (2.1), the orbital and spin angular momentum of the ion's lowest-energy state, respectively, are determined by Hund's first two rules. The $(2L + 1)(2S + 1)$ -degeneracy of this lowest-energy state is lifted by SOI and the ground state has total angular momentum of $J = |L - S|$ or $J = L + S$ for less than or more than half-filled $4f$ shell, respectively. The excited states⁴ are well separated from the ground state [37]. As a result, in the low energy regime⁵, that we are interested, the physical properties of the R^{3+} ion is determined by the SOI ground state.

Each R^{3+} ion in a $R_2M_2O_7$ compound is surrounded by an oxygen cage; a cube that is distorted along the local $[111]$ directions (see Fig. 2.3). This cage creates a crystal electric

³ $\zeta(LS) = (\pi/m^2c^2S) \int rR_{4f}^2(r)(dv/dr)dr$ where c is the speed of light, m is the mass of electron, R are the radial wavefunctions corresponding to $4f$ shell and v is the effective potential including Hartree, exchange-correlation and external potentials [37]

⁴with total angular momentum $|L - S| < J \leq L + S$ or $|L - S| \leq J < L + S$ depending on the number of electrons in the $4f$ shell.

⁵corresponding to low temperatures of order of 1 K

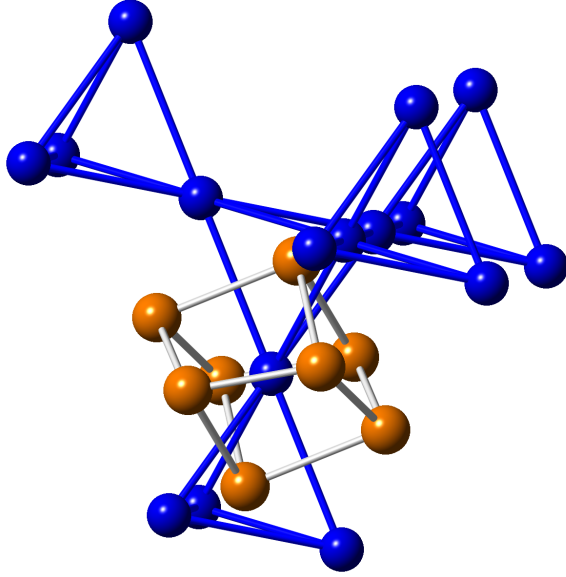


Figure 2.2: The orange spheres represent the closest oxygen ions to a rare-earth site (blue sphere) in $R_2M_2O_7$ compound, which form a cage (a distorted cube) and create the crystal electric field. Note that the two oxygen ions at the centre of the tetrahedra are closer to the rare-earth site than the others.

field (CEF) given by

$$\mathcal{H}_{\text{CEF}} = \sum_i \sum_{l,m} B_l^m O_l^m(\mathbf{J}_i). \quad (2.2)$$

$O_l^m(\mathbf{J}_i)$ are Stevens' operator equivalents which consist of polynomial functions of components of total angular momentum operator, J_{iz} and $J_{i\pm} \equiv J_{ix} \pm J_{iy}$ [38]. Due to the D_{3d} point symmetry of the pyrochlore lattice, the allowed terms in \mathcal{H}_{CEF} are the ones with $l = 2, 4, 6$ ⁶ [11]. The CEF lifts the $2J + 1$ -fold degeneracy of the SOI ground state with total angular momentum of J . Thus, the low energy properties of R^{3+} single-ion is dictated by the CEF energy spectrum.

Equipped with the knowledge of single-ion energy levels, we now review the possible interactions between the magnetic ions in rare-earth pyrochlore oxides. The inter-ionic interactions of R^{3+} ions on the pyrochlore lattice are complicated [39] especially compared to $3d$ transition metal ion systems with often a relatively simple spin-only exchange Hamil-

⁶The space group of pyrochlore lattice is $Fd\bar{3}m$.

tonian of the form $\mathcal{J}\mathbf{S}_i \cdot \mathbf{S}_j$. In $R_2M_2O_7$ compounds, the partially-filled $4f$ subshells are strongly shielded by the $5s$, $5p$ and $5d$ subshells. As a result, the orbital overlap is reduced and direct exchange or superexchange interactions are not dominant [11]. The ion-ion interactions then have multiple origins: direct classical electric and magnetic multipole interactions, direct exchange or superexchange electric and magnetic multipole interactions and lattice-mediated electric multipole interactions [40]. Thus, Ω_{ij} , the microscopic couplings between ions at lattice site i and j , is very complicated. In principle, the microscopic Hamiltonian of a system of $4f$ ions can be written in terms of the Stevens' operator equivalents $O(\mathbf{J}_i)$. However, the couplings Ω_{ij} are tremendously difficult to determine, both theoretically and experimentally, due to complex nature of $O(\mathbf{J}_i)$, $O(\mathbf{J}_j)$ and Ω_{ij} itself [39]. Depending on whether CEF ground state is isolated, this complicated situation can be simplified to a great extent which we review in the next two sections.

2.1.1 Isolated CEF ground state

In $R_2M_2O_7$ series the ground state wavefunction is usually doubly degenerate [39]. If the energy gap between the CEF ground state doublet and the first excited states is significantly larger than the Ω_{ij} ⁷, the low energy magnetic properties of the system is only dictated by the CEF *isolated* ground state wavefunction and is determined by considering the Zeeman energy⁸. For argument's sake, we label the ground state doublets as $|1\rangle$ and $|2\rangle$. The matrix elements of \mathbf{J}_i in this doubly degenerate subspace of CEF wavefunctions determine the low temperature behaviour of R^{3+} ion. It can lead to Ising-like behaviour of the magnetic moments if the only nonzero matrix elements are $\langle j|J_i^z|j\rangle$ with $j = 1, 2$ which is the case for Dy^{3+} in $\text{Dy}_2\text{Ti}_2\text{O}_7$ [11]. On the other hand, if $\langle 1|J^\alpha|2\rangle \neq 0$ with $\alpha = x, y$, the low energy behaviour of the R^{3+} ion is expected to be XY -like such as the behaviour of Er^{3+} magnetic moments in $\text{Er}_2\text{Ti}_2\text{O}_7$ [11]. The low energy Hamiltonian, \mathcal{H}_{int} , can be obtained by the use of degenerate perturbation theory and can be simply written as [39]

$$\begin{aligned} \mathcal{H}_{\text{int}} = \mathcal{H}_{\text{nn}} \equiv & \sum_{\langle i,j \rangle} [\mathcal{J} \mathbf{S}_i \cdot \mathbf{S}_j + \mathcal{J}_{\text{DM}} \hat{d}_{ij} \cdot (\mathbf{S}_i \times \mathbf{S}_j) \\ & + \mathcal{J}_{\text{Ising}} (\mathbf{S}_i \cdot \hat{z}_i)(\mathbf{S}_j \cdot \hat{z}_j) + \mathcal{J}_{\text{pd}} S_i^\alpha \Lambda_{ij}^{(\alpha\beta)} S_j^\beta], \end{aligned} \quad (2.3)$$

where \mathbf{S}_i is the pseudo-spin $1/2$ expressed in global coordinate system and is representing the ground state doublet. $S_i^\mu \equiv (1/2g_J) \sum_\nu \tilde{g}_i^{\mu\nu} \sigma_i^\nu$ where g_J is the Landé factor of the R^{3+}

⁷Of the order of 10^3 larger [39]

⁸ $-g_J\mu_B \sum \mathbf{J}_i \cdot \mathbf{B}$ where g_J is the Landé factor, μ_B is the Bohr magneton and \mathbf{B} is an external magnetic field.

ion of interest, σ_i are the Pauli matrices⁹ and $\tilde{g}_i^{\mu\nu}$ is an element of the g tensor defined below, in global coordinate system. g tensor captures the anisotropy of the CEF ground state and is initially defined in local [111] direction on each sublattice of pyrochlore lattice (see Fig. 2.3 and Appendix A). g tensor is diagonal in these local coordinate systems and its elements are defined as: $g^{xx} = g^{yy} = 2g_J\langle 1|J^\alpha|2\rangle$ with $\alpha = x$ or y and $g^{zz} = 2g_J\langle i|J^z|i\rangle$ with $i = 1$ or 2 . \tilde{g} can be obtained by rotating g from local coordinates to global coordinates using the directions defined in Appendix A.

\mathcal{H}_{nn} includes all possible symmetry-allowed nearest-neighbour (n.n.) bilinear interactions on the pyrochlore lattice: isotropic exchange (\mathcal{J}), Dzyaloshinskii-Moriya (DM) (\mathcal{J}_{DM})¹⁰, Ising ($\mathcal{J}_{\text{Ising}}$) and pseudo-dipolar (\mathcal{J}_{pd}) [41, 42]. The couplings $\{\mathcal{J}, \mathcal{J}_{\text{DM}}, \mathcal{J}_{\text{Ising}}, \mathcal{J}_{\text{pd}}\}$ can be positive or negative in general. Unit vectors \hat{d}_{ij} are determined based on the symmetries of the pyrochlore lattice and Moriya's rules and are chosen such that positive and negative \mathcal{J}_{DM} indicate direct and indirect DM interactions, respectively [43] (see Fig. 2.4). \hat{z}_i is the local cubic [111] direction (see Fig. 2.3) at site i and $\Lambda_{ij}^{(\alpha\beta)} \equiv (\delta_{\alpha\beta}/r_{\text{nn}}^3 - 3r_{\text{nn};\alpha}r_{\text{nn};\beta}/r_{\text{nn}}^5)$ where r_{nn} is the nearest-neighbour distance in pyrochlore lattice. The Hamiltonian in Eq. (2.3) can be written using different conventions [44, 45] one of which we present in Chapters 5, 6. We note that depending on the CEF ground state wavefunctions, some of the above terms may not be present in the Hamiltonian, for example for Dy^{3+} in $\text{Dy}_2\text{Ti}_2\text{O}_7$, the only nonzero coefficient is $\mathcal{J}_{\text{Ising}}$. However, for Er^{3+} in $\text{Er}_2\text{Ti}_2\text{O}_7$ all the coefficients are present.

Since R^{3+} ions possess a large magnetic moment and shielded $4f$ subshells, the magnetostatic dipole-dipole interaction energy scale is comparable to the energy scale of the interactions in Eq. (2.3) and needs to be considered in \mathcal{H}_{int} . As a result the full effective low-energy interaction Hamiltonian can be written as:

$$\mathcal{H}_{\text{int}} = \mathcal{H}_{\text{nn}} + \mathcal{H}_{\text{dip}}, \quad (2.4)$$

where

$$\mathcal{H}_{\text{dip}} = \mathcal{J}_{\text{dip}} \sum_{i,j} \mathbf{S}_i \cdot \mathbf{S}_j / r_{ij}^3 - 3(\mathbf{S}_i \cdot \mathbf{r}_{ij})(\mathbf{S}_j \cdot \mathbf{r}_{ij}) / r_{ij}^5. \quad (2.5)$$

Here, \mathbf{r}_{ij} is the position vector connecting sites i and j in the pyrochlore lattice. $\mathcal{J}_{\text{dip}} = \mu_0\mu_B^2/4\pi r_{\text{nn}}^3$, where r_{nn} is the nearest-neighbour distance in pyrochlore lattice. r_{ij} is measured in units of r_{nn} and μ_B is the Bohr magneton.

⁹Which we replace with unit vectors along global three Cartesian directions in the classical limit.

¹⁰An antisymmetric, anisotropic exchange interaction between two spins on a lattice bond with no point of inversion that is induced by spin-orbit coupling.

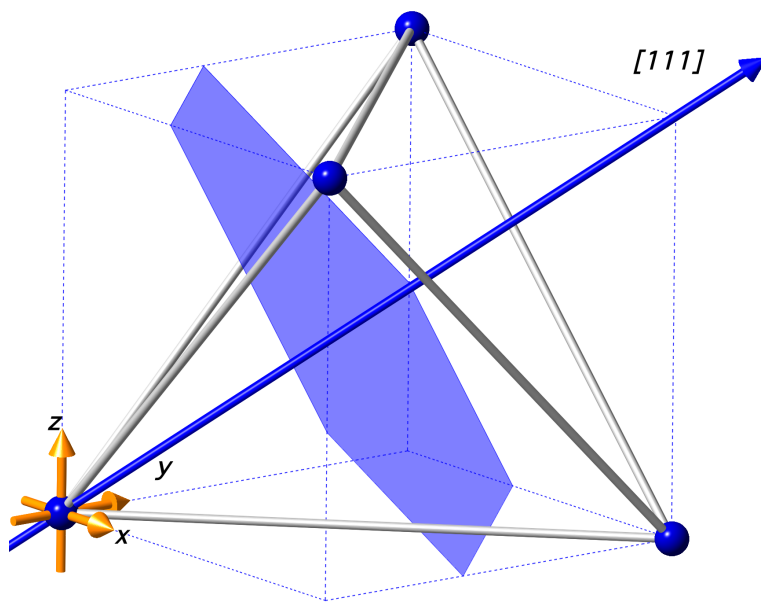


Figure 2.3: $[111]$ cubic direction, the so-called the local $[111]$ direction, (blue arrow) and the plane perpendicular to it, the so-called local xy plane, (blue plane) are specified for one of the sites on a tetrahedron. The orange arrows show cubic x , y and z directions.

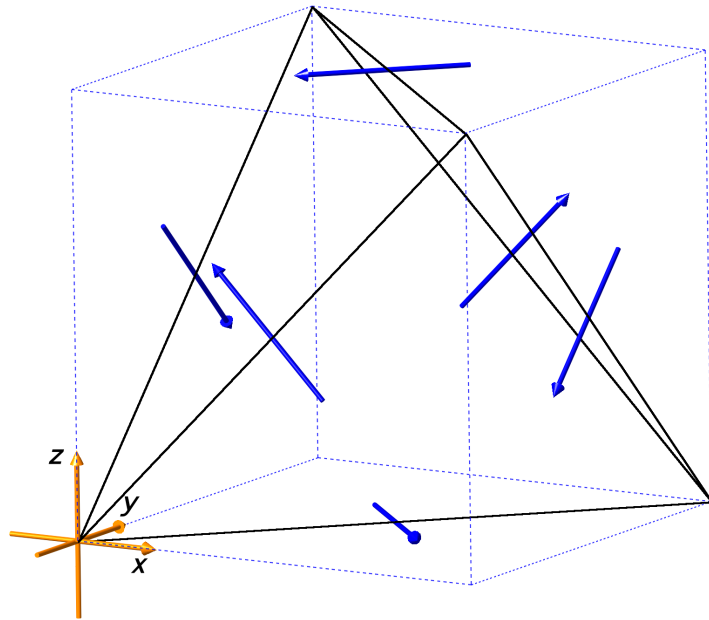


Figure 2.4: \hat{d}_{ij} vectors (blue arrow) are illustrated for indirect DM interaction on a single tetrahedron. The orange arrows show cubic x , y and z directions

2.1.2 Non-isolated CEF ground state

It is also possible that the CEF ground state is not isolated i.e. the energy gap between excited states and the ground state is not significantly large compared to Ω_{ij} [11]. $\text{Tb}_2\text{Ti}_2\text{O}_7$ is an example of such case. The low energy effective Hamiltonian of $\text{Tb}_2\text{Ti}_2\text{O}_7$ is then influenced by the ground state and the excited states [46]¹¹. As a result, the situation can be far more complicated compared to the case of isolated CEF ground state. However, in order to make progress in such cases, one starts by considering the minimal form of \mathcal{H}_{int} which includes the isotropic spin-spin exchange interaction and long-range dipolar interaction. The full Hamiltonian in this case must include CEF and is given by:

$$\mathcal{H} = \mathcal{H}_{\text{CEF}} + \mathcal{H}_{\text{int}}, \quad (2.6)$$

where

$$\mathcal{H}_{\text{int}} = \mathcal{J} \sum_{\langle i,j \rangle} \mathbf{J}_i \cdot \mathbf{J}_j + \mathcal{H}_{\text{dip}}. \quad (2.7)$$

\mathcal{H}_{dip} is the long-range dipolar interaction in Eq. (2.5) in which \mathbf{S}_i is replaced with \mathbf{J}_i . In the case of $\text{Tb}_2\text{Ti}_2\text{O}_7$, since \mathcal{H}_{int} is smaller compared to \mathcal{H}_{CEF} , \mathcal{H}_{int} was treated as perturbation in order to investigate the the low temperature properties of this compound [46].

Another example of non-isolated CEF ground state is Gd^{3+} ions in $\text{Gd}_2\text{Ti}_2\text{O}_7$. This is a special case since the orbital angular momentum of Gd^{3+} is zero which makes its CEF energy scale significantly smaller than most of the $R_2M_2O_7$ compounds [48]. Consequently, as the first approximation, CEF effect in this material can be neglected and one may use the Eq. (2.3) along with long-range dipolar interaction Hamiltonian as the starting point. However, the pseudo-spins \mathbf{S}_i will be replaced by \mathbf{J}_i the total angular momentum since there is no isolated CEF doublet and no perturbation theory is applied as in the case of isolated CEF. We present such an approach in Chapter 4.

To continue, we review another class of frustrated materials in which ObD mechanism is at play.

2.2 Rare-earth salts with FCC structure

Rare-earth ions in salts with the chemical formula $\text{Cs}_2\text{NaR}(\text{NO}_2)_6$ [49] and $\text{Cs}_2\text{NaR}(\text{Cl})_6$ (also known as elpasolite)[50] where R is a rare-earth element of lanthanide series, form a

¹¹This effect combined with spin-lattice coupling makes $\text{Tb}_2\text{Ti}_2\text{O}_7$ one of the most challenging compounds to study in rare-earth pyrochlore oxides series [47].

face centred cubic (FCC) lattice¹² where R^{3+} ions in these compounds possess perfect tetrahedral and octahedral symmetries, respectively¹³ (see Fig. 2.5). The nearest-neighbour distance between R^{3+} ions in both groups of compounds, is large¹⁴ which makes the exchange interactions between different nearest-neighbour ions so weak that the primary form of interaction between these ions is the magnetostatic long-range dipole-dipole interaction and exchange interactions are negligible in comparison [36, 50]. It has been shown experimentally that $\text{Cs}_2\text{NaR}(\text{NO}_2)_6$ with $R = \text{Gd}, \text{Nd}, \text{Dy}$ and Er and $\text{Cs}_2\text{NaR}(\text{Cl})_6$ with $R = \text{Dy}, \text{Er}$ order ferromagnetically at approximately 0.1 K and 0.03 K, respectively [36, 50]. We focus on these compounds.

In order to write a proper Hamiltonian for these compounds, we first recall the hierarchy of energy scales for rare-earth ions discussed above in Section 2.1. We then consider their crystal electric field (CEF) which based on the tetrahedral and octahedral symmetry of the rare-earth sites (see Fig. 2.5), has general form of

$$\mathcal{H}_{\text{CEF}}^{\text{FCC-tetra}} = B_4^0(O_4^0 + 5O_4^4) + B_6^0(O_6^0 - 21O_6^4) + B_6^2(O_6^2 - O_6^6), \quad (2.8)$$

and

$$\mathcal{H}_{\text{CEF}}^{\text{FCC-octa}} = B_4^0(O_4^0 + 5O_4^4) + B_6^0(O_6^0 - 21O_6^4), \quad (2.9)$$

respectively. Here, B_m^n , $m = 4, 6$ and $n = 0, 2$ are constants and O_m^n are Stevens' operator equivalents. B_m^n coefficients can be determined by fitting the susceptibility calculated by point charge approximation, to the experimental results¹⁵ [49, 50].

The magnetic properties of the rare-earth ion depends on the energy spectrum of the CEF. Based on the point charge calculations and pure symmetry arguments, the g tensor corresponding to the CEF ground state of the rare-earth ion in each of the salts, can be determined [49]. Whether the CEF ground state is isolated or not, is then determined by measuring the DC susceptibility of the desired compound. If the low temperature, i.e. $T \approx T_c$, behaviour of DC susceptibility could be solely explained by the CEF ground state and the g tensor corresponding to the ground state is isotropic, the R^{3+} ion can be represented by isotropic Heisenberg spin.

Among the above salts that undergo ferromagnetic transition, an example with isotropic isolated CEF ground state is $\text{Cs}_2\text{NaR}(\text{Cl})_6$ with $R = \text{Dy}$. The DC susceptibility of this ion

¹²Elpasolite compounds, when R is a lighter rare-earth element, undergo a crystalline phase transition below the room temperature. So in this work we focus on the ones that do not experience such a phase transition.

¹³The space group of $\text{Cs}_2\text{NaR}(\text{NO}_2)_6$ and $\text{Cs}_2\text{NaR}(\text{Cl})_6$ are $Fm\bar{3}$ and $Fm\bar{3}m$, respectively.

¹⁴About 7.8 Å [36] which is almost two times larger than the nearest-neighbour distance in $R_2M_2O_7$ compounds.

¹⁵They can also be calculated using Electron Paramagnetic Resonance technique [51, 52].

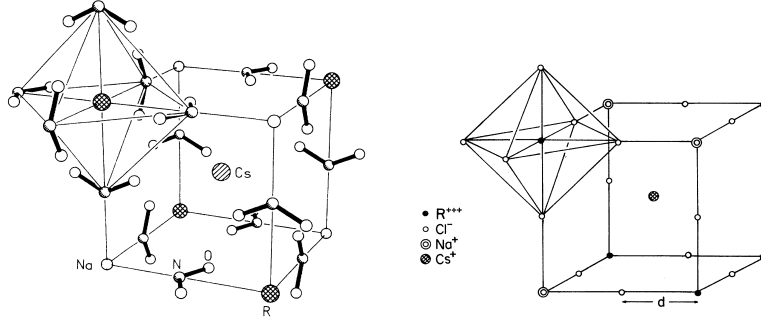


Figure 2.5: **Left:** Reproduced from Ref. [49]. Tetrahedral environment of the rare-earth ion in $\text{Cs}_2\text{NaR}(\text{NO}_2)_6$ compounds. **Right:** Reproduced from Ref. [53]. Octahedral environment of rare-earth ion in $\text{Cs}_2\text{NaR}(\text{Cl})_6$.

presented in Fig. 2.6-top, shows that around the ferromagnetic transition temperature the isotropic CEF ground state can be considered isolated. Although Ref. [50] classifies the $\text{Cs}_2\text{NaR}(\text{Cl})_6$ with $R = \text{Er}$ as an isotropic dipolar ferromagnet, Er^{3+} does not possess an isotropic g tensor corresponding to its CEF ground state. Perhaps further experiments are required to clarify the details regarding this compound.

Another example among the ferromagnetic FCC salts that can be represented by Heisenberg spins on FCC lattice is $\text{Cs}_2\text{NaGd}(\text{NO}_2)_6$ which is an exception of the above rule in terms of CEF energy spectrum. The susceptibility of Gd^{3+} ions in this compound is featureless and approaches the free ion behaviour at low temperatures (see Fig. 2.6-bottom), which is expected since Gd^{3+} possesses zero orbital angular momentum and in consequence weak CEF parameters. So all the above considerations to determine isolated isotropic CEF ground state do not apply to Gd FCC salt. However, based on the fact that Gd^{3+} behaves as a free ion, this material is another example of isotropic Heisenberg spins on FCC lattice [49].

We recall that the primary interaction between R^{3+} ions in rare-earth FCC salts is the long range dipolar interaction. In consequence, the Hamiltonian reads

$$\mathcal{H}^{\text{FCC}} = \mathcal{J}_{\text{dip}} \sum_{i,j} \frac{\mathbf{S}_i \cdot \mathbf{S}_j}{r_{ij}^3} - \frac{3(\mathbf{S}_i \cdot \mathbf{r}_{ij})(\mathbf{S}_j \cdot \mathbf{r}_{ij})}{r_{ij}^5}. \quad (2.10)$$

Here, \mathbf{r}_{ij} is the position vector connecting sites i and j in the FCC lattice. Rare-earth FCC salts are the first realization of a cubic dipolar system that exhibit ferromagnetic order, confirming the theoretical investigations predicting that purely dipolar interactions

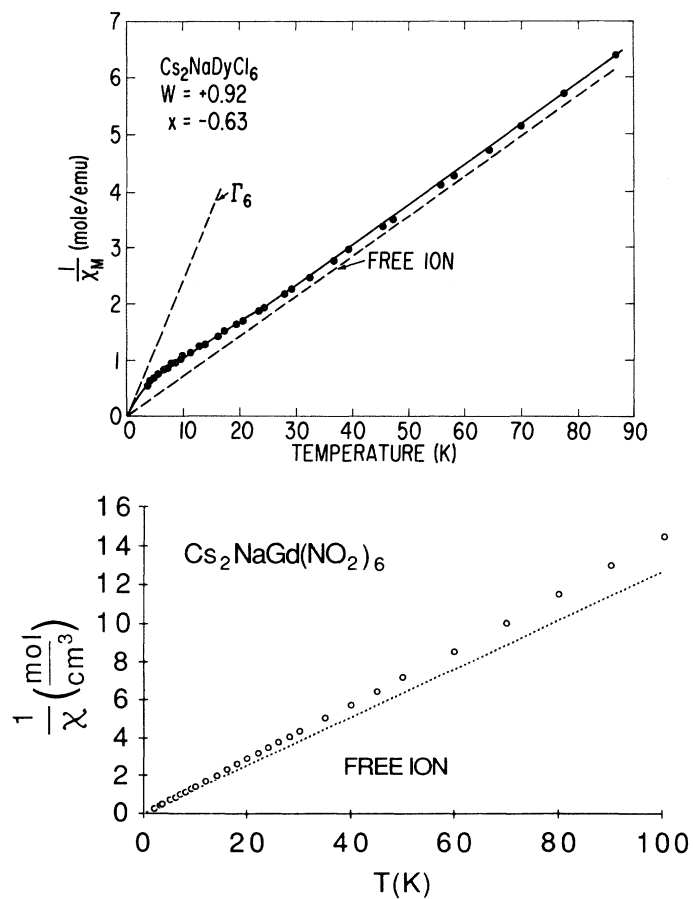


Figure 2.6: **Top:** Reproduced from Ref. [53]. Calculated (solid line) and measured (dots) susceptibility of $\text{Cs}_2\text{NaDy}(\text{Cl})_6$. Γ_6 represents the CEF ground state wavefunction. The susceptibility at low temperatures is only determined by the CEF ground state. **Bottom:** Reproduced from Ref. [49]. DC susceptibility of $\text{Cs}_2\text{NaGd}(\text{NO}_2)_6$ (circles) versus free ion susceptibility of Gd^{3+} . At low temperatures they converge.

on FCC lattices result in a ferromagnetic ground state¹⁶ [36]. These systems are the first examples of non-quantum mechanical/non-exchange ferromagnetism¹⁷.

In this thesis, we study the model of Eq. (2.10). We show that this model at the mean field level approximation possesses an accidental $O(3)$ symmetry. A particular direction of magnetization is then selected by an ObD mechanism. The details of our study are presented in Chapter 7.

In the next chapter, we review the methods we employ in this thesis to detect and investigate the ObD phenomenon in the frustrated systems which we reviewed in this chapter.

¹⁶Purely dipolar interaction on BCC lattice also has a ferromagnetic ground state. However, this does not occur for SC lattice [36]

¹⁷We note that a system of cobalt and nickel nanoparticles about 200-300 Å and 340 Å in size, respectively, arranged in a FCC lattice [54, 55] may also be represented by the Eq. (2.10) as their minimal Hamiltonian. Each site of this FCC lattice is occupied by a nanoparticle which is ordered ferromagnetically in its bulk and may minimally be represented by a point dipole. However, it was shown in Ref. [54] that the surface effects in each nanoparticle introduces an anisotropy field. As a result, a single-site anisotropy term needs to be included in the Hamiltonian of these systems [54]. The study of Eq. (2.10) may be viewed as the first step towards considering an anisotropic Hamiltonian for this class of materials.

Chapter 3

Methods

In this chapter we review the methods we have developed and/or used in this thesis. The application of each of these methods in specific problem are discussed in Part II of the thesis.

3.1 Standard mean field theory

The idea of *mean field approximation* was put forward first by van der Waals in 1873 to develop a liquid-gas equation of state. Later on, in 1907, Weiss applied the same concept to the problem of ferromagnetism. We refer to this approximation as standard mean field theory (s-MFT). In its simplest form, s-MFT replaces a many-body problem with a one-body problem interacting with an averaged field resulting from the interaction with other particles in the system. In this process the fluctuations about the averaged field are neglected and, as a result, s-MFT fails to adequately address the critical behaviour of condensed matter systems close to a phase transition or to predict spin waves at low temperatures. Despite its quantitative drawbacks, in the study of condensed matter systems, s-MFT is often the starting point to capture the basic physical properties of a system before applying more intricate methods.

There are several ways of implementing s-MFT in condensed matter problems. In this thesis we employ two of the simplest forms of the s-MFT in the context of insulating magnetic systems: direct space s-MFT and reciprocal space s-MFT. The former method results in the configuration of the magnetic moments in the direct space at different temperatures which in turn leads to a determination of the transition temperature. Direct space s-MFT

is particularly useful in cases where the system goes through multiple phase transitions at different temperatures. On the other hand, reciprocal space s-MFT provides a recipe to directly evaluate the mean field transition temperature from the paramagnetic phase to the ordered phase, T_c , the normal modes that become soft¹ at $T = T_c$ and their propagation wave vector. However, this method is not suitable to detect multiple phase transitions at low temperatures because it determines soft modes at T_c [56]. We employ both of these methods to achieve better initial assessment of the problems we aim to solve. In what follows we review the details corresponding to these two methods and consider, classical 3-component Heisenberg spins in the systems of interest.

3.1.1 Direct space s-MFT

We proceed to apply the s-MFT approximation to the spin models of interest presented in Chapter 2, all of which can be written in the following general form:

$$\mathcal{H} = \frac{1}{2} \sum_{i,j} \sum_{\mu\nu} S_i^\mu \mathcal{J}_{ij}^{\mu\nu} S_j^\nu, \quad (3.1)$$

where Greek labels represent Cartesian coordinates. $\mathcal{J}_{ij}^{\mu\nu}$ is an element of the matrix of the bilinear spin-spin couplings defined through the Hamiltonians in Chapter 2. The mean field approximation is defined as [1]:

$$(S_i^\mu - m_i^\mu)(S_j^\nu - m_j^\nu) = 0, \quad (3.2)$$

where

$$m_i^\mu \equiv \langle S_i^\mu \rangle \quad (3.3)$$

and $\langle \dots \rangle$ represents a thermal average. Eq. (3.2) imposes the mean field condition which is that fluctuations about the average value of S_i^μ , m_i^μ , are ignored. We substitute $S_i^\mu S_j^\nu$ from Eq. (3.2) into Eq. (3.1) to obtain our s-MFT Hamiltonian [42]

$$\mathcal{H}_{\text{MF}} = \sum_{i,\mu} \left(h_i^\mu S_i^\mu - \frac{1}{2} h_i^\mu m_i^\mu \right), \quad (3.4)$$

where

$$h_i^\mu = \sum_{j,\nu} \mathcal{J}_{ij}^{\mu\nu} m_j^\nu. \quad (3.5)$$

¹In other words, critical or massless

\mathcal{H}_{MF} represents the Hamiltonian of a one-body system interacting with an average field \mathbf{h}_i . We consider \mathbf{S}_i to be 3-component classical vectors in 3 dimensional space unless mentioned otherwise. The Helmholtz free energy of this system is given by [57]

$$\mathcal{F}_{\text{MF}} = -\frac{1}{2} \sum_{ij} \sum_{\mu\nu} m_i^\mu \mathcal{J}_{ij}^{\mu\nu} m_j^\nu - \frac{1}{\beta} \sum_i \ln \left(\frac{4\pi \sinh(\beta|\mathbf{h}_i|)}{\beta|\mathbf{h}_i|} \right) \quad (3.6)$$

where $\beta = 1/k_{\text{B}}T$, k_{B} is the Boltzmann constant and T is temperature. Upon minimizing Eq. (3.6) with respect to \mathbf{h}_i , one obtains the direct space s-MFT self-consistent equation [57]:

$$\mathbf{m}_i = -\frac{\mathbf{h}_i}{|\mathbf{h}_i|} \left[\coth(\beta|\mathbf{h}_i|) - \frac{1}{\beta|\mathbf{h}_i|} \right] \quad (3.7)$$

The s-MFT extrema free-energy states of the system at temperature T can be found from the states obtained by solving this equation. The global minimum will then be determined among the extrema using Eq. (3.6).

3.1.2 Reciprocal space s-MFT

The propagation wave vector of the ordered state at $T = T_c^-$ and the s-MFT transition temperature T_c can be determined by considering the Fourier transform of the s-MFT free energy up to quadratic order². We focus on the pyrochlore lattice³. The s-MFT free energy up to quadratic order in $\{m_i^\mu\}$ reads [24]

$$\mathcal{F}_{\text{MF}} = -\frac{1}{\beta} \sum_i \ln(4\pi) - \frac{1}{2} \sum_{ij} \sum_{\mu\nu} m_i^\mu (\mathcal{J}_{ij}^{\mu\nu} + \frac{3}{\beta} \delta_{ij} \delta_{\mu\nu}) m_j^\nu + O(|\mathbf{m}_i|^4) \quad (3.8)$$

where we used $\ln(4\pi \sinh(\beta|\mathbf{h}_i|)/\beta|\mathbf{h}_i|) \simeq \ln(4\pi) + (\beta|\mathbf{h}_i|)^2/6 + O(|\mathbf{m}_i|^4)$ and $(\beta|\mathbf{h}_i|)^2 \simeq 9|\mathbf{m}_i|^2$ which comes from the Taylor expansion of Eq. (3.7) in powers of $|\mathbf{h}_i|$. δ_{ij} and $\delta_{\mu\nu}$ are Kronecker deltas. We define the following Fourier transforms [56]:

$$m_i^\mu = \sum_{\mathbf{q}} m_a^\mu(\mathbf{q}) e^{i\mathbf{q}\cdot\mathbf{r}_i} \quad (3.9)$$

²Because in the $T \lesssim T_c$ temperature regime, $|\mathbf{m}_i|$ and consequently $|\mathbf{h}_i|$ are small.

³In this thesis we focus on the pyrochlore lattice to obtain the Fourier transform of the s-MFT free energy. The case of the FCC lattice can be easily obtained by following a similar procedure without facing the complications that arise in the case of a non-Bravais lattice.

and

$$\mathcal{J}_{ij}^{\mu\nu} = \frac{1}{N} \sum_{\mathbf{q}} \mathcal{J}_{ab}^{\mu\nu}(\mathbf{q}) e^{i\mathbf{q}\cdot(\mathbf{r}_j - \mathbf{r}_i)}. \quad (3.10)$$

$\mathbf{r}_i \equiv \mathbf{R}_i + \mathbf{r}^a$ where \mathbf{r}_i is a pyrochlore lattice position vector, \mathbf{R}_i is an FCC lattice position vector and \mathbf{r}^a is a basis position vector, henceforth referred to as sublattices, with $a = 0, \dots, 3$. (For more details see Appendix A). N is the number of FCC lattice points. Consequently, to quadratic order in $\{m_a^\mu\}$, the s-MFT free energy in reciprocal space reads [24, 56]

$$\frac{1}{N} \mathcal{F}_{\text{MF}} = -\frac{1}{\beta} \ln(4\pi) - \frac{1}{2} \sum_{\mathbf{q}} \sum_{ab} \sum_{\mu\nu} m_a^\mu(\mathbf{q}) (\mathcal{J}_{ab}^{\mu\nu}(\mathbf{q}) + \frac{3}{\beta} \delta_{ab} \delta_{\mu\nu}) m_b^\nu(\mathbf{q}) + \dots, \quad (3.11)$$

where \dots represents higher order terms in components of $\mathbf{m}_a(\mathbf{q})$. $\mathcal{J}_{ab}^{\mu\nu}(\mathbf{q})$ is an element of the 12×12 interaction matrix $\mathcal{J}(\mathbf{q})$. Since the pyrochlore lattice is a non-Bravais lattice, $\mathcal{J}(\mathbf{q})$ is not diagonal. In order to find the soft modes as well as the s-MFT transition temperature, we need to determine the nodes of the coefficient of the quadratic term in free energy. To do so, we need to diagonalize $\mathcal{J}(\mathbf{q})$. The coefficient of the quartic term in Eqs. (3.8, 3.11) should be assessed in order to determine the nature of the phase transition i.e. first order transition versus continuous transition and to ensure the stability of the ordered phase (i.e. having an ordered state with finite energy and finite $|\mathbf{m}_i|$). Based on the symmetries of the pyrochlore lattice, the s-MFT free-energy can have isotropic and anisotropic quartic terms. If the isotropic quartic term's coefficient is negative, the coefficient of the sixth order term and in some cases eighth order terms in free-energy need to be evaluated to ensure stability of the ordered phase.

The minimum eigenvalue of $\mathcal{J}(\mathbf{q})$ over the first Brillouin zone, $\lambda^{\min}(\mathbf{q}_0)$, determines the normal modes that first become soft as temperature is decreased. The system enters the ordered phase at $T_c = -\lambda^{\min}(\mathbf{q}_0)/3$ [56] where \mathbf{q}_0 is the wave vector at which the minimum eigenvalue of $\mathcal{J}(\mathbf{q})$ occurs⁴. The eigenvector corresponding to $\lambda^{\min}(\mathbf{q}_0)$ determines the configuration of the ordered moments on a single tetrahedron which propagates throughout the lattice with \mathbf{q}_0 wave vector. This is the final result of the reciprocal space s-MFT that we are concerned with in this thesis.

⁴The minus sign in the equation corresponding to T_c comes from the convention we chose in writing the Hamiltonian in Eq. (3.1)

3.2 Monte Carlo methods

The s-MFT methods presented in Section 3.1 provide an initial semi-quantitative description of the system of interest. In this section we review a numerical method which enables us to study the physics beyond s-MFT approximation. The Monte Carlo method refers to a wide category of numerical algorithms that use statistical sampling to tackle problems that are not exactly solvable. Monte Carlo simulations are applied widely in condensed matter physics [58].

Among numerous numerical algorithms, in this thesis we employ the Metropolis-Hastings and the heat bath algorithms to simulate spin systems on a lattice. The Metropolis-Hastings algorithm provides an efficient method to simulate the system of interest and is applicable to any lattice symmetry [4]. On the other, the heat bath algorithm can provide us with higher efficiency than metropolis algorithm, but is only applicable to certain lattice symmetries [4]. We next review both of these methods.

3.2.1 Metropolis algorithm

In 1953, Nicholas Metropolis and collaborators in their paper titled "Equation of State Calculations by Fast Computing Machines", proposed an algorithm known today as the Metropolis algorithm [59] which was generalized by W. K. Hastings in 1971 [60]. To illustrate the implementation of the Metropolis algorithm, we consider a canonical ensemble at temperature T . A microstate with energy E_k arises with probability $w_B \equiv e^{-E_k/k_B T} / Z$ where $Z = \sum_k e^{-E_k/k_B T}$ is the partition function and k_B is the Boltzmann constant. The goal of the Metropolis algorithm is to generate a Markov chain⁵ of sample values of a physical observable O with Boltzmann probability distribution as its equilibrium distribution. The Markov chain is described by a transition matrix P which has to satisfy ergodicity and detailed balance. Ergodicity ensures that every possible microstate of the system can be reached by a finite number of elementary random moves from another microstate. The detailed balance condition is given by

$$w_i P_{ij} = w_j P_{ji} \quad (3.12)$$

where w_i and w_j are the equilibrium probabilities of being in states i and j , respectively, which in our case are the Boltzmann probabilities. P_{ij} is the transition probability from state i to state j . The process of generating the Markov chain in Metropolis algorithm can be summarized in following steps

⁵A sequence of random variables $\{X_i\}$ where for a given X_n , X_{n-1} and X_{n+1} are independent.

- Start with a random microstate i with energy E_i
- Make a random change in the microstate i to create microstate j with energy E_j
- Accept or reject the previous "move" with the probability

$$P_{\text{accept}} = \min(1, e^{-\Delta E/K_B T}) \quad (3.13)$$

where $\Delta E \equiv E_j - E_i$. and $\min(a, b)$ represents the minimum of the set $\{a, b\}$.

These three steps are the core of a Monte Carlo simulation. Starting from a random configuration, the above sequence of steps should be repeated several times in order to reach an equilibrium distribution. As a result, one needs to run the simulation for sufficient time before starting to measure physical observables. The sample values of observable O can be measured when equilibration is reached. The average value of O is the arithmetic average of sample values. We note that Metropolis algorithm implements importance-sampling in the third step where random change is weighted and is chosen with Boltzmann probability. The importance sampling increases the efficiency of the algorithm and promotes statistically important microstates which might not be reached if random changes are sampled from a uniform distribution.

3.2.2 Heat bath algorithm

In the Metropolis algorithm a proposed configuration update is accepted with probability P_{accept} in Eq. (3.13). In order to increase the acceptance rate of the updates which in turn increases the efficiency of the simulation and leads to a faster equilibration, the configuration updates should be chosen in such a way that $\Delta E = E_j - E_i$ in Eq. (3.13) is small. The heat bath method offers a more efficient way of local updates in which the new configuration energy is exactly distributed according to a Boltzmann weight [4]. In this case, all the update are accepted. In Chapter 7 of this thesis, we apply this method to the case of isotropic Heisenberg spins on the FCC lattice interacting via magnetostatic long-range dipole-dipole interaction. The heat bath updates (i.e. the new spin orientations) for isotropic Heisenberg spins can be calculated analytically. We consider the Hamiltonian of the system in the following form [4]

$$\mathcal{H} = \frac{1}{2} \sum_i \mathbf{h}_i \cdot \mathbf{S}_i \quad (3.14)$$

where \mathbf{h}_i is the local field with components defined as $h_i^\mu \equiv \sum_{j \neq i, \nu} \mathcal{J}_{ij}^{\mu\nu} S_j^\nu$. In consequence, the energy of the i^{th} spin reads

$$E_i = \mathbf{h}_i \cdot \mathbf{S}_i = h_i \cos(\theta_i) \quad (3.15)$$

where h_i is the magnitude of \mathbf{h}_i and θ_i is the polar angle between \mathbf{S}_i and \mathbf{h}_i . In the heat bath algorithm, we aim to randomly update \mathbf{S}_i such that E_i in Eq. (3.15) has a Boltzmann probability distribution. To do so, we consider \mathbf{S}_i in a spherical coordinate system with the polar axis along \mathbf{h}_i . E_i is independent of the azimuthal angle ϕ_i in this coordinate system. Consequently, we update the ϕ_i by randomly choosing an angle in the interval $[0, 2\pi)$ from a uniform distribution. The new polar angle θ_i must be chosen with the following probability distribution p given by [61]

$$p(x) = \frac{e^{-\beta h_i x}}{\int_{-1}^1 e^{-\beta h_i x} dx} = \frac{\beta h_i}{\sinh(\beta h_i)} e^{-\beta h_i x} \quad (3.16)$$

where $\beta = 1/k_B T$ and $x = \cos(\theta_i)$. To propose a random θ_i with probability distribution p , one first needs to consider the cumulative distribution F associated with p given by:

$$F(x) = \int_{-1}^x p(x') dx'. \quad (3.17)$$

The next step is to obtain x , randomly using the following [61]:

$$x = F^{-1}(r) = -1 - \frac{\ln[1 - r(1 - \exp(-2\beta h_i))]}{\beta h_i} \quad (3.18)$$

where $r \in [0, 1]$ is a random number and F^{-1} is the inverse of F ⁶. As a result, the x evaluated in Eq. (3.18) has the probability distribution p . The updated spin at site i , $\mathbf{S}_i^{\text{new}}$, can be calculated from updated θ_i and ϕ_i which is expressed in the spherical coordinate system with polar axis along \mathbf{h}_i . Since the $\mathbf{S}_i^{\text{new}}$, is expressed in the "local" coordinate system, in order to implement the new spin orientation in the system i.e. to calculate \mathbf{h}_j where $j \neq i$ and carry on the simulation, one needs to express $\mathbf{S}_i^{\text{new}}$ in the global coordinate system [4].

⁶We note that if the Hamiltonian includes self-interaction term i.e. $\mathcal{J}_{ii}^{\mu\nu} \neq 0$, F can not be integrated and inverted analytically. This is the case for long-range dipolar interaction in a system with periodic boundary condition. However, in systems with cubic symmetries, the self-interaction term only contributes a constant to the Hamiltonian which is independent of the spin configuration. Consequently, heat bath method can be applied [4, 62]

3.2.3 Parallel tempering method

The Metropolis and heat bath algorithms provide local updates in a Monte Carlo simulation. However, these updates might not be sufficient to reach equilibration in systems with large energy barriers between different microstates. Consequently, the system can be trapped in a local minimum of free-energy. The parallel tempering method, also known as replica exchange method [63], offers a way to better equilibrate these systems by swapping the configurations at different temperatures (the so-called thermal replicas). During a simulation, the system explores a larger volume of configuration space at high temperatures compared to low temperatures. Exchanging the configurations at different temperatures provides an opportunity for the system to travel between local free-energy minima at low temperatures, which would be otherwise impossible since the energy barriers between those local minima could not be overcome by local updates.

The configuration swap in the parallel tempering method should satisfy the detailed balance condition. To demonstrate this point, we consider a system with N thermal replicas which form an extended ensemble $X = \{X_1, \dots, X_N\}$ at temperatures $\{T_1, \dots, T_N\}$, respectively. The partition function of this ensemble can be written as

$$Z = \prod_{n=1}^N Z_n, \quad (3.19)$$

where Z_n is the partition function at $T = T_n$. The probability of a given configuration X then reads:

$$W(X) = \prod_{n=1}^N w(X_n, T_n) \quad (3.20)$$

where $w(X_n, T_n) = \exp(-E(X_n)/k_B T_n)/Z_n$ and $E(X_n)$ is the energy of the replica X_n . A proposed configuration swap between temperatures T_k and T_l should satisfy the detailed balance condition given by:

$$W_{kl} P_{kl \rightarrow lk} = W_{lk} P_{lk \rightarrow kl}. \quad (3.21)$$

Here, $W_{kl} = W(X = \{X_1, \dots, X_k, X_l, \dots, X_n\})$ and $P_{kl \rightarrow lk}$ represents the transition probability between $X = \{X_1, \dots, X_k, X_l, \dots, X_n\}$ and $X' = \{X_1, \dots, X_l, X_k, \dots, X_n\}$ where replicas at temperatures T_k and T_l are being swapped. Accordingly, the swap will be accepted by the following probability

$$P_{\text{accept}} = \min(1, e^{-\Delta}) \quad (3.22)$$

where $\Delta = (E(X_k) - E(X_l))/k_B T_k + (E(X_l) - E(X_k))/k_B T_l$. For this swap to be accepted, the configuration at $T = T_l$ should be likely to happen at $T = T_k$ and vice versa. In other

words, there should be overlap between probability distributions at T_k and T_l . As a result, for a given temperature range, it is more probable for a proposed swap to be accepted if the number of thermal replicas are more.

3.3 Extended TAP method (E-TAP)

In Section 3.2, we reviewed a variety of numerical techniques known as the Monte Carlo methods to capture the physics beyond the s-MFT approximation. In this section we introduce an analytical method for the same purpose⁷, in particular, to explore the physics beyond the s-MFT at $T = T_c^-$.

In 1977, Thouless, Anderson and Palmer (TAP) [66] proposed a method to study the role of fluctuations in spin glasses. This method is equivalent to calculating the Onsager reaction field [67]: a magnetic moment at a particular lattice site experiences a local field due to its neighbours. At the s-MFT level, the presence of the spin at the site of interest affects its local field indirectly, which is an artifact of s-MFT. The Onsager reaction field introduces a term that cancels this unphysical effect [2]. The TAP approach provides a systematic way to implement the Onsager reaction field correction [67].

In this thesis, we develop an extended version of the TAP method (E-TAP), a high temperature expansion, for Heisenberg-spin systems, first developed by Georges and Yedidia [68] for Ising spin-glass and includes fluctuation corrections calculated by TAP and those beyond in powers of $\beta = 1/k_B T$. In the E-TAP method, nonzero on-site fluctuations i.e. $\langle S_i^\alpha S_i^\beta \rangle \neq \langle S_i^\alpha \rangle \langle S_i^\beta \rangle$ [68], are taken into account via a high-temperature expansion (small β) of the Gibbs free-energy:

$$G = -\frac{1}{\beta} \ln \left(\text{Tr}[\exp(-\beta \mathcal{H} + \sum_i \boldsymbol{\lambda}_i \cdot (\mathbf{S}_i - \mathbf{m}_i))] \right). \quad (3.23)$$

Here, \mathbf{m}_i is the average magnetization at site i , $\mathbf{m}_i \equiv \langle \mathbf{S}_i \rangle$ and $\boldsymbol{\lambda}_i$ is a Lagrange multiplier which fixes \mathbf{m}_i to its mean-field value. The high temperature expansion introduces

⁷An alternative well-known process totake into account fluctuations about standard mean-field theory (s-MFT) solutionis Hubbard-Stratonovich transformation (HST) [64, 65] . In the context of magnetic systems, this process introduces a set of auxiliary variables (molecular fields) to replace spin variables. Then, fluctuations about the average molecular fields up to quadratic orderare consideredin the long-wave length limit. These fluctuations introduce various infrared divergent corrections to the theory in $d < 4$ spatial dimensions [65]. The E-TAP method, on the other hand, takes into accountshort-range fluctuations with longer range fluctuations taken into account through higher order terms in the β expansion. As a result, the underlying assumption on the nature of the fluctuations in the HST and E-TAP method are different.

fluctuations about the s-MFT solution. Defining $\beta G(\beta) \equiv \tilde{G}(\beta)$, the first two terms of the expansion in powers of β , $\tilde{G}(0)/\beta$ and $\tilde{G}'(0)$, are the entropy and energy at the s-MFT level, respectively. The prime represents differentiation with respect to β . The higher order terms in the β expansion of the Gibbs free-energy correspond to fluctuation corrections to the s-MFT free-energy.

To proceed, we modify E-TAP procedure of Ref.[68] to study the case of 3-component classical Heisenberg spins with anisotropic exchange interactions. We focus on a temperature regime close to the mean field critical temperature, $T \lesssim T_c^{\text{MF}}$. We consider the Hamiltonian in Eq. (3.1). A Taylor series expansion of Eq. (5.9) in powers of β reads:

$$G(\beta) = \frac{1}{\beta} \left(\tilde{G}(\beta) \Big|_{\beta=0} + \frac{\partial \tilde{G}(\beta)}{\partial \beta} \Big|_{\beta=0} \beta + \frac{1}{2!} \frac{\partial^2 \tilde{G}(\beta)}{\partial \beta^2} \Big|_{\beta=0} \beta^2 \dots \right), \quad (3.24)$$

where $\tilde{G}(\beta) = \beta G(\beta)$. We define,

$$U \equiv \frac{1}{2} \sum_{ij} \delta S_i^\mu J_{ij}^{\mu\nu} \delta S_j^\nu \quad (3.25)$$

where

$$\delta S_j^\nu \equiv S_j^\nu - m_j^\nu, \quad (3.26)$$

which represents spin fluctuations about the s-MFT solution. As shown in Ref. [68], the derivatives of $\tilde{G}(\beta)$ with respect to β can be evaluated in terms of expectation value of powers of U that read:

$$\frac{\partial(\beta G(\beta))}{\partial\beta} = \langle \mathcal{H} \rangle, \quad (3.27a)$$

$$\frac{\partial^2(\beta G(\beta))}{\partial\beta^2} = -\langle U^2 \rangle, \quad (3.27b)$$

$$\frac{\partial^3(\beta G(\beta))}{\partial\beta^3} = \langle U^3 \rangle, \quad (3.27c)$$

$$\frac{\partial^4(\beta G(\beta))}{\partial\beta^4} = -\langle U^4 \rangle + 3\langle U^2 \rangle^2 - 3\langle U^2 T_2 \rangle, \quad (3.27d)$$

$$\frac{\partial^5(\beta G(\beta))}{\partial\beta^5} = \langle U^5 \rangle - 10\langle U^2 \rangle \langle U^3 \rangle - 3\langle U^2 T_3 \rangle + 7\langle U^3 T_2 \rangle + 6\langle U T_2^2 \rangle, \quad (3.27e)$$

$$\begin{aligned} \frac{\partial^6(\beta G(\beta))}{\partial\beta^6} = & -\langle U^6 \rangle + 15\langle U^4 \rangle \langle U^2 \rangle + 10\langle U^3 \rangle^2 - 30\langle U^2 \rangle^3 - 12\langle U^4 T_2 \rangle \\ & + 10\langle U^3 T_3 \rangle - 3\langle U^2 T_4 \rangle - 27\langle U^2 T_2^2 \rangle + 18\langle U T_2 T_3 \rangle \\ & - 6\langle U T_3 \rangle \langle U^2 \rangle + 51\langle U^2 \rangle \langle U^2 T_2 \rangle + 6\langle U^2 \rangle \langle T_2^2 \rangle - 6\langle T_2^3 \rangle, \end{aligned} \quad (3.27f)$$

where

$$T_n = \sum_i \frac{\partial^n \boldsymbol{\lambda}_i}{\partial \beta^n} \cdot \delta \mathbf{S}_i. \quad (3.28)$$

The terms involving T_n include fluctuations of the local mean field. On the other hand, the terms that involve U^n , take into account the fluctuations of the magnetization \mathbf{m}_i itself (see Eqs. (3.25, 3.26))⁸. The $\langle \dots \rangle$ above denotes a thermal average. For a general observable O , $\langle O \rangle$ is given by:

$$\langle O \rangle = \frac{\text{Tr}[O \exp(-\beta H + \sum_i \boldsymbol{\lambda}_i \cdot (\mathbf{S}_i - \mathbf{m}_i))]}{\text{Tr}[\exp(-\beta H + \sum_i \boldsymbol{\lambda}_i \cdot (\mathbf{S}_i - \mathbf{m}_i))]} \quad (3.29)$$

The first two terms in Eq. (3.24) correspond to the s-MFT free-energy while the higher order terms in β provide the corrections beyond s-MFT. Calculating the expectation value of powers of U at $\beta = 0$, reduces to the evaluation of the mean field averages of the following form:

$$\langle \delta S_{i_1}^{\alpha_1} \delta S_{i_2}^{\alpha_2} \dots \delta S_{i_n}^{\alpha_n} \rangle_{\text{MF}}, \quad (3.30)$$

where i_n represents the site label and α_n represents a Cartesian coordinate. n is the number of δS factors in Eq. (3.30). For simplicity, we henceforth drop the MF subscript in Eq.

⁸This method can be generalized to include quantum mechanical effects. To do so, one needs to treat the δS_i^μ as operators in deriving Eqs. (3.27).

(3.30). For $n = 1$, the expectation value in Eq. (3.30) is zero due to the relation $\mathbf{m}_i = \langle \mathbf{S}_i \rangle$. For $n \geq 2$, however, Eq. (3.30) is nonzero only if there is no site label which appears only once. For example, averages of the following form have a nonzero contribution:

$$\langle \delta S_i^{\alpha_1} \delta S_i^{\alpha_2} \delta S_j^{\alpha_3} \delta S_j^{\alpha_4} \delta S_j^{\alpha_5} \rangle = \langle \delta S_i^{\alpha_1} \delta S_i^{\alpha_2} \rangle \langle \delta S_j^{\alpha_3} \delta S_j^{\alpha_4} \delta S_j^{\alpha_5} \rangle \quad (3.31)$$

The expectation values above can be calculated using the self-consistent s-MFT equations for 3-component classical spins which are given by the Langevin function

$$\mathbf{m}_i = -\frac{\boldsymbol{\lambda}_i}{|\boldsymbol{\lambda}_i|} \left[\coth(|\boldsymbol{\lambda}_i|) - \frac{1}{|\boldsymbol{\lambda}_i|} \right]. \quad (3.32)$$

Consequently

$$\langle \delta S_i^\alpha \delta S_i^\beta \rangle = \frac{\partial m_i^\alpha}{\partial \lambda_i^\beta} \equiv \chi_i^{\alpha\beta}, \quad (3.33)$$

$$\langle \delta S_i^\alpha \delta S_i^\beta \delta S_i^\gamma \rangle = \frac{\partial \chi_i^{\alpha\beta}}{\partial \lambda_i^\gamma}, \quad (3.34)$$

and in general

$$\langle \delta S_i^{\alpha_1} \delta S_i^{\alpha_2} \dots \delta S_i^{\alpha_n} \rangle = \frac{\partial \langle \delta S_i^{\alpha_1} \delta S_i^{\alpha_2} \dots \delta S_i^{\alpha_{n-1}} \rangle}{\partial \lambda_i^{\alpha_n}}. \quad (3.35)$$

Since we are interested in a temperature range close to T_c , Eq. (3.32) can be expanded for small $|\boldsymbol{\lambda}_i|$:

$$m_i^\alpha = -\frac{\lambda_i^\alpha}{3} \left[1 - \frac{(|\boldsymbol{\lambda}_i|)^2}{15} + \frac{2(|\boldsymbol{\lambda}_i|)^4}{315} + \dots \right], \quad (3.36)$$

The expansions of Eqs. (3.33, 3.34, 3.35) at $T \lesssim T_c$ can be calculated by differentiating Eq. (3.36) with respect to different components of the vector $\boldsymbol{\lambda}_i$.

3.4 Spin wave theory

In this section, we briefly review the well-known spin wave theory which we use to explore the physics beyond s-MFT at $T = 0^+$ in Chapter 7.

Spin wave theory in its simplest form takes into account the harmonic quantum spin fluctuations about a classical long-range ordered state. This allows one to explore the low-lying excited states of the system and, consequently, its low-temperature properties. In

this thesis, we use spin wave theory to study the low-temperature properties of a system of point dipole on a FCC lattice with ferromagnetic ordering. The case of more complicated systems e.g. low-lying excitations of an antiferromagnetic ordering on a pyrochlore lattice can be found in Ref. [69].

A system of point-dipoles on FCC lattice is expected to order ferromagnetically [36]. To calculate the dispersion relation of the low-lying excitation, we consider a classical approach.

The time evolution of the spins can be written as:

$$\frac{d\mathbf{S}_i}{dt} = \mathbf{S}_i \times \mathbf{B}_i \quad (3.37)$$

where

$$B_i^\mu = \sum_{j,\nu} \mathcal{J}_{ij}^{\mu\nu} S_j^\nu, \quad (3.38)$$

where $\mathcal{J}_{ij}^{\mu\nu}$ is the long range dipolar interaction matrix element defined in Eq. (2.10) and expressed in global coordinates. To proceed, we consider the polarization direction along z -axis and we define:

$$\mathbf{S}_i^x = \delta_i^x, \quad (3.39a)$$

$$\mathbf{S}_i^y = \delta_i^y, \quad (3.39b)$$

$$\mathbf{S}_i^z = 1 - \frac{1}{2} \left((\delta_i^x)^2 + (\delta_i^y)^2 \right). \quad (3.39c)$$

δ_i^μ with $\mu = x, y$, characterizes transverse spin fluctuations. We then define $\tilde{\mathcal{J}}_{ij}^{\mu\nu} = \sum_\alpha R^{\mu\alpha} \mathcal{J}_{ij}^{\alpha\nu}$ where

$$R \equiv \begin{pmatrix} -\cos(\theta) \cos(\phi) & -\cos(\theta) \sin(\phi) & \sin(\theta) \\ \sin(\phi) & -\cos(\phi) & 0 \\ \sin(\theta) \cos(\phi) & \sin(\theta) \sin(\phi) & \cos(\theta) \end{pmatrix}. \quad (3.40)$$

$\tilde{\mathcal{J}}_{ij}^{\mu\nu}$ is the coupling matrix expressed in the coordinate system with polarization direction defined by θ and ϕ , the polar and azimuthal angles of the ferromagnetic order, respectively. We also define the following Fourier transforms:

$$\delta_i^\alpha(t) = \frac{1}{\sqrt{N}} \sum_{\mathbf{k}} \sum_{\omega} \delta^\alpha(\mathbf{k}) e^{i(\mathbf{k} \cdot \mathbf{r}_i - \omega t)}, \quad (3.41a)$$

$$\tilde{\mathcal{J}}_{ij}^{\mu\nu} = \frac{1}{N} \sum_{\mathbf{k}} \mathcal{J}^{\mu\nu}(\mathbf{q}) e^{i\mathbf{q} \cdot (\mathbf{r}_j - \mathbf{r}_i)}, \quad (3.41b)$$

Substituting Eqs. (3.39, 3.41) in Eq. (3.37) and after some simple algebraic steps, we obtain:

$$\begin{pmatrix} -i\omega - S\mathcal{J}^{xy}(\mathbf{k}) & -S\mathcal{J}^{yy}(\mathbf{k}) + S\mathcal{J}^{zz}(0) \\ S\mathcal{J}^{xx}(\mathbf{k}) - S\mathcal{J}^{zz}(0) & -i\omega + S\mathcal{J}^{xy}(\mathbf{k}) \end{pmatrix} \begin{pmatrix} \delta^x(\mathbf{k}) \\ \delta^y(\mathbf{k}) \end{pmatrix} = \begin{pmatrix} 0 \\ 0 \end{pmatrix} \quad (3.42)$$

where we kept only terms to the lowest order in $\delta^\mu(\mathbf{k})$. To obtain the dispersion relation of the transverse fluctuation, $\omega(\mathbf{k})$, the roots of the determinant of the 2×2 matrix in Eq. (3.42) should be calculated which yields to

$$\frac{\omega^2(\mathbf{k})}{S^2} = -\left(\mathcal{J}^{xy}(\mathbf{k})\right)^2 + \left(\mathcal{J}^{zz}(0)\right)^2 - \mathcal{J}^{zz}(0)\left(\mathcal{J}^{xx}(\mathbf{k}) + \mathcal{J}^{yy}(\mathbf{k})\right) + \mathcal{J}^{xx}(\mathbf{k})\mathcal{J}^{yy}(\mathbf{k}). \quad (3.43)$$

Part II

Results

The following contents of Part II of the thesis is the outcome of works with several collaborators which follows as:

Chapter 4: The contents of this chapter has been submitted to Physical Review Letters and is available on arXiv:1310.5146 under the title: "Fluctuation-Driven Selection at Criticality in a Frustrated Magnetic System: the Case of Multiple- \mathbf{k} Partial Order on the Pyrochlore Lattice". The coauthors of the paper are Zhihao Hao, Matthew Enjalran and Michel Gingras. The author of this thesis is responsible for the following in this work: s-MFT calculations, E-TAP calculations, Monte Carlo simulations and part of the Ginzburg-Landau symmetry analysis as well as the entire first draft of the paper.

Chapter 5: The contents of this chapter will appear in a paper that is in preparation at the moment. The collaborators of this work are: Alexandre G. R. Day, Zhihao Hao and Michel Gingras. The author of this thesis is responsible for the Ginzburg-Landau analysis and the E-TAP calculations. The diagrammatic method was developed by the author of this thesis. The code for calculating the diagram counts mentioned in Appendix E was written by Alexandre G. R. Day.

Chapter 6: The contents of this chapter will appear in a paper that is in preparation at the moment. The collaborators of this work are: Pawel Stasiak and Michel Gingras. The author of this thesis is responsible for performing the Monte Carlo simulations and data analysis. Part of the Monte Carlo results in this chapter has also appeared in the following publication: J. Oitmaa, R. R. P. Singh, B. Javanparast, A. G. R. Day, B. V. Bagheri, and M. J. P. Gingras. Phase transition and thermal order-by-disorder in the pyrochlore antiferromagnet $\text{Er}_2\text{Ti}_2\text{O}_7$: A high-temperature series expansion study. *Phys. Rev. B*, **88**, 220404, 2013.

Chapter 7: The contents of this chapter will appear in a paper that is in preparation at the moment. The collaborators of this work are: Zhihao Hao, Michel Gingras and Byron Southern from University of Manitoba. The author of the thesis is responsible for the following calculations: s-MFT and E-TAP calculations, Monte Carlo simulations and Ginzburg-Landau analysis.

The Monte Carlo code used in all of the above works, was primarily written by Pawel Stasiak. The code was then modified and optimized by the author of the thesis to meet the requirements of each problem.

The author of this thesis also coauthored the following publication: Spin Ice: Magnetic Excitations without Monopole Signatures Using Muon Spin Rotation, *Phys. Rev. Lett.* **107**, 207207 (2011) where the author contributed in calculating muon's landing position in the $\text{Dy}_2\text{Ti}_2\text{O}_7$ spin ice material. The contributions of the author are not presented in this thesis due their different subject matter from the main theme of this thesis

Chapter 4

Thermal Selection of Multi- k Partial Order on Pyrochlore Lattice

In this chapter, we explore the ObD phenomenon at $T = T_c^-$ in a 4-vector model with an emergent $O(4)$ symmetry at the s-MFT level. Study of this model is motivated by the experimentally reported ordered phase of the rare-earth pyrochlore oxide $\text{Gd}_2\text{Ti}_2\text{O}_7$ at $T \lesssim T_c = 1$ K, where T_c is the transition temperature from the paramagnetic phase to a partially ordered state (POS). A POS possesses periodically distributed disordered (paramagnetic) sites on the pyrochlore lattice. The periodicity of POS phases is characterized by one or more wave vectors $\mathbf{k} = \{\frac{1}{2}\frac{1}{2}\frac{1}{2}\}$. We demonstrate that thermal fluctuations ignored in s-MFT are responsible for the selection of one particular partially ordered phase, e.g. the “4- \mathbf{k} ” phase over the “1- \mathbf{k} ” phase. We suggest that the transition into the 4- \mathbf{k} phase is continuous with its critical properties controlled by the cubic fixed point of a Ginzburg-Landau theory with a 4-component vector order-parameter. By combining the E-TAP method with parallel-tempering Monte-Carlo simulations, we establish the phase diagram for different types of partially ordered phases. Our results contribute to elucidate the long-standing puzzle concerning the origin of the 4- \mathbf{k} partially ordered phase observed in the $\text{Gd}_2\text{Ti}_2\text{O}_7$ below its paramagnetic phase transition temperature.

4.1 Introduction

For reasons mentioned in Chapter 1, highly frustrated magnetism is one of the paradigms of modern condensed matter physics [18]. In frustrated magnets, the combination of lattice geometry and competing interactions often leads to degenerate classical states. The

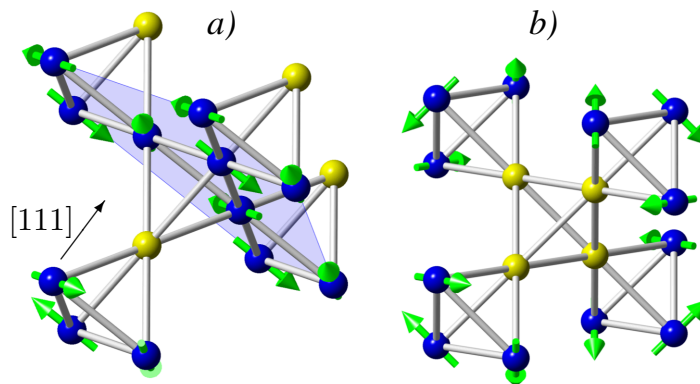


Figure 4.1: The yellow (arrowless) sites are disordered (paramagnetic). *a*) a $1\text{-}\mathbf{k}$ state with \mathbf{k} along $[111]$. The spins on the (blue) ordered sites form a 120° pattern on a triangle that does not share a corner with a disordered site. These ordered sites form a kagome plane (blue-shaded plane) perpendicular to the $[111]$ direction. *b*) $4\text{-}\mathbf{k}$ state arising from the superposition of four $1\text{-}\mathbf{k}$ states.

degeneracies are generally accidental as they are not protected by the symmetries of the spin Hamiltonian. Yet, the degenerate states may be related by transformations that form an *emergent* symmetry group. Near a continuous phase transition, these approximate symmetries provide “organizing principles” in determining the critical properties by distinguishing relevant perturbations from irrelevant ones. In the most interesting case, the leading degeneracy-lifting perturbations, which may be relevant or irrelevant in the renormalization group sense, are thermal or quantum fluctuations – a phenomenon called order-by-disorder (ObD) [22, 25, 26, 27]. The competition among diverse degeneracy-lifting effects can result in a modulated long-range ordered state at nonzero wave vector \mathbf{k} , which may or may not be commensurate with the lattice [24, 70, 71, 72, 73, 74, 75]. In some cases, a number of superposed symmetry-related \mathbf{k} modes within the first Brillouin zone form a so-called *multiple- \mathbf{k} order* [70, 71, 76, 77]. A particular interesting form of such modulated magnetism is a partially ordered state (POS) with periodically arranged “paramagnetic” sites [78, 79, 80, 81]. These fluctuating magnetic moments decimate a fraction of the energy-costly frustrated bonds while retaining an extensive entropy, hence lowering the free-energy.

In this Chapter, we study the convergence of the aforementioned phenomena (emergent symmetry, multiple- \mathbf{k} POS and fluctuation-induced degeneracy-lifting) in an extensively

studied class of frustrated magnetic materials, the insulating $R_2M_2O_7$ pyrochlore oxides [11]. The competition between four types of nearest-neighbour anisotropic interactions mentioned in Chapter 2, and the nature of the single-ion magnetic anisotropy are largely responsible for the wealth of phenomena displayed by the $R_2M_2O_7$ materials [11]. We focus on a general description for the perplexing yet rich physics of multi- \mathbf{k} partial magnetic ordering in pyrochlore oxides and not on any material-specific issues.

A multi- \mathbf{k} POS (see Fig. 4.1b) is believed to exist in $Gd_2Ti_2O_7$ [19] for temperature $0.7 \text{ K} \lesssim T \lesssim T_c \sim 1 \text{ K}$ in which the POS is a superposition of spin density waves with wave vectors $\mathbf{k} = \{\frac{1}{2}\frac{1}{2}\frac{1}{2}\}$ [19, 57, 82, 83, 84, 85, 86]. While this compound has been the subject of a number of investigations [19, 83, 84, 87, 88, 89, 90, 91, 92, 93, 94, 95, 96], mechanism responsible for the selection of 4- \mathbf{k} order had not yet been identified before the work in this thesis. Further, after fifteen years of research on the $Tb_2Ti_2O_7$ spin liquid candidate [97], evidence has recently begun accumulating that short-range magnetic correlations develop below $T \sim 0.4 \text{ K}$ in the form of broad elastic neutron intensities at $\mathbf{k} = \{\frac{1}{2}\frac{1}{2}\frac{1}{2}\}$ [47, 98, 99, 100, 101]. To the best of our knowledge, no theory has yet explained the origin of these correlations in $Tb_2Ti_2O_7$. As $Gd_2Ti_2O_7$ and $Tb_2Ti_2O_7$ constitute two out of the six magnetic $R_2Ti_2O_7$ pyrochlore compounds that exist ($R=Gd, Tb, Dy, Ho, Er$ and Yb) [11], it may be that $\mathbf{k} = (\frac{1}{2}\frac{1}{2}\frac{1}{2})$ order is not unusual among the plethora of $R_2M_2O_7$ materials.

The rest of this chapter is organized as follows. In Section 4.2, we introduce the model Hamiltonian and identify an extensive range of exchange parameters able to support $\mathbf{k} = (\frac{1}{2}\frac{1}{2}\frac{1}{2})$ partial order through a standard mean-field theory (s-MFT) study. The s-MFT free-energy displays, up to quartic order in the order parameters, an *emergent* $O(4)$ symmetry. The transition into the POS is thus described by the Ginzburg-Landau free-energy, \mathcal{F}_{GL} , of an n -component vector model ($n = 4$) [64, 102]. The most relevant perturbation is a ‘‘cubic anisotropy’’ which breaks the $O(4)$ symmetry. We thus identify the physical origin of this cubic anisotropy as thermal fluctuations *beyond* s-MFT. The $O(4)$ symmetry-breaking and selection of either 1- \mathbf{k} or 4- \mathbf{k} order in this model is an example of thermal ObD. We stress, however, that our problem conceptually departs significantly from the more common cases of ObD where ‘‘small’’ thermal or quantum fluctuations are typically considered. This is valid for temperatures much lower than the critical temperature where the harmonic approximation is often justified. For example, in $Gd_2Ti_2O_7$, where another transition occurs at $T \sim 0.7 \text{ K} < T_c$ [87, 92, 93, 95, 96] (see Fig. 4.2), the low temperature ($T = 0^+$) fluctuations have no bearing on the state-selection at the critical temperature, T_c , to the paramagnetic phase. Consequently, a direct approach to the selection mechanism at $T = T_c^-$ is necessary, which we pursue here.

Given the above considerations on the effect of fluctuations in generating the cubic

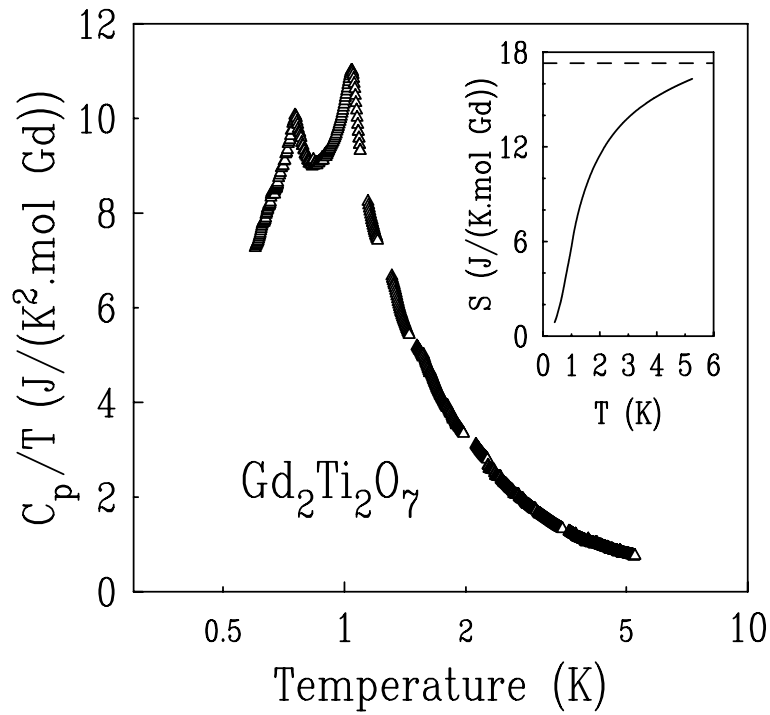


Figure 4.2: Reproduced from Ref. [88]. Specific heat of $Gd_2Ti_2O_7$ divided by temperature is plotted versus T indicating two phase transitions at $T \approx 1$ K and $T \approx 0.7$ K. The inset shows entropy versus temperature and the dashed line represents $R \ln(8)$ the total entropy associated with a spin $S = 7/2$.

anisotropy, in Section 4.3, we obtain the phase diagram of 1- \mathbf{k} and 4- \mathbf{k} orders using E-TAP. In Section 4.4, we use Monte Carlo simulations to confirm the E-TAP predictions that 1- \mathbf{k} and 4- \mathbf{k} POSs are selected in different portions of the phase diagram. As a corollary of this work, we suggest that the phase transition at $T_c \sim 1$ K in $\text{Gd}_2\text{Ti}_2\text{O}_7$ belongs to the above $n = 4$ cubic universality class.

4.2 Model and s-MFT treatment

We consider the general Hamiltonian, $\mathcal{H} = \mathcal{H}_{\text{nn}} + \mathcal{H}_{\text{dip}} + \mathcal{H}_2 + \mathcal{H}_3$, for classical spins, \mathbf{S}_i , on the pyrochlore lattice:

$$\mathcal{H}_{\text{nn}} \equiv \sum_{\langle i,j \rangle} [J \mathbf{S}_i \cdot \mathbf{S}_j + J_{\text{DM}} \hat{d}_{ij} \cdot (\mathbf{S}_i \times \mathbf{S}_j) + J_{\text{Ising}} (\mathbf{S}_i \cdot \hat{z}_i)(\mathbf{S}_j \cdot \hat{z}_j) + J_{\text{pd}} S_i^\alpha \Lambda_{ij}^{(\alpha\beta)} S_j^\beta]. \quad (4.1a)$$

$$\mathcal{H}_{\text{dip}} = J_{\text{dip}} \sum_{i>j} S_i^\alpha \Lambda_{ij}^{(\alpha\beta)} S_j^\beta. \quad (4.1b)$$

$$\mathcal{H}_2 \equiv \sum_{\langle\langle ij \rangle\rangle} J_2 \mathbf{S}_i \cdot \mathbf{S}_j, \quad \mathcal{H}_3 \equiv \sum_{\langle\langle\langle ij \rangle\rangle\rangle} J_3 \mathbf{S}_i \cdot \mathbf{S}_j. \quad (4.1c)$$

The details regarding each of the interactions in \mathcal{H}_{nn} are presented in Chapter 2. \mathcal{H}_{dip} is the long-range magnetostatic dipole-dipole interaction. \mathcal{H}_2 and \mathcal{H}_3 are second and third n.n. exchange interactions, respectively. We note that spin \mathbf{S}_i becomes a pseudo-spin describing the lowest energy doublet of the crystal electric field (CEF) if this interaction dominates others. In the case of $\text{Gd}_2\text{Ti}_2\text{O}_7$, the CEF interaction is small ($B_{20} = 75$ mK is the dominant term in Eq. (2.2) of Chapter 2) compared with the phase transition temperatures (0.7 K and 1K) [48]. We thus ignore CEF terms in Eq. (5.1). A discussion of the effect of CEF is presented in the Appendix B.3.

We begin by studying \mathcal{H}_{nn} using s-MFT [24, 56, 57]. For a large region of parameter space, a *degenerate* line of modes with momenta $\{hhh\}$ first becomes critical at T_c (see Fig. 4.3 for an illustration) [57, 82, 83, 85]. s-MFT calculations show that \mathcal{H}_{dip} lifts the degeneracy by weakly selecting soft modes at the four $\mathbf{L} \equiv \{\frac{1}{2}\frac{1}{2}\frac{1}{2}\}$ points within the first Brillouin zone, which we label \mathbf{k}_a ($a = 0, 1, 2, 3$) [57, 82]. Other perturbations to \mathcal{H}_{nn} , such as \mathcal{H}_2 and \mathcal{H}_3 , can have similar effects [57, 82, 85, 86]. Here, we focus on \mathcal{H}_{dip} since it is often of prominence in rare-earth pyrochlore oxides [11]. In particular, we choose, for concreteness, the $\text{Gd}_2\text{Ti}_2\text{O}_7$ value $J_{\text{dip}}/J \sim 0.18$ [83] as an example. For completeness, and of possible relevance to magnetic pyrochlores with ions having a small magnetic moment,

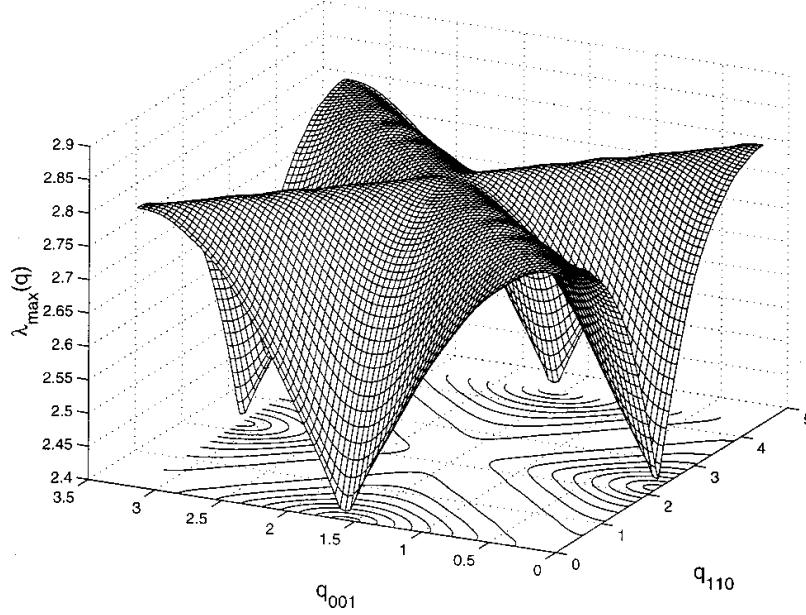


Figure 4.3: Reproduced from Ref. [83]. The line of degenerate modes at T_c for a model with Hamiltonian $\mathcal{H} = \sum_{\langle i,j \rangle} [J \mathbf{S}_i \cdot \mathbf{S}_j + J_{\text{dip}} S_i^\alpha \Lambda_{ij}^{(\alpha\beta)} S_j^\beta]$.

we present some results in the Appendix C that use the notation of Ref. [44] for \mathcal{H}_{nn} and where the $\{hhh\}$ degeneracy-lifting originates from \mathcal{H}_2 as opposed to \mathcal{H}_{dip} .

The direct space spin configurations corresponding to a $1-\mathbf{k}$ state, with $\mathbf{k} = \mathbf{k}_0 \equiv (\frac{1}{2} \frac{1}{2} \frac{1}{2})$, is illustrated in Fig. 4.1a. Denoting the corresponding spin direction at site \mathbf{r}_i as $\hat{e}_{\mathbf{k}_0}(\mathbf{r}_i)$, with $\hat{e}_{\mathbf{k}_a}(\mathbf{r}_i)$ ($a = 1, 2, 3$) defined similarly (see Appendix B.1, Table B.1), we introduce the order parameter ψ_a for a particular ordering wave vector \mathbf{k}_a as

$$\psi_a = \frac{1}{N} \sum_i \langle \mathbf{S}_i \rangle \cdot \hat{e}_{\mathbf{k}_a}(\mathbf{r}_i). \quad (4.2)$$

The summation goes over all N sites of the pyrochlore lattice and $\boldsymbol{\psi} \equiv (\psi_0, \dots, \psi_3)$ defines a 4-dimensional order parameter vector.

For a wide range of $(J, J_{\text{DM}}, J_{\text{Ising}}, J_{\text{pd}}, J_{\text{dip}}, J_2, J_3)$ couplings, s-MFT predicts a second order transition with ordering at momenta \mathbf{k}_a . Interestingly, we find that up to quartic order in the $\{\psi_a\}$ order parameters, the s-MFT free-energy displays an *emergent* $O(4)$

symmetry. (see Appendix B.4 for details) However, the $O(4)$ symmetry is spoiled at higher order in $\{\psi_a\}$, *no* selection of $1\text{-}\mathbf{k}$ (which has only one $\psi_a \neq 0$) vs $4\text{-}\mathbf{k}$ (which has four ψ_a with the same nonzero amplitude) occurs *at any* order. The proof is presented in Appendix B.2. The observation of an emergent $O(4)$ symmetry at quartic order in s-MFT helps us to recognize that an underlying effective “cubic anisotropy” in the $\{\psi_a\}$ is the most relevant symmetry-allowed perturbation. We therefore proceed to write the Ginzburg-Landau free-energy, $\mathcal{F}_{\text{GL}}(\{\psi_a\})$, of the system constructed in terms of the four order parameters ψ_a ($a = 0, 1, 2, 3$). Each $1\text{-}\mathbf{k}$ order is a spin-density wave and ψ_a is the amplitude of the wave. The four order parameters ψ_a form the components of a four-dimensional vector which fully describes the long-range order at the four $\{\frac{1}{2}\frac{1}{2}\frac{1}{2}\}$ momenta.

To construct the Ginzburg-Landau free-energy, we study how ψ_a transforms under the space group symmetry of the pyrochlore lattice. Based on the direct space spin configurations illustrated in Fig. 4.1, we obtain how ψ_a transforms. Under threefold rotations about the local $[111]$ direction of, say, the 0^{th} sublattice (see Eq. (A.1)), three of ψ_a 's are permuted: $\psi_1 \rightarrow \psi_2$, $\psi_2 \rightarrow \psi_3$ and $\psi_3 \rightarrow \psi_1$. Under a primitive FCC lattice translation, $\mathbf{r} \rightarrow \mathbf{r} + \hat{x}/2 + \hat{y}/2$ for example, two ψ_a 's, in this case ψ_0 and ψ_3 , reverse sign. All ψ_a 's reverse sign under time-reversal transformation. Lastly, the point inversion about a site on the a sublattice flips the sign of ψ_a while leaving the other three order parameters intact. Since the symmetry operation is responsible for the elimination of a term of the form $\psi_0\psi_1\psi_2\psi_3$ in free-energy invoked in Ref.[85], we demonstrate its consequence in detail here. Considering the $1\text{-}\mathbf{k}$ structure with momentum \mathbf{k}_0 , the point inversion about a site on sublattice 0 exchanges the spin configurations on adjacent kagome layers, which have opposite directions. As a result, $\psi_0 \rightarrow -\psi_0$. On the other hand, the point inversion about a site on any other sublattice than 0 leaves the $1\text{-}\mathbf{k}$ structure of \mathbf{k}_0 intact. In other words, such a transformation leaves ψ_0 unchanged. Similar arguments can be made for \mathbf{k}_a with $a = 1, 2, 3$. Consequently, $\psi_0\psi_1\psi_2\psi_3$ is odd under point inversion symmetry and not allowed in \mathcal{F}_{GL} .

We now construct the Ginzburg-Landau free-energy to quartic order. At the quadratic order, the only invariant term is $\sum_{a=0}^3 \psi_a^2$. At quartic order, there are two terms that are invariant under the above symmetry transformations: $(\sum_{a=0}^3 \psi_a^2)^2$ and $\sum_{a=0}^3 \psi_a^4$. We thus write down the Ginzburg-Landau free-energy:

$$\mathcal{F}_{\text{GL}} = \frac{1}{2}r \sum_{a=0}^3 \psi_a^2 + u \left(\sum_{a=0}^3 \psi_a^2 \right)^2 + v \sum_{a=0}^3 \psi_a^4. \quad (4.3)$$

In what follows, we make use of the following quantities:

$$\boldsymbol{\psi} \equiv (\psi_0, \psi_1, \psi_2, \psi_3), \quad (4.4a)$$

$$|\boldsymbol{\psi}| = \sqrt{\sum_{a=0}^3 \psi_a^2}, \quad (4.4b)$$

$$\hat{\boldsymbol{\psi}} \equiv \frac{\boldsymbol{\psi}}{|\boldsymbol{\psi}|}. \quad (4.4c)$$

Here, $\boldsymbol{\psi}$ is the 4-component vector order parameter and $|\boldsymbol{\psi}|$ is its magnitude. $\hat{\boldsymbol{\psi}}$ is a 4-component unit vector parallel to $\boldsymbol{\psi}$ which is convenient to parametrize the behaviour of the system below the critical temperature, T_c , in the Monte Carlo simulations discussed in Section 4.4 below.

Eq. (4.3) is the celebrated n -vector model ($n = 4$) with cubic anisotropy [64] with $r = a_0(T - T_c)$ and $a_0 > 0$. This model, a cornerstone of the theory of critical phenomena [64, 102], has been extensively investigated with numerous methods [103, 104, 105, 106]. In 3D, for $n > n_c \approx 2.89$ and $u > 0$ [106], the model undergoes a second-order transition into a phase where all ψ_a have the same amplitude if $v > 0$ [64]. The universality class is controlled by the cubic fixed point [64] with distinct critical exponents from those of the isotropic $O(n)$ fixed point [102, 106]. We note that the continuous nature of the phase transition depends on the condition $u > 0$ ¹ [107]. For $u > 0$, $v < 0$, the phase transition is a fluctuation-induced first-order transition to a state with only one nonzero ψ_a [64]. Therefore, we conclude that for $v > 0$ the magnetic order is defined by a superposition of four \mathbf{k}_a spin states (4- \mathbf{k} state) while for $v < 0$ the order is defined by a single \mathbf{k}_a spin structure (1- \mathbf{k} state). Both states are POSs since the spins on 1/4 of the sites remain disordered (see Fig. 4.1). As stated above, s-MFT predicts that 1- \mathbf{k} and 4- \mathbf{k} have the same \mathcal{F}_{GL} (i.e. $v = 0$). We thus identify thermal *fluctuations* as the *microscopic* mechanism for generating $v \neq 0$ which then leads to a selection of 1- \mathbf{k} vs 4- \mathbf{k} . To expose how fluctuations may lead at the microscopic level to a selection *directly at* T_c , we devise and then use an E-TAP method [68, 66, 108].

¹If $u < 0$, the transition is first order and terms to sixth order (or higher) should be included in the Ginzburg-Landau free-energy to ensure stability of the ordered phase i.e. to ensure a minimum free-energy state with finite $|\boldsymbol{\psi}|$. [107]

4.3 Extended TAP method

In this section, we devise the E-TAP method in the form of a series originating from nonzero on-site fluctuations, e.g. $\langle S_i^\alpha S_i^\beta \rangle \neq \langle S_i^\alpha \rangle \langle S_i^\beta \rangle$ [68, 108]. The third term in the series, presented in Eq. (3.24), $\Omega \equiv \tilde{G}'''(0)\beta/2$, is the first correction beyond s-MFT, arising from fluctuations [68] and reads as:

$$\Omega = -\frac{\beta}{4} \sum_{i,j} \sum_{\alpha\beta\gamma\delta} J_{ij}^{\alpha\gamma} J_{ij}^{\beta\delta} \chi_i^{\alpha\beta} \chi_j^{\gamma\delta}. \quad (4.5)$$

Here, $\chi_i^{\alpha\beta} = \langle S_i^\alpha S_i^\beta \rangle - \langle S_i^\alpha \rangle \langle S_i^\beta \rangle$ is the on-site susceptibility. To calculate $\chi_i^{\alpha\beta}$ in Eq. (4.5), we differentiate Eq. (3.36) with respect to λ_i^α . This gives:

$$\chi_i^{\alpha\beta} = -\frac{\delta_{\alpha\beta}}{3} \left(1 - \frac{|\boldsymbol{\lambda}_i|^2}{15}\right) + \frac{2}{25} \frac{\lambda_i^\alpha \lambda_i^\beta}{3} + \dots, \quad (4.6)$$

where \dots means higher order terms.

According to the general discussion pertaining to the Ginzburg-Landau theory presented above, we are foremost interested in the quartic terms in $|\boldsymbol{\lambda}_i|$ and λ_i^α . As we explained below, these are the ones that lead to a selection between $1\text{-}\mathbf{k}$ and $4\text{-}\mathbf{k}$ states on which we henceforth focus. We substitute Eq. (4.6) for $\chi_i^{\alpha\beta}$ and $\chi_j^{\gamma\delta}$ in Eq. (4.5). The following subset of terms are found to be potentially able to differentiate between $1\text{-}\mathbf{k}$ and $4\text{-}\mathbf{k}$ states at the quartic order:

$$\Omega_1 = -\beta \frac{1}{4(45)^2} \sum_{ij} |\boldsymbol{\lambda}_i|^2 |\boldsymbol{\lambda}_j|^2 \sum_{\gamma\delta} (J_{ij}^{\gamma\delta})^2, \quad (4.7)$$

$$\Omega_2 = -\beta \frac{1}{(45)^2} \sum_{ij} \sum_{\alpha\gamma\delta} J_{ij}^{\alpha\gamma} J_{ij}^{\alpha\delta} |\boldsymbol{\lambda}_i|^2 \lambda_j^\gamma \lambda_j^\delta, \quad (4.8)$$

$$\Omega_3 = -\beta \frac{1}{(45)^2} \sum_{ij} \sum_{\alpha\beta\gamma\delta} J_{ij}^{\alpha\beta} J_{ij}^{\gamma\delta} \lambda_i^\alpha \lambda_i^\gamma \lambda_j^\beta \lambda_j^\delta. \quad (4.9)$$

To calculate these terms, we wrote a computer program which directly calculates the sums by calculating $\boldsymbol{\lambda}_i$ for $1\text{-}\mathbf{k}$ and $4\text{-}\mathbf{k}$. The $J_{ij}^{\mu\nu}$ couplings are explicitly known through the Hamiltonian of Eq. (4.1) and the Ewald summation method is used to compute the contribution from the long-range dipolar interaction (Eq. (4.1c)). The reason these terms

can distinguish between $1\text{-}\mathbf{k}$ and $4\text{-}\mathbf{k}$ is because they can not be reduced to onsite terms, an effect that happens with the lower order terms in the expansion with respect to β , i.e., the first two terms in Eq. (3.24), which constitute the s-MFT free-energy.

Since $\chi_i^{\alpha\beta}$ is quadratic in $\{\psi_a\}$, Ω in Eq. (4.5) is therefore of *quartic order* in $\{\psi_a\}$. The first order E-TAP correction, Ω , can thus, in principle, generate a finite cubic anisotropy term in \mathcal{F} and select $1\text{-}\mathbf{k}$ or $4\text{-}\mathbf{k}$ depending on the bilinear spin-spin interaction matrix $J_{ij}^{\alpha\beta}$ defined through $\mathcal{H} \equiv \sum_{(i>j);\alpha,\beta} J_{ij}^{\alpha\beta} S_i^\alpha S_j^\beta$ in Eq. (5.1).

We calculate Ω for the region in parameter space with $(\frac{1}{2}\frac{1}{2}\frac{1}{2})$ ordering (the dark-shaded $1\text{-}\mathbf{k}/4\text{-}\mathbf{k}$ wedge in Fig. 4.4). Specifically, we compute $\delta\Omega \equiv \Omega_{1\mathbf{k}} - \Omega_{4\mathbf{k}}$. $\delta\Omega < 0$ indicates a $1\text{-}\mathbf{k}$ selection and conversely for $\delta\Omega > 0$, with the Ω contribution splitting the wedge into $1\text{-}\mathbf{k}$ and $4\text{-}\mathbf{k}$ sectors. In particular, for a dipolar Heisenberg model with $J_{\text{Ising}} = J_{\text{DM}} = J_{\text{pd}} = 0$, relevant to $\text{Gd}_2\text{Ti}_2\text{O}_7$ [83], E-TAP calculations predict a $4\text{-}\mathbf{k}$ state selection at T_c , as reported in this compound [19].

4.4 Monte Carlo simulations

We performed Monte Carlo simulations of three-component classical spins on the pyrochlore lattice to check the E-TAP predictions of the $1\text{-}\mathbf{k}$ versus $4\text{-}\mathbf{k}$ selection mechanism in the Hamiltonian of Eq. (4.1). We used the parallel tempering[63] method to assist with thermal equilibration. The simulations were performed for three system sizes $L = 4, 6, 8$ where the system is composed of L^3 conventional cubic unit cells and each cell contains 16 lattice sites (pyrochlore structure). Even system sizes L are required for the simulation cell to be commensurate with $(\frac{1}{2}\frac{1}{2}\frac{1}{2})$ spin density wave order. To account for the long-range dipolar interaction, we employed the Ewald summation method [56, 109]. For each temperature considered, about 10^8 spin flips per spin were attempted while maintaining an average acceptance of approximately 50%².

We pick, somewhat arbitrarily, two sets of interaction parameters corresponding to the $1\text{-}\mathbf{k}$ and $4\text{-}\mathbf{k}$ regions in Fig. 4.4. One set is the simplest model for a spin-only ${}^8S_{7/2}$ ($L = 0$, $S = 7/2$, $J = L + S$) state for Gd^{3+} in $\text{Gd}_2\text{Ti}_2\text{O}_7$, with $J_{\text{dip}}/J = 0.18$ [83], $J_{\text{Ising}} = J_{\text{DM}} = J_{\text{pd}} = 0$. We include, as in a previous Monte Carlo work [85], weak ferromagnetic second nearest neighbours interaction (e.g. $-0.02J \lesssim J_2 < 0$) to stabilize a temperature range wide enough to numerically resolve $(\frac{1}{2}\frac{1}{2}\frac{1}{2})$ order (see [85] and Appendix C). In our simulations, we measure $|\psi|^2$ defined in Eq. (4.4c).

²In parallel tempering process, a replica swap attempted after about 10^3 spin flip attempts per single spin

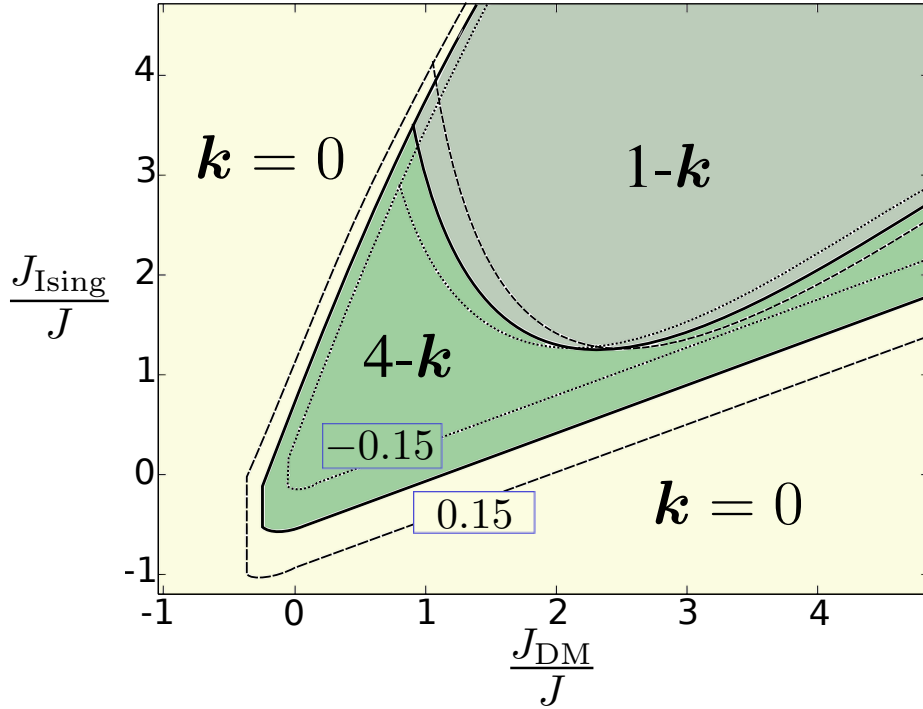


Figure 4.4: Ordering wave vectors at $T = T_c$ obtained from s-MFT with $J_{dip} = 0.18$. The combined area denoted $1-k$ and $4-k$ displays $(\frac{1}{2}\frac{1}{2}\frac{1}{2})$ order but $1-k$ and $4-k$ are degenerate at the s-MFT level. The first order E-TAP correction Eq. (4.5) applied in this regime selects either $1-k$ or $4-k$. The $k=0$ region encompasses all states for which all sites are fully ordered and each primitive 4-site tetrahedron basis has the same local spin order. The dashed (0.15) and dotted (-0.15) contours mark the boundaries for the corresponding J_{pd} values.

In addition to the magnitude of $\boldsymbol{\psi}$, we need to identify the orientation of $\boldsymbol{\psi}$ at $T < T_c$ through two additional order parameters, $d_{i\mathbf{k}}$ ($i = 1, 4$) defined below, in order to distinguish between the $1\text{-}\mathbf{k}$ and $4\text{-}\mathbf{k}$ states. To do so, we consider the 4-dimensional ($4D$) Euclidian space spanned by the four $1\text{-}\mathbf{k}$ states. In this $4D$ space, on the surface of a four-dimensional unit hyper-sphere, there are eight “ $1\text{-}\mathbf{k}$ points” corresponding to $1\text{-}\mathbf{k}$ states (4 of them are defined in Table B.1 and 4 are the time-reversed of those), which can be represented as:

$$\hat{p}_{1\mathbf{k}} = (\pm 1, 0, 0, 0), (0, \pm 1, 0, 0), (0, 0, \pm 1, 0), (0, 0, 0, \pm 1). \quad (4.10)$$

These points reside on the 4 axes of this $4D$ space.

Since the $4\text{-}\mathbf{k}$ states are linear combinations of the $1\text{-}\mathbf{k}$ states with coefficients $\hat{\psi}_a = \pm \frac{1}{2}$ (see Appendix B.1, Eq.(B.2)), there are sixteen points corresponding to them

$$\{\hat{p}_{4\mathbf{k}}\} = \left(\pm \frac{1}{2}, \pm \frac{1}{2}, \pm \frac{1}{2}, \pm \frac{1}{2} \right). \quad (4.11)$$

In the simulation, we measured ψ_a defined in the Eq. (4.2):

$$\psi_a(\tau) = \frac{1}{N} \sum_i \mathbf{S}_i(\tau) \cdot \hat{\mathbf{e}}_{\mathbf{k}_a}(\mathbf{r}_i), \quad (4.12)$$

where $\psi_a(\tau)$ corresponds to the value of ψ_a at the Monte Carlo step τ and $a = 0, \dots, 3$. $\hat{\mathbf{e}}_{\mathbf{k}_a}(\mathbf{r}_i)$ is given by Eq. (B.1). Consequently, the order parameter corresponding to $\{\frac{1}{2}\frac{1}{2}\frac{1}{2}\}$ ordering wave vectors, can be represented in the $4D$ space as:

$$|\boldsymbol{\psi}(\tau)|^2 = \left\langle \sum_{a=0}^3 \psi_a(\tau)^2 \right\rangle_{\tau}. \quad (4.13)$$

where $\langle \dots \rangle_{\tau}$ represents a Monte Carlo average. Since we foremost care about the orientation of this vector in the $4D$ space which signals whether the $1\text{-}\mathbf{k}$ or $4\text{-}\mathbf{k}$ state is selected, once $|\boldsymbol{\psi}(\tau)|$ acquires a finite value at $T < T_c$, we define:

$$\hat{\psi}(\tau) = \frac{1}{\sqrt{\sum_{a=0}^3 \psi_a^2}} (\psi_0(\tau), \psi_1(\tau), \psi_2(\tau), \psi_3(\tau)). \quad (4.14)$$

from which we define:

$$\tilde{d}_{1\mathbf{k}/4\mathbf{k}}(\tau) \equiv |\hat{\psi}(\tau) - \hat{p}_{1\mathbf{k}/4\mathbf{k}}|, \quad (4.15)$$

At a particular temperature, at each τ instance, eight and sixteen values are obtained for $\tilde{d}_{1\mathbf{k}}(\tau)$ and $\tilde{d}_{4\mathbf{k}}(\tau)$, respectively. The minimum value among those eight/sixteen determines $d_{1\mathbf{k}}^{\min}(\tau)$ and $d_{4\mathbf{k}}^{\min}(\tau)$. We then define $d_{1\mathbf{k}/4\mathbf{k}}$ at temperature T as

$$d_{1\mathbf{k}/4\mathbf{k}} = \langle d_{1\mathbf{k}/4\mathbf{k}}^{\min}(\tau) \rangle_{\tau}, \quad (4.16)$$

which we refer to as the *distance* parameter at the temperature considered. The results for $|\boldsymbol{\psi}|^2$ and $d_{1\mathbf{k}/4\mathbf{k}}$ are presented in Fig. 4.5. By construct, the thermal average of $d_{1\mathbf{k}}$ ($d_{4\mathbf{k}}$) is expected to decrease if the system enters a $1\text{-}\mathbf{k}$ ($4\text{-}\mathbf{k}$) state for $T < T_c$.

The results for two sets of interaction parameters in the $1\text{-}\mathbf{k}$ and $4\text{-}\mathbf{k}$ regions of Fig. 4.4 are shown in the left and right columns of Fig. 4.5, respectively. The growth of $|\boldsymbol{\psi}|^2$ at $T_c/J \sim 5.5$ and $T_c/J \sim 0.15$ shows that the system orders with $\mathbf{k} = (\frac{1}{2}\frac{1}{2}\frac{1}{2})$. In the left column, the $1\text{-}\mathbf{k}$ state is selected at T_c , as indicated by a minimum for $d_{1\mathbf{k}}$ and a maximum for $d_{4\mathbf{k}}$. The system orders in a $4\text{-}\mathbf{k}$ state in the right column. The separation of $d_{1\mathbf{k}}$ and $d_{4\mathbf{k}}$ for both cases in Fig. 4.5 accentuates as the linear dimension L of the system increases, indicating that the selection of either $1\text{-}\mathbf{k}$ or $4\text{-}\mathbf{k}$ survives in the thermodynamics limit. These results are consistent with the predictions from the E-TAP calculations at T_c . Unfortunately, the large computational resources required for simulations with long-range dipolar interactions prevent us from investigating the order of the phase transitions in Fig. 4.5.

The kinks in $|\boldsymbol{\psi}|^2$ and merging of $d_{1\mathbf{k}}$ and $d_{4\mathbf{k}}$ indicate the system enters into a distinct phase at $T/J \lesssim 4$ and $T/J \lesssim 0.1$ in the left and right columns of Fig. 4.5. Since in a $2\text{-}\mathbf{k}$ state $d_{1\mathbf{k}} \equiv d_{4\mathbf{k}} = \sqrt{2 - \sqrt{2}} \simeq 0.765$, the results for $d_{i\mathbf{k}}$ suggest that the low-temperature region may be a $2\text{-}\mathbf{k}$ state. To demonstrate this, consider the four-dimensional unit vector $\hat{\psi}$. The $4\text{-}\mathbf{k}$ state corresponds to $\hat{\psi}^{(4)} = (1/2, 1/2, 1/2, 1/2)$ while the $1\text{-}\mathbf{k}$ state has $\hat{\psi}^{(1)} = (1, 0, 0, 0)$. It is straightforward algebra to show the $2\text{-}\mathbf{k}$ state, $\hat{\psi} = (1/\sqrt{2}, 1/\sqrt{2}, 0, 0)$ has $d_{1\mathbf{k}} = d_{4\mathbf{k}} = \sqrt{2 - \sqrt{2}}$. We also measured $d_{2\mathbf{k}}$ in our Monte Carlo simulations for the two sets of parameters chosen above. The results are shown in Fig. 4.6. Upon lowering the temperature below $4.0J$ ($0.1J$) for the point in $1\text{-}\mathbf{k}$ ($4\text{-}\mathbf{k}$) region of Fig. 4.4, $d_{2\mathbf{k}}$ decreases. This effect is enhanced in larger system sizes indicating the lower temperature phase of the models corresponding to these two sets of parameters is indeed a $2\text{-}\mathbf{k}$ state. This result is not in agreement with the low temperature phase of $\text{Gd}_2\text{Ti}_2\text{O}_7$ reported in Ref. [19] (see Fig. 4.7³).

We note that the latest single-crystal neutron diffraction results [110] indicate that the low-temperature state ($T < 0.7$ K) of $\text{Gd}_2\text{Ti}_2\text{O}_7$ *may not* be the previously suggested

³Where a modified version of $4\text{-}\mathbf{k}$ state is reported, in which the 1/4 of disordered spins in Fig. 4.1b start ordering, without fully saturating as the system approaches zero temperature, while the ordered ones start canting with respect to their initial direction.

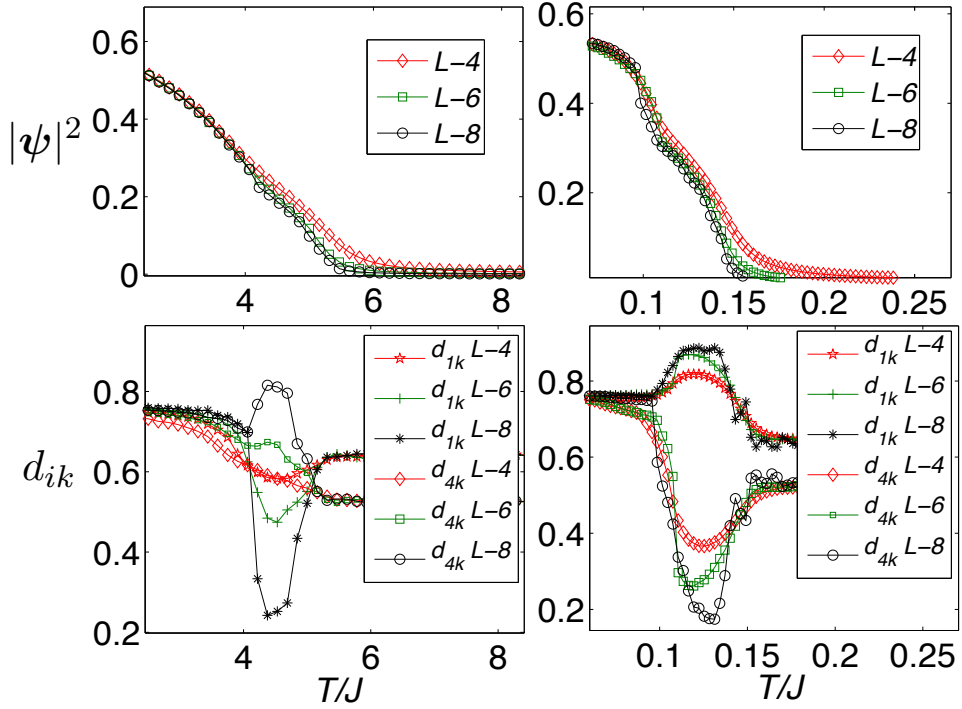


Figure 4.5: Monte Carlo simulations results. *Top row:* growth of $|\psi|^2$. *Bottom row:* value of $d_{i\mathbf{k}}$ as a function of T/J . **Left column:** $J_{\text{pd}} = 0$, $J_{\text{dip}}/J = 0.18$, $J_2/J = -1$, $J_{\text{Ising}}/J = 10$, $J_{\text{DM}}/J = 10$ (direct DM) and $J_3/J = 1$ (a point in $1\text{-}\mathbf{k}$ region). **Right column:** $J_{\text{pd}} = J_{\text{DM}} = J_{\text{Ising}} = 0$, $J_{\text{dip}}/J = 0.18$ and $J_2/J = -0.02$ (a point in $4\text{-}\mathbf{k}$ region). Note: The $d_{i\mathbf{k}}$ are nonzero in the paramagnetic phase because their value is equal to the average distance of a random point on a 4-dimensional hypersphere from the $1\text{-}\mathbf{k}$ and $4\text{-}\mathbf{k}$ points. We note that separation of $d_{1\mathbf{k}}$ and $d_{4\mathbf{k}}$ for both cases accentuates as the linear dimension L of the system increases, indicating that the selection of either $1\text{-}\mathbf{k}$ or $4\text{-}\mathbf{k}$ survives in the thermodynamics limit.

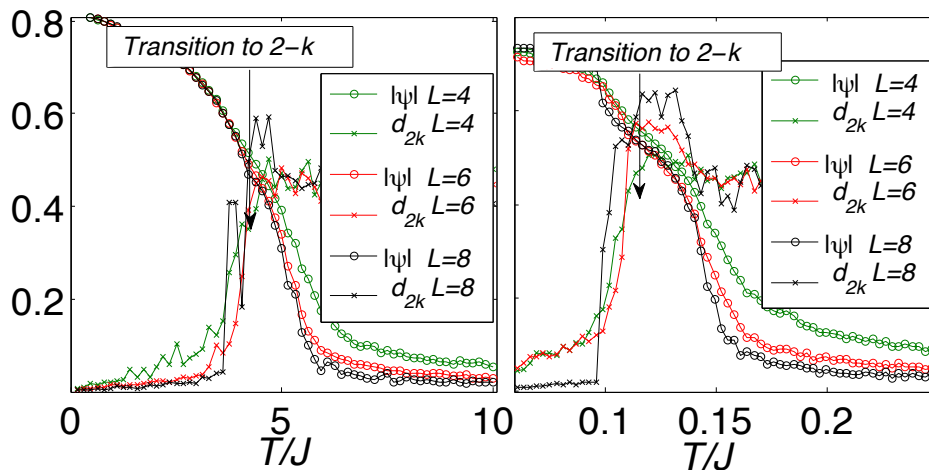


Figure 4.6: Monte Carlo simulations results. Circles show growth of $|\psi|$, and crosses value of $d_{2\mathbf{k}}$ as a function of T/J . **Left panel:** $J_{\text{pd}} = 0$, $J_{\text{dip}}/J = 0.18$, $J_2/J = -1$, $J_{\text{Ising}}/J = 10$, $J_{\text{DM}}/J = 10$ (direct DM) and $J_3/J = 1$ (a point in $1\text{-}\mathbf{k}$ region). **Right panel:** $J_{\text{pd}} = J_{\text{DM}} = J_{\text{Ising}} = 0$, $J_{\text{dip}}/J = 0.18$ and $J_2/J = -0.02$ (a point in $4\text{-}\mathbf{k}$ region).

modified $4\text{-}\mathbf{k}$ structure [19]. Whether the $2\text{-}\mathbf{k}$ state obtained in our simulation, is the low temperature phase of $\text{Gd}_2\text{Ti}_2\text{O}_7$, awaits further experimental efforts and more in-depth numerical investigations.

4.5 Discussion

Having considered a general symmetry-allowed anisotropic Hamiltonian, we found that $\mathbf{k} = (\frac{1}{2}\frac{1}{2}\frac{1}{2})$ partial order can occur over a wide range of anisotropic bilinear and long-range dipolar interactions in pyrochlore magnets. We argued that fluctuations beyond s-MFT are responsible for the stabilization of a $1\text{-}\mathbf{k}$ or $4\text{-}\mathbf{k}$ partially ordered structure. This conclusion is based on results from E-TAP calculations where on-site fluctuations are included. We used Monte Carlo simulations to illustrate that different values of the magnetic exchange interactions can, as anticipated on the basis of the E-TAP calculations, lead to either $1\text{-}\mathbf{k}$ or $4\text{-}\mathbf{k}$ order.

From our work, we have exposed a likely mechanism for the establishment of $4\text{-}\mathbf{k}$ order in $\text{Gd}_2\text{Ti}_2\text{O}_7$ below its paramagnetic transition [19]. Further quantitative progress on

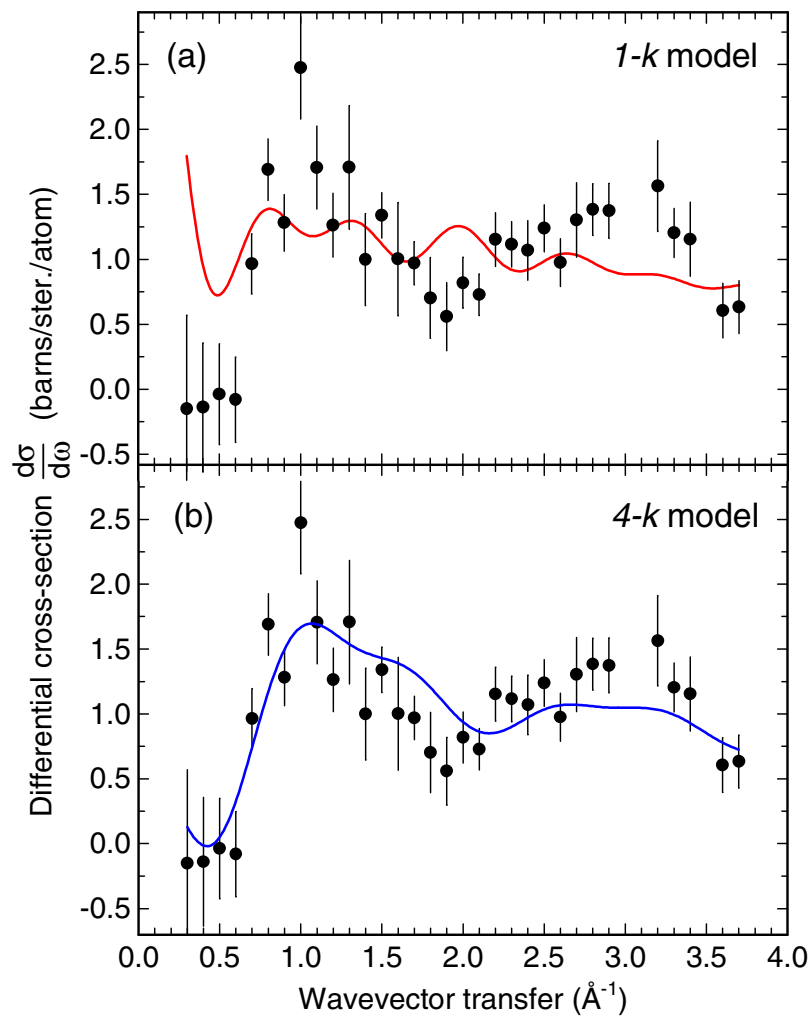


Figure 4.7: Reproduced from Ref. [19]. Black dots represent magnetic diffuse neutron scattering data from $\text{Gd}_2\text{Ti}_2\text{O}_7$ measured at $T = 46$ mK. The (a) red and (b) blue curves are fits to the experimental data for $1\text{-}\mathbf{k}$ and $4\text{-}\mathbf{k}$ models. Based on the above results it is concluded that the low temperature phase of $\text{Gd}_2\text{Ti}_2\text{O}_7$ has a $4\text{-}\mathbf{k}$ structure.

this problem will require a better estimate of the couplings of Eq. (4.1) corresponding to the material [21, 41, 44]. From this work we conclude that the transition from the paramagnetic state to the $4\text{-}\mathbf{k}$ phase should be second order and belong to the $3D$ $n = 4$ cubic universality class, according to the Ginzburg-Landau analysis presented in Section 4.2 which indicates the $4\text{-}\mathbf{k}$ state arises only in the $u, v > 0$ regime of the 4-vector model. Experimental evidence [93] suggests that this transition is second order in $\text{Gd}_2\text{Ti}_2\text{O}_7$ [11]. Determining the critical exponents for this system could confirm our prediction but will be a challenge, given that the exponents for the $3D$ $n = 4$ cubic and $3D$ Ising, XY and Heisenberg universality classes are proximate to one another [102, 106].

In the next chapter, we discuss the problem of the ObD selection at $T = T_c^-$ in another region of the parameter space of the Hamiltonian of Eq. (4.1) where $U(1)$ symmetry emerges at the s-MFT level. The $U(1)$ symmetry is broken by a hexagonal anisotropy introduced in the free-energy via thermal fluctuations that arise beyond s-MFT.

Chapter 5

Emergent $U(1)$ Symmetry Breaking by Thermal Fluctuations – a method exploration

Moving along the path we embarked on in Chapter 4 to explore the ObD phenomenon at $T = T_c^-$, in this chapter, we investigate this phenomenon in a system of 3D XY spins on the pyrochlore lattice interacting via a bilinear anisotropic spin Hamiltonian. At the standard mean field theory (s-MFT) level, in a certain region of the parameter space of this Hamiltonian that we shall refer to as Γ_5 *region* for shorthand, the ordered state possesses an accidental $U(1)$ degeneracy. We show that fluctuations beyond s-MFT lift this degeneracy, exposing a certain form of ObD and selecting either the ψ_2 or the ψ_3 states from the degenerate manifold (see Fig. 5.1 for definitions of these states). Similar to our approach in Chapter 4, we analytically explore this selection at the microscopic level and close to criticality, $T = T_c^-$, by elaborating upon and using the E-TAP method. We obtain the phase diagram resulting from the ObD selection. Interestingly, the E-TAP method predicts a weak fluctuation-induced magnetic moment in the z direction of the local $\langle 111 \rangle$ coordinate system when ObD selects the ψ_2 state. This induced z moment has heretofore been missed by previous theoretical studies of XY pyrochlore magnets.

5.1 Introduction

Recently, several studies [20, 21, 30, 31, 32] have put forward compelling arguments for ObD being responsible for the experimentally observed long-range order in the rare-earth

pyrochlore oxide $\text{Er}_2\text{Ti}_2\text{O}_7$. The key observation in those works is that the degenerate classical ground states are related by operations of an emergent $U(1)$ symmetry [21]. This set of classically degenerate states form the so-called Γ_5 manifold [111]. For a range of interaction parameters of the most general symmetry allowed bilinear spin-spin Hamiltonian on the pyrochlore lattice (mg-Hamiltonian), the emergent $U(1)$ degeneracy is exact at the s-MFT level as long as the cubic symmetry of the material remains intact. We henceforth refer to this region of the parameter space as the Γ_5 region. Based on the robustness of the $U(1)$ symmetry, Ref. [21] argued that essentially *only* fluctuations can lift the degeneracy in $\text{Er}_2\text{Ti}_2\text{O}_7$.¹ In this compound, a particular long-range ordered state, the ψ_2 state (see Fig. (5.1)) [111, 112, 113, 114, 115], is selected. In continuation of previous studies and considering the mg-Hamiltonian, Wong *et al.* and Yan *et al.* further studied the effect of fluctuations and established a general phase diagram for this Hamiltonian at $T = 0^+$ [31, 33]. In this chapter we have a similar goal but for the $T \lesssim T_c$ regime.

The investigations reported in Refs. [20, 21, 30, 31] focused on identifying the mechanism of selection of the *ground state* by taking into account the harmonic quantum spin fluctuations about a classical long-range ordered state. As pointed out in Chapter 1, apart from the selection of *the ground state* by fluctuations, the problem of ObD selection at $T = T_c^-$ stands on its own and, to the best of our knowledge, has not received as much attention. In the temperature regime near a phase transition, the harmonic approximation often employed in theoretical discussions of ObD at $T = 0^+$ is not physically justified since large fluctuations typically accompany the transition [64]. From a fundamental viewpoint, it is thus highly desirable to study the role of fluctuations beyond s-MFT using a different method at temperatures close to the critical region. A possible route to tackle this problem is the E-TAP method as it captures corrections to the s-MFT free-energy by including fluctuations in the form of on-site linear and nonlinear susceptibilities.

In this chapter, we explore the problem of ObD selection near criticality in a model of XY spins on the pyrochlore lattice using E-TAP, which has been used in Chapter 4 to investigate the partial multiple- \mathbf{k} order in pyrochlore magnets [35]. We concentrate on the Γ_5 manifold for the $T \lesssim T_c^{\text{MF}}$ regime since the manifold is not only an interesting theoretical playground according to recent investigations of ObD in the $T = 0^+$ regime, [31, 33], it is also of potential relevance to real materials proposed to display an ObD mechanism [20, 21, 112]. In addition, the interesting case of distinct ObD selection at $T = 0^+$ and T_c has been reported in a pyrochlore system with anisotropic spin-spin coupling [34, 116]. This intriguing phenomena further motivates us to investigate a general model of XY spins

¹It has been pointed out by McClarty *et al.* that ψ_2 state can be energetically selected through van Vleck-like mechanisms [42]. Ref. [21] argues that this mechanism is not strong enough to be at play in $\text{Er}_2\text{Ti}_2\text{O}_7$. However, this remains to be explicitly demonstrated both theoretically and experimentally

on pyrochlore lattice. In what follows, we aim to help shed light on the broad theoretical problem of ObD selection at $T \lesssim T_c$ in a general model pertinent to real pyrochlore materials [11].

The rest of this chapter is organized as follows. In Section 5.2, we present the mg-Hamiltonian and discuss its symmetries. Focusing on the Γ_5 manifold with its $U(1)$ degeneracy, we present a Ginzburg-Landau (GL) symmetry analysis to specify the general form of the anisotropic terms allowed in the GL free-energy (\mathcal{F}_{GL}) that can lift the accidental $U(1)$ degeneracy. We show that the fluctuation correction terms to the standard mean field theory (s-MFT) free-energy select either the ψ_2 or the ψ_3 state of the Γ_5 manifold (see Fig. 5.1 and Appendix D for definition) and induce a local m_z moment to the ψ_2 state. In Section 5.3, we present the E-TAP method and calculate the phase boundary between ψ_2 and ψ_3 states in the space of spin-spin coupling constants. A discussion is presented in Section 5.4. Related to the topics discussed in this chapter, in Appendix D we present the spin configurations of ψ_2 and ψ_3 states and in Appendix E, we provide the details of diagrammatic approach used for the E-TAP calculations for the present problem.

5.2 Model

We consider the mg-Hamiltonian [44]:

$$\mathcal{H}_{\text{mn}} = \mathcal{H}_0 + \mathcal{H}_1 \quad (5.1a)$$

$$\mathcal{H}_0 = \sum_{\langle ij \rangle} J_{zz} S_i^z S_j^z - J_{\pm} (S_i^+ S_j^- + S_i^- S_j^+) \quad (5.1b)$$

$$\begin{aligned} \mathcal{H}_1 &= \sum_{\langle ij \rangle} J_{\pm\pm} (S_i^+ S_j^+ \gamma_{ij} + S_i^- S_j^- \gamma_{ij}^*) \\ &+ J_{z\pm} \{ S_i^z (\zeta_{ij} S_j^+ + \zeta_{ij}^* S_j^-) + i \leftrightarrow j \} \end{aligned} \quad (5.1c)$$

where $S_i^{\pm} \equiv S_i^x \pm i S_i^y$ and S_i^{μ} with $\mu = z, +, -$ is defined in the local $\langle 111 \rangle$ coordinate frame [44] attached to each of the four pyrochlore sublattices (see Fig. 5.1). \mathbf{S}_i can be treated classically as a 3-component vector or quantum mechanically as an $|\mathbf{S}| = 1/2$ operator. We note that in material-relevant contexts, \mathbf{S}_i would represent either the total angular momentum \mathbf{J} , or the pseudo-spin depending on the energy spectrum of the crystal electric field in the specific material of interest [11, 20, 21, 41, 46, 117]. As we are foremost interested in the selection of ordered phases at $0 \ll T \lesssim T_c$ in this Chapter and thesis, we shall treat \mathbf{S}_i generally classically, where $|\mathbf{S}_i| = 1/2$ for all i . In Eq. (5.1), $J_{zz}, J_{\pm}, J_{\pm\pm}, J_{z\pm}$ are the four symmetry-allowed independent exchange parameters, while $\zeta_{ij} = -\gamma_{ij}^*$ are

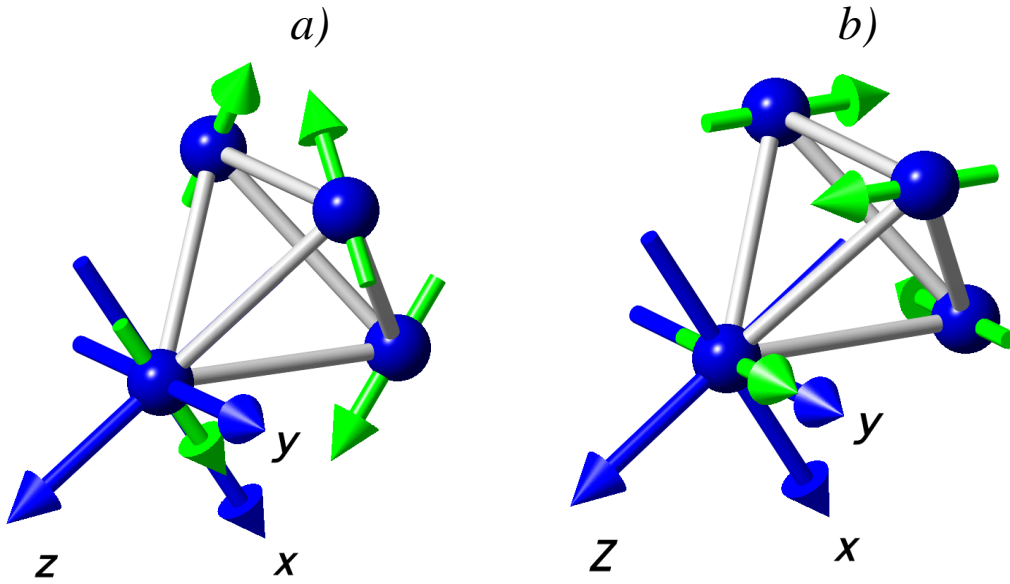


Figure 5.1: Spin configurations of the (a) non-coplanar ψ_2 state and the (b) coplanar ψ_3 state on a single tetrahedron. These states belong to the Γ_5 manifold: a set of states with a $\mathbf{k} = 0$ wave vector and all the magnetic moments in the system lie in the xy plane of their local $[111]$ coordinate system pointing in the same local direction. The spin (in blue) at each site points along (a) x axis and (b) y axis of the local $[111]$ reference frame which is illustrated by blue arrows for one sublattice labelled by the xyz triad. See Appendix D for more details.

bond dependant phases on a single tetrahedron [21, 118]. We note that the Hamiltonian in Eq. (5.1) is related to the Hamiltonian of Eq. (4.1) by a linear transformation presented in Appendix F.

\mathcal{H}_0 has a $U(1)$ symmetry: it is invariant under a rotation of \mathbf{S}_i by an arbitrary angle about the local $\langle 111 \rangle$ axes. On the other hand, the \mathcal{H}_1 term in Eq. (5.1a) reduces this $U(1)$ symmetry to a Z_6 symmetry ($C_3[111] \times Z_2$). In other words, instead of rotation by an arbitrary angle, only rotations of \mathbf{S}_i by $\frac{2\pi}{3}$ around the local $\langle 111 \rangle$ axes leave \mathcal{H}_1 invariant.

In the s-MFT treatment of a system with the Hamiltonian of Eq. (5.1), in a certain region of the parameter space centered around a dominant J_{\pm} (Γ_5 region), the system orders in a state with a $\mathbf{k} = 0$ wave vector and all the magnetic moments in the system lie in the xy plane of their local $[111]$ coordinate system pointing in the same local direction. These spin configurations are referred to as the Γ_5 manifold [111]. As a result, $\mathbf{m}_i \equiv \langle \mathbf{S}_i \rangle^2$ and $\phi_i \equiv \tan^{-1}(m_i^y/m_i^x)$, the azimuthal angle expressed in the local $[111]$ coordinate system, are independent of i the lattice site index. We henceforth drop the lattice site indices of ϕ and \mathbf{m} for these spin configurations. In the Γ_5 region, the s-MFT free-energy of the system is *independent* of ϕ [21]. Consequently, the $U(1)$ degeneracy remains intact at the s-MFT level. However, since \mathcal{H} has a Z_6 symmetry, we expect that in a treatment of the problem that goes beyond s-MFT, the $U(1)$ symmetry will be reduced to a Z_6 symmetry in the paramagnetic phase which gets spontaneously broken in the ordered phase. Below, we present a Ginzburg-Landau (GL) symmetry analysis that allows one to predict the form of the fluctuation corrections to s-MFT that lift this $U(1)$ degeneracy.

5.2.1 Ginzburg-Landau (GL) symmetry analysis

We start by defining the complex variable

$$m_{xy} \equiv \sqrt{m_x^2 + m_y^2} \exp(i\phi), \quad (5.2)$$

which corresponds to the magnitude and direction of the on-site magnetization \mathbf{m} in the local xy plane.

For simplicity, we first consider a strictly local- xy state and assume $m_z = 0$. The allowed terms in the GL free-energy contain only even powers of m_{xy} due to the time reversal symmetry (τ). On the other hand, C_3 , the rotation by $2\pi/3$ about the cubic $\langle 111 \rangle$ axes, forbids the existence of terms of the form $m_{xy}^n + (m_{xy}^*)^n$ unless n is a multiple of

² $\langle \dots \rangle$ represent a thermal Boltzmann average

three. The resulting anisotropy terms in the GL free-energy have the ability to lift the accidental $U(1)$ degeneracy of the Γ_5 manifold since they introduce a dependence of the GL free-energy on the azimuthal angle ϕ , the orientation of the on-site magnetization \mathbf{m} in the local xy plane (see Eq. (5.2)). Considering the effect of C_3 and τ together, the lowest-order symmetry-allowed $U(1)$ degeneracy-lifting term must therefore have $n = 6$. Consequently, for strictly xy order ($m_z = 0$), the sixth order term in the GL free-energy is the lowest order term capable of lifting the degeneracy and has the form

$$m_{xy}^6 + (m_{xy}^*)^6. \quad (5.3)$$

We note that the sixth order term in 3-dimensional XY universality class is dangerously ³ irrelevant which means it does not affect the critical properties of the system.[119] However, this term plays a crucial role in the selection of a specific long-range ordered state at $T \lesssim T_c$.

If we now include the z component of the order parameter, m_z , a $U(1)$ -symmetry breaking term arises at fourth order in the components of \mathbf{m} in the GL free-energy. This effect has been overlooked in Refs. [20, 21, 30, 31]. Again, based on the combined effect of the C_3 and τ symmetry operations, the degeneracy-lifting fourth order term in the GL free-energy has the form

$$m_z[m_{xy}^3 + (m_{xy}^*)^3]. \quad (5.4)$$

Eqs. (5.3, 5.4) together, identify the general form of the first two lowest order terms in the GL free-energy capable of lifting the degeneracy of the Γ_5 manifold.

It turns out that the sixth order term (Eq. (5.3)) and the fourth order term (Eq. (5.4)) have the same net effect in lifting the degeneracy beyond s-MFT as can be shown by combining them into a single term in the GL free-energy. We demonstrate this by considering, at the phenomenological level, the quadratic terms in the GL free-energy $a_0(m_x^2 + m_y^2) + a_1 m_z^2$ where a_0, a_1 are chosen to be different to incorporate the microscopic anisotropic exchange in the Hamiltonian of Eq. (5.1) and to emphasize the possibility of distinct criticality for the xy and z components of the order parameter. Taking into account the degeneracy-lifting terms of Eqs. (5.3, 5.4), we have:

$$\begin{aligned} \mathcal{F}_{\text{GL}} &= a_0(m_x^2 + m_y^2) + a_1 m_z^2 \\ &+ g_0 m_z(m_{xy}^3 + (m_{xy}^*)^3) + g_1(m_{xy}^6 + (m_{xy}^*)^6) \\ &+ \mathcal{F}_{\text{GL}}^{(4)}(m_{xy}, m_z) + \mathcal{F}_{\text{GL}}^{(6)}(m_{xy}, m_z) + \dots, \end{aligned} \quad (5.5)$$

³It is dangerously irrelevant since at temperatures $T < T_c$ this becomes relevant above a length scale λ , which diverges as a power of the correlation length [119].

which, can be rewritten:

$$\begin{aligned}
\mathcal{F}_{\text{GL}} = & a_0(m_x^2 + m_y^2) + a_1(m_z + \frac{g_0|m_{xy}|^3 \cos(3\phi)}{a_1})^2 \\
& - \frac{g_0^2|m_{xy}|^6}{2a_1} + (2g_1 - \frac{g_0^2}{2a_1})|m_{xy}|^6 \cos(6\phi) \\
& + \mathcal{F}_{\text{GL}}^{(4)}(m_{xy}, m_z) + \mathcal{F}_{\text{GL}}^{(6)}(m_{xy}, m_z) + \dots
\end{aligned} \tag{5.6}$$

In Eq. (5.6), $|m_{xy}| \equiv \sqrt{m_x^2 + m_y^2}$. In Eqs. (5.5,5.6), $\mathcal{F}_{\text{GL}}^{(4)}$ and $\mathcal{F}_{\text{GL}}^{(6)}$ are fourth and sixth order isotropic ($U(1)$ invariant) terms that *do not lift* the $U(1)$ degeneracy and \dots represents terms that are of higher order in the components of \mathbf{m} . We point out that Eq. (5.6) is valid when $a_1 > 0$ indicating no criticality for the m_z component. Upon minimizing Eq. (5.6) with respect to m_z , we obtain

$$m_z = -g_0|m_{xy}|^3 \cos(3\phi)/a_1. \tag{5.7}$$

The minimum of \mathcal{F}_{GL} is consequently determined by the term $(2g_1 - g_0^2/2a_1)|m_{xy}|^6 \cos(6\phi)$ with either $\cos(6\phi) = \pm 1$, depending on the sign of $f \equiv 2g_1 - g_0^2/2a_1$. This happens for $\phi = n\pi/3$ with $n = \pm 1, \pm 2, \pm 3$ or $\phi = n\pi/6$ with $n = \pm 1, \pm 3, \pm 5$. These two sets of angles respectively correspond to the ψ_2 and the ψ_3 states (see Fig. 5.1). So, when $f < 0$ ($f > 0$) the minimum free-energy state is ψ_2 (ψ_3). Consequently, *after* minimizing \mathcal{F}_{GL} with respect to m_z ,

$$\delta\mathcal{F}_{\text{GL}} = f|m_{xy}|^6 \cos(6\phi) \tag{5.8}$$

is the $U(1)$ degeneracy-lifting term on which we focus. The boundary between ψ_2 and ψ_3 is thus determined by the real roots of f .

We note that the fluctuation corrections to s-MFT induces a local m_z moment in Eq. (5.7) to the minimum free-energy state which was found to be strictly ordered in the local xy plane at the s-MFT level. Since this moment is proportional to $\cos(3\phi)$, only ψ_2 state can have a finite m_z . This result is also expected based on the symmetries of the ψ_2 and ψ_3 states which we review below.

The symmetries of each ψ_i state ($i = 2, 3$) form a group known as the little group. The generators of the ψ_3 little group include the C_2 rotation by π about one of the cubic x , y or z axes (depending on the particular ψ_3 state), the improper rotation by $\pi/2$ (S_4) about the same cubic axis, and two plane reflections, σ_1 and σ_2 , with respect to planes spanned by the cubic axis and one of the two tetrahedron bonds perpendicular to the cubic axis. The generators of the little group of ψ_2 states include τS_4 , $\tau\sigma_1$ and $\tau\sigma_2$ where τ is the time-reversal symmetry operation. Finite onsite m_z moments on a tetrahedron are only

invariant under the symmetry operations of the ψ_2 's little group. As a result, only the ψ_2 state can possess a finite onsite m_z moment, based on the above symmetry argument. The induced moment, however, is weak just below T_c since it is proportional to $|m_{xy}|^3$.

At the phenomenological GL level, Eq. (5.8) is the final result demonstrating how the $U(1)$ degeneracy of s-MFT level is broken by introducing fluctuation in the free-energy of the system. In this work, however, we are rather interested in understanding how the coefficient of the symmetry-breaking $\cos(6\phi)$ terms in the free-energy of Eq. (5.6), f , can be determined *at the microscopic level* beyond the s-MFT.

5.3 E-TAP method and results

Our goal in Section 5.3 will be to calculate the phase boundary between the ψ_2 and the ψ_3 states determined by the function f in Eq. (5.8), close to $T \lesssim T_c^{\text{MF}}$ using the E-TAP method. In this calculation, for simplicity, we consider $J_{zz} = 0$ in Eq. (5.1)⁴. Since we are predominantly interested in the Γ_5 region where the dominant interaction is J_{\pm} in Eq. (5.1), we express the rest of the couplings in units of J_{\pm} and we henceforth denote the scaled interactions with lower case letters, e.g. $j_{\pm\pm} \equiv J_{\pm\pm}/J_{\pm}$.

5.3.1 Method

In 1977, Thouless, Anderson and Palmer (TAP) [120] proposed a method to study the role of fluctuations in spin glasses. This method is equivalent to calculating the Onsager reaction field (see Chapter 3, Section 3.3). Here, we present an extended version of the TAP method (E-TAP) first developed by Georges and Yedidia [68] for Ising spin-glass which includes fluctuation corrections calculated by TAP and those beyond. To proceed, We must first modify the E-TAP procedure of Ref. [68] to study the case of 3-component Heisenberg spins with anisotropic exchange interactions. In the E-TAP method, nonzero on-site fluctuations i.e. $\langle S_i^\alpha S_i^\beta \rangle \neq \langle S_i^\alpha \rangle \langle S_i^\beta \rangle$, [68] are taken into account via a high-temperature expansion (small β) of the Gibbs free-energy:

$$G = -\frac{1}{\beta} \ln \left(\text{Tr}[\exp(-\beta\mathcal{H} + \sum_i \boldsymbol{\lambda}_i \cdot (\mathbf{S}_i - \mathbf{m}_i))] \right). \quad (5.9)$$

⁴Considering $J_{zz} \neq 0$ contribution to $\cos(6\phi)$ coefficient would require calculating higher order terms in β (seventh and eighth order to include lowest order of J_{zz}) in the expansion of Eq. (5.9) where the number of "relevant" terms proliferates. This calculation is beyond the scope of the present work.

Here, \mathbf{m}_i is the average magnetization at site i , $\mathbf{m}_i \equiv \langle \mathbf{S}_i \rangle$ and $\boldsymbol{\lambda}_i$ is a Lagrange multiplier which fixes \mathbf{m}_i to its mean-field value. The high temperature expansion introduces fluctuations about the s-MFT solution. Defining $\beta G(\beta) \equiv \tilde{G}(\beta)$, the first two terms of the expansion in powers of β , $\tilde{G}(0)/\beta$ and $\tilde{G}'(0)$, are the entropy and energy at the s-MFT level, respectively. The prime represents differentiation with respect to β . The higher order terms in the β expansion of the Gibbs free-energy correspond to fluctuation corrections to the s-MFT free-energy that generate the terms that lift the $U(1)$ degeneracy. We aim to calculate the higher order terms (β^2 and beyond) in the β expansion of Eq. (5.9) that ultimately contribute to the degeneracy lifting term $f|m_{xy}|^6 \cos(6\phi)$ to the lowest order in the coupling constants $j_{\pm\pm}$ and $j_{z\pm}$ ⁵, which is represented by

$$\delta G = f(j_{\pm\pm}, j_{z\pm}) |m_{xy}|^6 \cos(6\phi) \quad (5.10)$$

Here, $f(j_{\pm\pm}, j_{z\pm}) = 0$ determines the phase boundaries between the ψ_2 and the ψ_3 states in the space of coupling-constants $j_{\pm\pm}$ and $j_{z\pm}$. We now proceed to calculate $f(j_{\pm\pm}, j_{z\pm})$.

In the n^{th} order in the β expansion, factors of the form $j_{\pm\pm}^k j_{z\pm}^l$ arise where k and l are positive integers and $k + l = n$. Each power of $j_{\pm\pm}$ and $j_{z\pm}$ contributes factors of $e^{\pm 2i\phi}$ and $e^{\pm i\phi}$, respectively (see Eq. (5.1c)), to the corresponding term in the β expansion. By a simple power counting of these factors, one can easily pinpoint the terms that contribute to $\cos(6\phi)$ (and $\cos(3\phi)$ which is necessary to calculate due to its contribution to g_0 and consequently to f as can be seen in Eq. (5.6)) arising at different orders of β in the E-TAP calculation. It is simple arithmetic to find what combinations of k and l in $j_{\pm\pm}^k j_{z\pm}^l$ generate $\cos(6\phi)$ and $\cos(3\phi)$. We then calculate g_0 and g_1 in Eqs. (5.5, 5.6) in terms of microscopic couplings $j_{\pm\pm}$ and $j_{z\pm}$. Using the E-TAP method, we obtain the $g_0(j_{\pm\pm}, j_{z\pm})$, $g_1(j_{\pm\pm}, j_{z\pm})$ and $f(j_{\pm\pm}, j_{z\pm})$ to the lowest order in $j_{\pm\pm}$ and $j_{z\pm}$ which read as⁶:

$$g_0(j_{\pm\pm}, j_{z\pm}) = a_0 \beta j_{\pm\pm} j_{z\pm} + \beta^2 (a_1 j_{\pm\pm}^2 j_{z\pm} + a_2 j_{z\pm}^3) + \beta^3 (a_3 j_{\pm\pm}^3 j_{z\pm} + a_4 j_{\pm\pm} j_{z\pm}^3) \quad (5.11)$$

and

$$g_1(j_{\pm\pm}, j_{z\pm}) = b_0 \beta^2 j_{\pm\pm}^3 + b_1 \beta^3 j_{\pm\pm}^2 j_{z\pm}^2 + b_2 \beta^4 j_{\pm\pm} j_{z\pm}^4 + b_3 \beta^5 j_{z\pm}^6, \quad (5.12)$$

and in consequence,

$$f(j_{\pm\pm}, j_{z\pm}) = c_0 \beta^2 j_{\pm\pm}^3 + c_1 \beta^3 j_{\pm\pm}^2 j_{z\pm}^2 + c_2 \beta^4 j_{\pm\pm} j_{z\pm}^4 + \beta^5 (c_3 j_{\pm\pm}^4 j_{z\pm}^2 + c_4 j_{\pm\pm}^2 j_{z\pm}^4 + c_5 j_{z\pm}^6). \quad (5.13)$$

⁵We recall that J_{\pm} is the dominant interaction and $j_{\pm\pm}$ and $j_{z\pm}$ are being treated perturbatively in Eq. (5.1).

⁶We also note that E-TAP corrections of the coefficient a_1 does not contribute to $f(j_{\pm\pm}, j_{z\pm})$ when f is calculated to the lowest order of coupling constants $j_{\pm\pm}$ and $j_{z\pm}$.

a_0	a_1	a_2	a_3	a_4
-0.593	-1.13	-0.451	-0.938	7.21

Table 5.1: Values of a_i in $g_0(j_{\pm\pm}, j_{z\pm})$ multiplied by 10^2 .

In Eqs. (5.11, 5.12, 5.13), a_i , $i = 0, \dots, 4$, b_j , $j = 0, \dots, 3$ and c_k , $k = 0, \dots, 5$ are numerical coefficients to be determined by the explicit E-TAP calculation described in Appendix E. Considering the highest power of coupling constants $j_{\pm\pm}$ and $j_{z\pm}$ in Eq. (5.13), one needs to consider the terms up to β^6 in the high-temperature expansion of G .

We remark that obtaining the a_i , b_j and c_k coefficients in Eq. (5.13) involves tremendous amount of effort in calculating the desired terms up to β^6 in the expansion of Eq. (5.9). We presented the necessary tools to perform these calculations in Appendix E.

5.3.2 Results

In order to obtain the numerical value of the a_i , b_j and c_k coefficients in Eq. (5.13), we employ a diagrammatic technique to represent the terms in the β expansion, which constitutes the computational core of the E-TAP method. These diagrams are composed of vertices and bonds [121]. The vertices correspond to lattice sites covered by the diagram and a bond represents the interaction between the vertices that it connects. The details necessary to carry out the calculations using the diagrams are presented in Appendix E. As mentioned earlier, for simplicity, we only consider the case of $j_{zz} = 0$ in this work. After computing the a_i , b_j and c_k coefficients using E-TAP, we find the $f(j_{\pm\pm}, j_{z\pm})$ polynomials to be given by:

$$f(j_{\pm\pm}, j_{z\pm}) = 10^{-1} \times [-0.47\beta^2 j_{\pm\pm}^3 + 4.18\beta^3 j_{\pm\pm}^2 j_{z\pm}^2 + 1.93\beta^4 j_{\pm\pm} j_{z\pm}^4 + 2.03\beta^5 j_{z\pm}^6 - 0.58\beta^5 j_{\pm\pm}^4 j_{z\pm}^2 + 0.33\beta^4 j_{\pm\pm}^3 j_{z\pm}^2 - 4.84\beta^5 j_{\pm\pm}^2 j_{z\pm}^4], \quad (5.14)$$

where we used g_0 and g_1 in Eqs. (5.11, 5.12), respectively, with the numerical values of a_i and b_j coefficients presented in Tables 5.1, 5.2. Since $f(j_{\pm\pm}, j_{z\pm}) = 0$ determines the boundaries between the ψ_2 and the ψ_3 states, we need to compute the roots of Eq. (5.14). We find that Eq. (5.14) has one real root which *to the lowest order in the coupling constants* reads:

$$j_{\pm\pm} = p_0 j_{z\pm}^2 + \dots \quad (5.15)$$

b_0	b_1	b_2	b_3
-0.322	2.92	1.42	1.42

Table 5.2: Values of b_j in $g_1(j_{\pm\pm}, j_{z\pm})$ multiplied by 10^4 .

where the \dots ellipsis represent higher order terms in $j_{z\pm}$ and $p_0 = 9.37\beta$ which determines the phase boundary between the ψ_2 and the ψ_3 states for $j_{zz} = 0$ and $\beta \gtrsim \beta_c$.

The ψ_2/ψ_3 boundary is shown Fig. 5.2-top for $\beta = 0.253 \gtrsim \beta_c^{\text{MF}} = 1/4$. The boundaries of the overall Γ_5 region for $j_{zz} = 0$ is also shown in this figure. In Ref.[31] it is found that at zero-temperature, quantum fluctuations yield three distinct phase boundaries for $j_{zz} = 0$ (see Fig. 5.2-Bottom). Combining our results with the ones from Ref. [31], suggests the possibility of multiple transitions between ψ_2 and ψ_3 as the temperature is decreased well below T_c (see Ref. [34] where such a phenomenon is observed). Such a scenario constitutes an exotic variant of the ObD phenomenon, since fluctuations select distinct long-range ordered states in different temperatures regimes ($T \lesssim T_c$ and $T = 0^+$).

5.4 Discussion

In this chapter, we used an extended TAP (E-TAP) method to analytically study the problem of ObD near the critical temperature, in a system of 3D XY spins on the pyrochlore lattice with the Hamiltonian in Eq. (5.1) considering $J_{zz} = 0$. We focused on the Γ_5 manifold which is $U(1)$ degenerate at the standard mean field theory (s-MFT) level. The fluctuations in the free-energy beyond s-MFT were organized in an expansion in powers of β , to the lowest order in coupling constants $J_{\pm\pm}$, $J_{z\pm}$ and magnetization \mathbf{m} . These fluctuations introduce a hexagonal anisotropy to the free energy of the system which select either the ψ_2 or the ψ_3 as the only minima of the free-energy of the system in different parts of the Γ_5 region. The phase boundary between ψ_2 and ψ_3 states can be obtained by finding the real roots of a cubic equation in terms of $J_{\pm\pm}/J_{\pm}$ and $J_{z\pm}/J_{\pm}$ (see Eq. (??)). We also note that the fluctuation induced anisotropy in the free-energy can in general have the form of $v(\phi) = \sum_{n>0} f_n \cos[6(2n+1)\phi]$ (only odd multiples of six can distinguish between ψ_2 and ψ_3 states). The higher order anisotropy term, however, do not lead to qualitative new behaviour in the phase boundaries between ψ_2 and ψ_3 [31].

Using E-TAP, we found that for a state strictly ordered in the local xy plane *at the s-MFT level*, fluctuations can induce an out-of- xy -plane component to the on-site magnetization. This fluctuation-induced local z component of the magnetization is only compatible

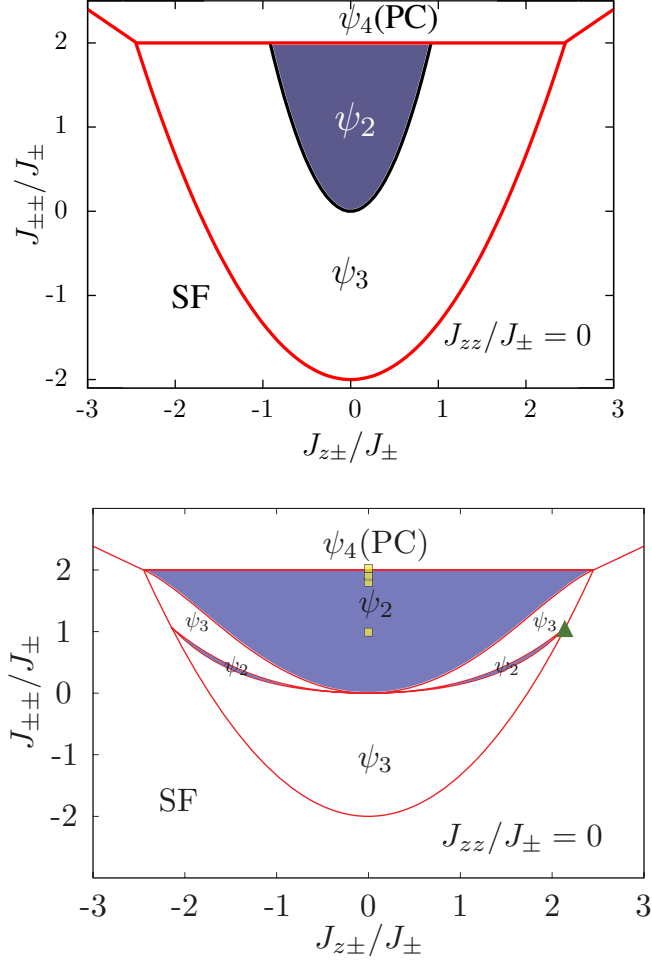


Figure 5.2: **Top:** The figure is made by of Alexander G. R. Day. The $j_{zz} = 0$ phase diagram of the model at $T \lesssim T_c$. The Γ_5 region corresponds to the region enclosing the ψ_2 and ψ_3 states taken together. The Γ_5 region is circumscribed by an outer (red) parabola $j_{\pm\pm} = 2j_{z\pm}^2/3 - 2$ and a horizontal red line at $j_{\pm\pm} = 2$ obtained from the s-MFT calculation [31]. The phase boundary between the ψ_2/ψ_3 states obtained from the E-TAP calculation is represented by the black line. The phases outside of the boundaries of Γ_5 region are: SF, a splayed ferromagnet canted from [100] cubic direction and the so called ψ_4 or Palmer-Chalker state. [31]. **Bottom:** Reproduced from Ref. [31]. $T = 0^+$ phase diagram obtained by spin-wave theory. The boundaries between ψ_2 and ψ_3 states are clearly different from the top phase diagram, indicating the possibility of multiple phase transitions between ψ_2 and ψ_3 states as the temperature decreased.

with the ψ_2 state. We expect the size of this moment to be small, since it is proportional to $|m_{xy}|^3 \ll 1$ for $T \lesssim T_c^{\text{MF}}$.

Considering the phase boundaries between ψ_2 and ψ_3 states obtained by E-TAP at $T \lesssim T_c$ along with the ones from Ref. [31], where multiple phase boundaries between ψ_2 and ψ_3 states at $T = 0^+$ are found for $J_{zz} = 0$ (see Fig. 5.2-Bottom), we may expect to find multiple phase transitions between ψ_2 and ψ_3 states in the Γ_5 region upon decreasing temperature from $T \lesssim T_c$ to $T \sim 0^+$. This indicates that the free-energy landscape of the system described by Eq. (5.1), in the Γ_5 region, can change with temperature as a consequence of change of the density of available states around the free-energy local minima. As a result, the global minima of the free-energy may be different at different temperatures. Since the E-TAP phase boundary is obtained to the lowest order in $j_{\pm\pm}$ and $j_{z\pm}$, it would need to be modified by calculating higher order terms in these couplings, close to the phase boundaries of the Γ_5 region. Consequently, the E-TAP phase boundary in Eq. (5.15) is valid for small $j_{\pm\pm}$ and $j_{z\pm}$.

The E-TAP corrections to the s-MFT free-energy could be computed for the $J_{zz} \neq 0$ case. This could constitute the topic of a future study.

In the next Chapter, we focus more directly on a material aspect of ObD at $T = T_c^-$. Recalling the importance of the long range dipolar interaction in rare-earth pyrochlore oxides from Chapter 2, we investigate the ObD selection at $T = T_c^-$ by performing Monte Carlo simulations using a Hamiltonian that includes Eq. (5.1) with its coupling constants tuned to those of $\text{Er}_2\text{Ti}_2\text{O}_7$'s experimentally obtained in Ref. [21], as well as the long range dipolar interaction.

Chapter 6

Thermal ObD in $\text{Er}_2\text{Ti}_2\text{O}_7$

In Chapter 5, we saw that in a certain region of the parameter space of mg-Hamiltonian, known as Γ_5 region, a $U(1)$ symmetry emerges at s-MFT level in the ordered phase. We showed that fluctuations beyond s-MFT break this accidental symmetry and reduce it to a Z_6 symmetry. In order to relate our investigations in Chapter 5 to experiments and in an effort to study the effect of long-range dipolar interaction on ObD selection at $T = T_c^-$ in the Γ_5 region, we explore the critical properties of a system represented by a Hamiltonian including long-range magnetostatic dipole-dipole interactions and Eq. (5.1) with its coupling constants tuned to those of $\text{Er}_2\text{Ti}_2\text{O}_7$'s which are known to be in Γ_5 region [20, 21]. We find that the critical behaviour of this model is consistent with 3D XY universality class. Focusing on the effect of long-range dipolar interaction, we find that the transition temperature of this model is slightly increased in comparison with that of the nearest-neighbour model. However the spin configuration of the long-range ordered state remains the same as the nearest-neighbour model's, the ψ_2 state.

6.1 Introduction

In an attempt to demonstrate a definitive order-by-disorder (ObD) in real materials, which has been proven to be exceedingly difficult, two different theoretical studies have over the last year converged more or less simultaneously [20, 21] to argue that a *quantum* variant of ObD is at work in $\text{Er}_2\text{Ti}_2\text{O}_7$. The main interest in these two recent studies stems from the fact that the proposed quantum ObD (q -ObD) leads to the selection of a *unique* ground

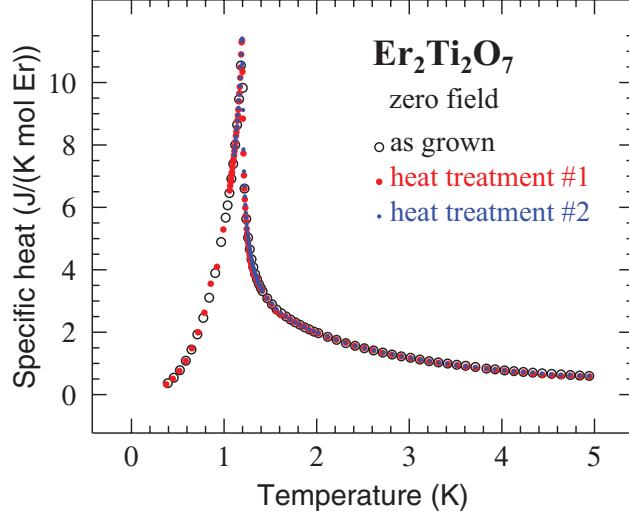


Figure 6.1: Reproduced from Ref. [115]. Zero field specific heat of $\text{Er}_2\text{Ti}_2\text{O}_7$ versus temperature measured for three samples. All of them show a second order phase transition at $T_c \approx 1.2$ K.

state (so-called ψ_2 state a basis state of the Γ_5 manifold¹, as opposed to ψ_3 state; the second basis state of the Γ_5 manifold) out of the set of accidentally degenerate classic ground states and which further corresponds to the long range ordered state observed in $\text{Er}_2\text{Ti}_2\text{O}_7$ below a critical temperature $T_c \approx 1.2$ K [111, 112, 122] (see Fig. 6.1)².

The specific mechanism leading to the observed long-range ordered state in $\text{Er}_2\text{Ti}_2\text{O}_7$ had defied explanation [30, 42] since its original observation [111, 112] and the studies reported in Refs. [20, 21] are not only of importance for the understanding of XY pyrochlore magnets, but are also important contributions to the field of frustrated magnetism as a whole.

A corollary of this q -ObD proposal and thus of the spin models considered [20, 21], in particular the model of Ref. [21], is that the experimentally observed second order phase

¹ Manifold of spin configurations on the pyrochlore lattice with a $\mathbf{k} = 0$ wave vector and all the magnetic moments in the system lie in the xy plane of their local [111] coordinate system and point in the same local direction.

² Specific heat measurements of $\text{Er}_2\text{Ti}_2\text{O}_7$ indicated a phase transition at $T_c \approx 1.2$ K and neutron scattering experiments found an ordering wave vector of $\mathbf{k} = 0$ for this compound where the scattered intensity I vanishes at T_c as $I(T) \propto (T_c - T)^{2\beta}$ with $\beta \approx 0.33$, indicating a continuous phase transition to the ψ_2 state [111, 112].

transition in the three-dimensional (3D) $U(1)/XY$ universality class in $\text{Er}_2\text{Ti}_2\text{O}_7$ at T_C has been, at last, rationalized. It was then shown by Ref. [32] through a high temperature expansion method, that in a system with model Hamiltonian of Ref. [21], at $T = T_c^-$, an ObD mechanism is at play in the selection of the long-range ordered state which is demonstrated to be the ψ_2 state.

On the other hand, while the work of Ref. [20] does find compelling evidence for such universality for the strongly anisotropic limit of the toy model they consider, their model does not incorporate all the symmetry-allowed anisotropic interactions that Ref. [21] considers.

Perhaps the most important missing piece of puzzle in all of the above investigations, is the significantly strong long-range dipolar interactions present in $\text{Er}_2\text{Ti}_2\text{O}_7$. The effect of this strong interaction on the ObD selection at $T = T_c^-$ had not been investigated prior to the work that will be presented in this chapter.

In what follows, to continue our path in investigating the ObD mechanism in the $T = T_c^-$ regime, we establish via Monte Carlo (MC) simulations that a version of Savary *et al.*'s model [21], which neglects its quantum aspect at T_c , does indeed display a transition at $T_c^{\text{MC}} \approx T_c$ to the experimentally observed ground state, *even* when the model is amended to incorporate the non-negligible long-range dipole-dipole interactions.

6.2 Model and method

In $\text{Er}_2\text{Ti}_2\text{O}_7$, the magnetic moment of Er^{3+} ions have total angular momentum of $J = 15/2$ and Ti^{4+} ions are nonmagnetic. Each of the Er^{3+} ions is surrounded by an oxygen-cage (eight oxygen ions). These oxygen ions create a crystal electric field (CEF) that admixes the angular momentum eigenstates, $|J, m_J\rangle$. Since Er^{3+} ion is a Kramers ion, the CEF Hamiltonian has a doublet as its ground state that is separated from the excited states by an energy gap that is three order of magnitude stronger than the energy scale of the interactions between the Er^{3+} ions in $\text{Er}_2\text{Ti}_2\text{O}_7$ [11]. As a result, Er^{3+} ions can be described by an effective spin-1/2 model and a g tensor, defined in Section 2.1 in Chapter 2, that takes into account the single ion anisotropy associated with the CEF ground state. The Hamiltonian for $\text{Er}_2\text{Ti}_2\text{O}_7$ is the same one as in Eq. (5.1). The coupling constants are taken as the ones obtained in Ref.[21] by fitting the dispersion relation calculated by linear spin-wave approximation, to the one measured in neutron scattering experiment in a polarized

paramagnetic state in a strong magnetic field. The mg-Hamiltonian is given by:

$$\begin{aligned} \mathcal{H}_{\text{nm}} = & \sum_{\langle i,j \rangle} \{ J_{zz} S_i^z S_j^z - J_{\pm} (S_i^+ S_j^- + S_i^- S_j^+) \\ & + J_{\pm\pm} (\gamma_{ij} S_i^+ S_j^+ + \gamma_{ij}^* S_i^- S_j^-) \\ & + J_{z\pm} [S_i^z (\zeta_{ij} S_j^+ + \zeta_{ij}^* S_j^-) + i \leftrightarrow j] \} \end{aligned} \quad (6.1)$$

where S_i^μ are pseudo-spin-1/2 components in local $\langle 111 \rangle$ coordinate system attached to each basis site in the pyrochlore lattice. ζ_{ij} and γ_{ij} are phases that depend on the bonds in pyrochlore lattice[44]. Based on our discussion in Section 2.1 of Chapter 2, $S_i^\mu = (1/2g_J) \sum_\nu g^{\mu\nu} \sigma_i^\mu$ where σ_i^μ with $\mu = +, -, z$ are the Pauli matrices. Since S_i^μ are expressed in local coordinate system in Eq. (6.1), the g tensor is diagonal and Eq. (6.1) can be considered in the following way: redefining $S_i^\mu \equiv (1/2g_J) \sigma_i^\mu$ and the g tensor matrix elements can be absorbed in the coupling constant as $J_{ij}^{\mu\nu} \rightarrow J_{ij}^{\mu\nu} g^{\mu\mu} g^{\nu\nu}$. In the rest of this chapter, we choose this convention.

The couplings extracted from the experiment in Ref.[21], in units of 10^{-2} meV, are

$$\begin{aligned} J_{\pm} &= 6.5 \pm 0.75, & J_{\pm\pm} &= 4.2 \pm 0.5, \\ J_{zz} &= -2.5 \pm 1.8, & J_{z\pm} &= -0.88 \pm 1.5. \end{aligned} \quad (6.2)$$

The g tensor for $\text{Er}_2\text{Ti}_2\text{O}_7$ has the form of $g_{xx} = g_{yy} = g_{\perp}$ and $g_{zz} = g_{\parallel}$ in local $\langle 111 \rangle$ coordinate systems with $g_{\perp} = 5.97 \pm 0.08$ and $g_{\parallel} = 2.45 \pm 0.23$ which are included in the values of the couplings in Eq. (6.2) as described in the above convention. The Landé for Er^{3+} ions is $g_J = 6/5$ [32].

Due to the large magnetic moment of Er^{3+} ions, long-range magnetostatic dipole-dipole interaction is significant in $\text{Er}_2\text{Ti}_2\text{O}_7$. The dipolar Hamiltonian for pseudo-spin-1/2 moments in global coordinates reads:

$$\mathcal{H}_{\text{dip}} = D \sum'_{i>j} \frac{g_i^{\omega\alpha} S_i^\omega g_j^{\gamma\beta} S_j^\gamma}{r_{ij}^3} \left(\delta_{\alpha\beta} - 3\hat{r}_{ij}^\alpha \hat{r}_{ij}^\beta \right) \quad (6.3)$$

where $D = \mu_0 \mu_B^2 / 4\pi a^3 = 0.525 \times 10^{-4} \text{meV}$ and $a = 10.1 \text{\AA}$ is the edge of the conventional cubic unit cell in $\text{Er}_2\text{Ti}_2\text{O}_7$. r_{ij} is expressed in units of a . In Eq. (6.3), for simplicity, S_i^ω are expressed in the global coordinate system and $g_i^{\omega\alpha}$ are the elements of g tensor in global coordinates. Here, the summation convention for repeated Greek superscripts is implied. \sum' indicates that we are *excluding* nearest-neighbour dipole-dipole interaction since the

nearest-neighbour part of the long range dipolar interaction is already implicitly included in Eq.(6.2) [21]. So the full Hamiltonian considered in this chapter, is given by :

$$\mathcal{H} = \mathcal{H}_{\text{nn}} + \mathcal{H}_{\text{dip}}. \quad (6.4)$$

At the standard mean field theory (s-MFT) level and as discussed in Chapter 5, the ordered phase of the model of Eq. (6.1) has the spin configuration that belongs to the so-called Γ_5 manifold with $\mathbf{k} = 0$ ordering wave vector. All the spins lie in the xy plane of the local $\langle 111 \rangle$ coordinate systems pointing in the same local direction and the s-MFT free-energy is independent of the local azimuthal angle [21]. Consequently, at the s-MFT level, the system possesses an accidental $U(1)$ degeneracy. Beyond s-MFT, thermal [32] and quantum fluctuations [21, 31] break the continuous $U(1)$ symmetry and reduce it to a discrete Z_6 symmetry which in turn breaks in the ordered phase and the ψ_2 state as opposed to ψ_3 state, is selected [21] (see Fig. 5.1 and Appendix Eq. (D.1) for details regarding ψ_2 and ψ_3 states). The theoretical results are in agreement with experiments [111, 112, 113, 114, 115]. To confirm the thermal selection of ψ_2 and to study the effect of the long-range tail of the magnetostatic dipole-dipole interaction, we explore the critical behaviour of the system with the model Hamiltonian of Eq. (6.4) close to this transition and the spin configuration of its ordered phase, using classical Monte Carlo (MC) simulations. We performed the MC simulations for classical three-component spins with unit length³ on the pyrochlore lattice using parallel tempering technique [63] for better equilibration. Simulations were performed for seven system sizes $L = 2, \dots, 8$. To account for the long-range dipolar interaction, we employed the Ewald summation method [56]. For each temperature point, about 10^8 spin flips per spin were attempted with an average acceptance of approximately 50%⁴. We now proceed to present the results.

6.3 Critical behaviour

The order parameter corresponding to XY -like ordering in the Γ_5 manifold is defined as follows:

$$\zeta = \sqrt{\sum_{i=1}^3 p_a^2} \quad (6.5)$$

³Ignoring quantum effects at $T = T_c^-$ regime and normalizing the spin length.

⁴In parallel tempering process, a replica swap attempted after about 10^3 spin flip attempts

with

$$p_a = \frac{1}{N} \sum_{i=1}^N \mathbf{S}_i \cdot \hat{e}_i^a \quad (6.6)$$

where $\{\mathbf{S}_i\}$ is the spin configuration obtained in the Monte Carlo simulations and \hat{e}_i^a specifies the direction of the spin at site i in one of the three distinct ψ_3 states which are not related by time reversal symmetry (see Appendix D). We note that considering the other basis state of Γ_5 , ψ_2 state, instead of ψ_3 state in defining the order parameter in Eq. (6.5), would lead to the same value for ζ , since ζ is invariant under rotations about local $\langle 111 \rangle$ by $\pi/6$ which transforms ψ_3 to ψ_2 . The growth of this order parameter signals that the system orders in the local xy planes with either a ψ_2 or ψ_3 ordering pattern within the Γ_5 manifold. To identify the ordering pattern, an order parameter sensitive to the azimuthal angle in the local xy plane needs to be defined, a matter that we focus on in Section 6.4. We also measured the order parameter susceptibility (χ) and the order parameter Binder cumulant (B_4), which are defined, respectively, as:

$$\chi = \frac{1}{T} (\langle \zeta^2 \rangle - \langle \zeta \rangle^2) \quad (6.7)$$

$$B_4 = 1 - \frac{\langle \zeta^4 \rangle}{3 \langle \zeta^2 \rangle^2}. \quad (6.8)$$

Here $\langle \dots \rangle$ represents a Monte Carlo average. The results for $\langle \zeta \rangle$, χ and B_4 are presented in Fig. 6.2, left column. We observe a clear continuous phase transition from the paramagnetic phase to the ordered phase which manifests itself through a continuous increase of ζ and a susceptibility whose amplitude at its peak grows with increasing the system size. The crossings of B_4 for different system sizes indicates $\frac{T_c}{J_{\pm}} \simeq 2.8$. We recall that our simulations were performed for classical 3-component spins with unit length. In order to obtain the T_c in units of Kelvin, we use the relation $T_c \approx 2.8 S^2 J_{\pm} = 0.53$ K. Here, $S^2 = |\mathbf{S}|^2 = 1/4$ which were factored out during the simulations for simplicity and need to be considered since the Hamiltonian in Eq. (6.1) describes an effective pseudo-spin-1/2 model. The finite size scaling plots for ζ , χ and B_4 are shown in Fig. 6.2, right column. The order parameter scales according to the following function:

$$\zeta = L^{-\beta/\nu} f(L^{1/\nu}(T - T_c)), \quad (6.9)$$

and the susceptibility scaling function is:

$$\chi = L^{\gamma/\nu} g(L^{1/\nu}(T - T_c)). \quad (6.10)$$

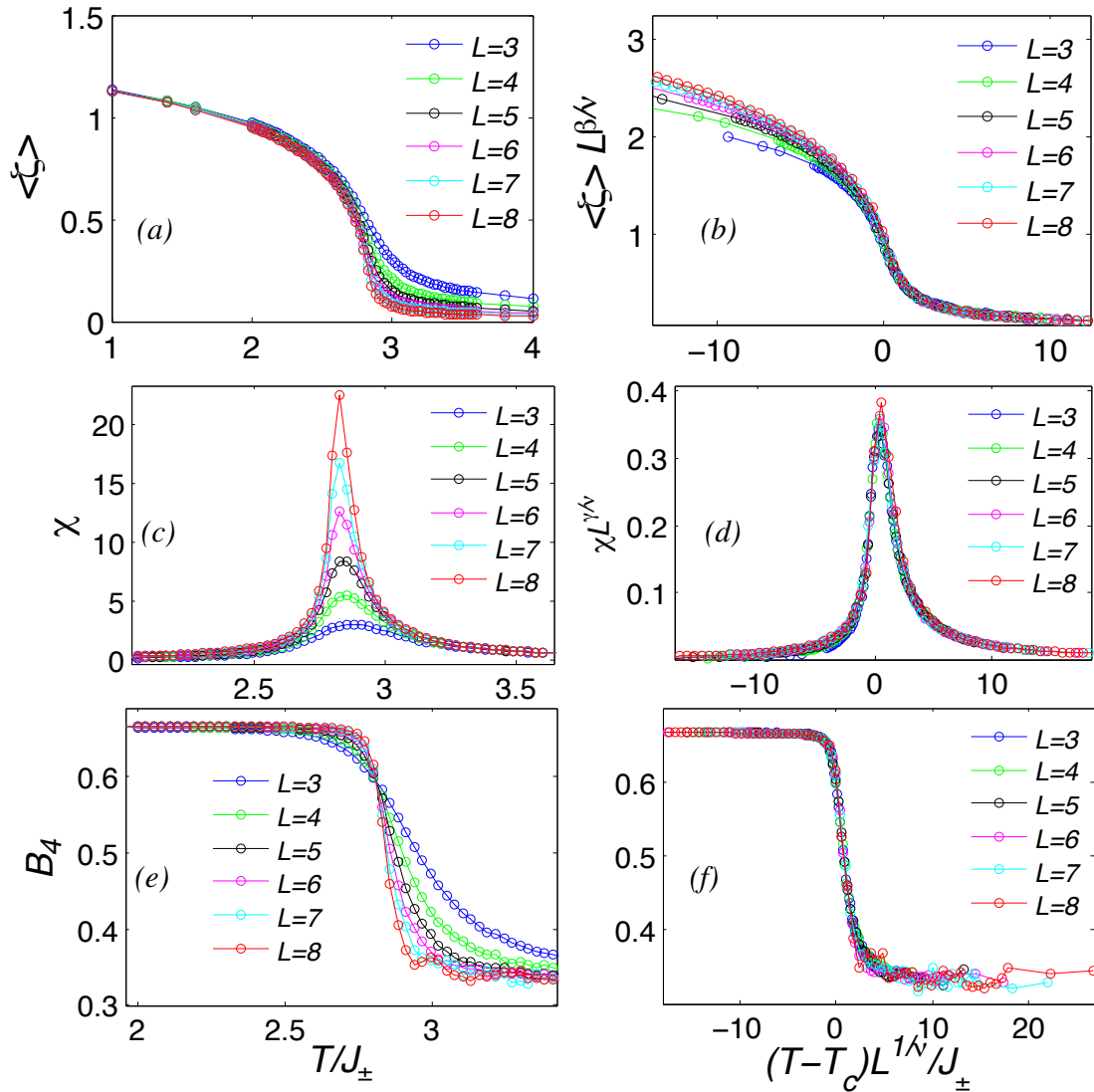


Figure 6.2: (a) Order Parameter ζ (b) Scaling analysis of order parameter, $\beta = 0.346$ and $\nu = 0.669$ with the scaling function of Eq. (6.9) (c) Susceptibility χ (d) Scaling analysis of χ with $\nu = 0.669$ and $\gamma = 1.316$ (e) Binder cumulant B_4 (f) B_4 scaling analysis with $\nu = 0.669$. The values of critical exponents are imposed; not fitted. The error bars in all of the above plots are about the same size as the data symbols.

The values of the critical exponents $\beta = 0.35$, $\nu = 0.67$ and $\gamma = 1.32$ for 3D XY universality class [64], were imposed and led to a reasonable collapse at critical region i.e. $|T - T_c|/J_{\pm} \approx 5$. These results show that the order parameter ζ possesses the symmetry of 3D XY model when the long range dipolar interaction is considered, which is not surprising considering the symmetries of the Hamiltonian in Eq. (6.4). Recalling the Z_6 anisotropy present in Eq. (6.1), we note that this anisotropy is shown to be dangerously irrelevant i.e. it does not influence the critical behaviour of the system but plays a key role in the selection of a specific long-range ordered state [119]⁵. As a result, the critical properties of ζ falls under the universality class of 3D XY model.

We also measured the specific heat in our MC simulation. $C(T)$ is defined as

$$C(T) = \frac{1}{NT^2} (\langle \mathcal{H}^2 \rangle - \langle \mathcal{H} \rangle^2). \quad (6.11)$$

Fig. 6.3-left shows the result of this measurement for different system sizes. Since C_v has a nonzero regular part, the finite-size scaling of specific heat is somewhat difficult. Fig. 6.3-right shows the $C^{\max}(T)$ as a function of system size that is scaled as $L^{\alpha/\nu}$ with the scaling form [34] of

$$C^{\max}(T) = C_0 + C_1 \times L^{\alpha/\nu}. \quad (6.12)$$

The imposed value of α is -0.007 , the one expected for 3D XY universality class [64]. The linear fit indicates reasonable agreement between the critical behaviour of the specific heat of the model for $\text{Er}_2\text{Ti}_2\text{O}_7$ and that of the 3D- XY universality class [64].

Based on the scaling behaviour of the model Hamiltonian of Eq. (6.4) proposed for $\text{Er}_2\text{Ti}_2\text{O}_7$ in our Monte Carlo studies, we may conclude that this model goes through a phase transition which can be classified under 3D XY universality class.

6.4 Selection of ψ_2 state

In this section, we investigate the type of long-range ordered state selected at $T \lesssim T_c$ for the model Hamiltonian of Eq. (6.4) and compare this result with the result of the selection for the nearest-neighbour-only model Hamiltonian of Eq. (6.1). Fig. 6.4a shows the result of measuring $\langle \zeta \rangle$ in the MC simulation for Hamiltonians in Eq. (6.4) (black) and Eq. (6.1) (green). The results indicate that the presence of the dipolar interaction increases the transition temperature by about 3%.

⁵It is dangerously irrelevant since at temperatures $T < T_c$ this becomes relevant above a length scale Λ , which diverges as a power of the correlation length [119]

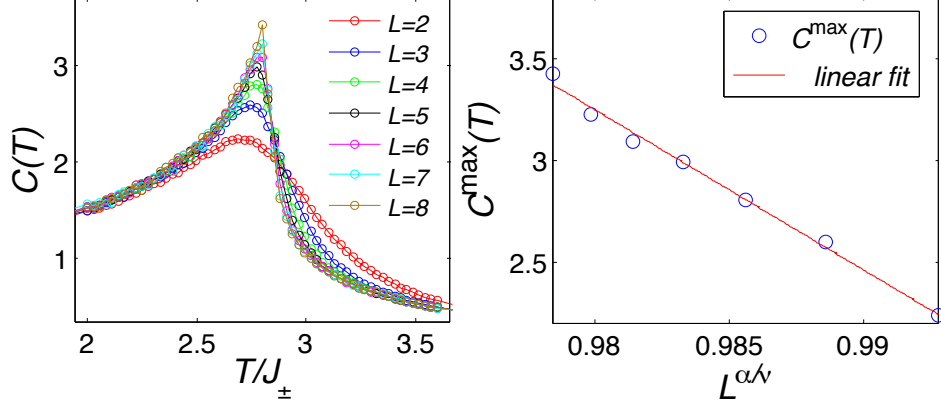


Figure 6.3: *Left*: Specific heat for different system sizes *Right*: Scaling analysis using Eq. (6.12) with $\alpha \equiv -0.007$ (imposed; not fitted). The error bars in the above plots are about the same size as the data symbols.

In order to identify the spin configuration of the ordered state, one needs to distinguish between ψ_2 and ψ_3 states. The order parameter ζ is not capable of doing so. In consequence, we need to define another order parameter sensitive to the local azimuthal angle. The following order parameter possesses this property and is given by [34]:

$$\zeta_6 = \zeta \cos(6\phi). \quad (6.13)$$

Here

$$\phi = \tan^{-1} \left(\frac{\sqrt{3}(p_1 - p_2)}{p_1 + p_2 - 2p_3} \right) \quad (6.14)$$

is the local azimuthal angle, while p_a with $a = 0, 1, 2$ are defined in Eq. (6.6), $(p_1 + p_2 - 2p_3)/\sqrt{6}$ and $(p_1 - p_2)/\sqrt{2}$ are the local x and y components of the ζ order parameter, respectively. Considering that ψ_3 is used in Eqs. (6.5, 6.6) i.e. ζ and ζ_6 are defined with respect to the ψ_3 state, having $\phi = n\pi/6$ with $n = 0, \pm 2, \pm 4, 6$ corresponds to the ψ_3 states while $n = \pm 1, \pm 3, \pm 5$ correspond to the ψ_2 states. Hence, $\zeta_6 < 0$ and $\zeta_6 > 0$ indicate that the system orders in a ψ_2 or a ψ_3 state, respectively. Figs. 6.4b and 6.4c show $\langle \zeta_6 \rangle$ result from the MC simulations including and excluding long range dipolar interaction, respectively. At $T < T_c$, the system enters a ψ_2 state where $\zeta_6 < 0$, with the $|\zeta_6|$ increasing as the system size, L , is increased. The results in Fig. 6.4 show that the presence of the long-range dipolar interaction does not affect the selection, although it changes slightly (3%) the critical temperature T_c .

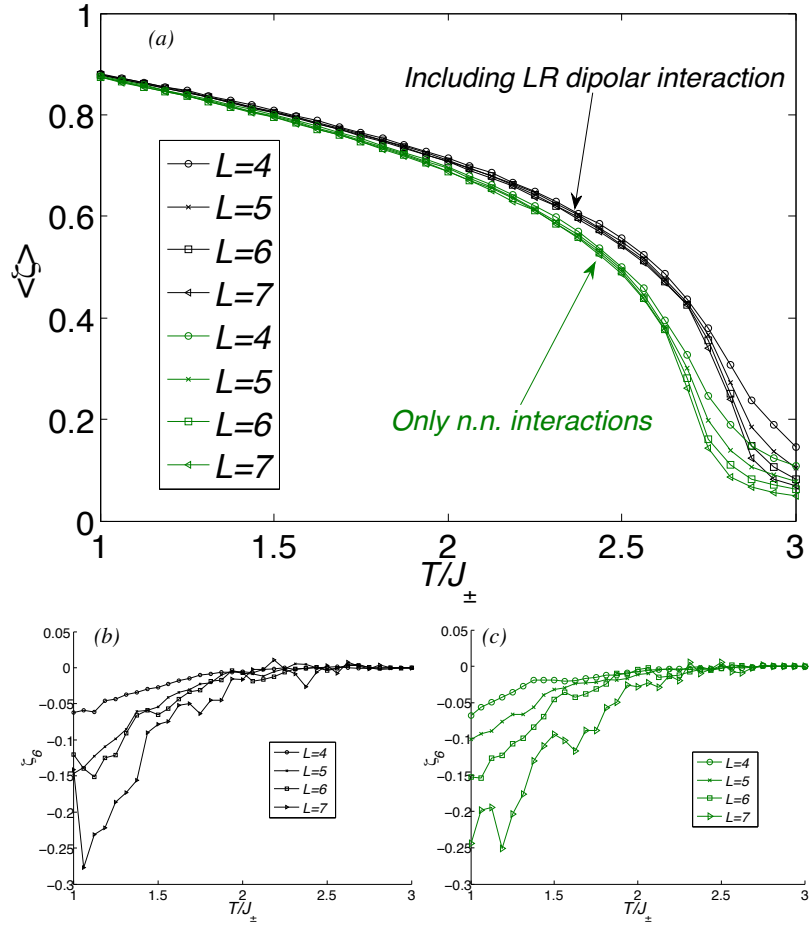


Figure 6.4: (a) The order parameter for simulation with \mathcal{H}_0 (green) from Eq. (6.1) and \mathcal{H} (black) from Eq. (6.4). (b) $\langle \zeta_6 \rangle$ including long-range dipolar interaction (c) $\langle \zeta_6 \rangle$ without long-range dipolar interaction.

6.5 Conclusion

We investigated the effect of the long-range magnetostatic dipole-dipole interaction on the critical behaviour and on the classical selection of the long-range ordered state of a bilinear spin Hamiltonian appropriate for the rare-earth pyrochlore oxide $\text{Er}_2\text{Ti}_2\text{O}_7$. We considered the Hamiltonian in Eq. (6.4), which includes the mg-Hamiltonian of Eq. (6.1) as well as the long-range dipolar interaction. We used the coupling constants obtained from the experiment in Ref. [21]. Our study shows that the critical behaviour of this model is consistent with that of the 3D XY universality class which is also consistent with experimental results.

Our simulations shows that the addition of the long-range tail of the dipolar interaction to the Hamiltonian of the Eq. (6.1) does not change the ObD selection of the long-range state i.e. the pattern of the ordered state remains ψ_2 . The presence of the long-range dipolar interaction very marginally affect the transition temperature (by about 3% in comparison with the nearest-neighbour model's T_c). This had been implicit in Refs. [20, 21] but had remained unchecked. It appears that the increase of T_c indicates the suppression of the fluctuations due to the long-range dipolar interaction. However, the energy change of the ground state, the ψ_2 , due to long range dipolar interaction needs to be assessed, in order to make a meaningful comment on this matter. In addition, Oitmaa *et al.* in Ref. [32] suggested that the thermodynamic properties of a system described by Eq. (6.1) were indeed not significantly affected at T_c by the dipolar interactions. We also note that the long range dipolar interaction renormalizes the spin-wave gap, a signature of discrete symmetry, at $T = 0^+$. However it does not influence the selection for spin-spin coupling appropriate for $\text{Er}_2\text{Ti}_2\text{O}_7$ [31].

Although recent investigations [20, 21, 31] support the scenario in which the ObD is responsible for the selection of the ground state of $\text{Er}_2\text{Ti}_2\text{O}_7$, it has been pointed out by McClarty *et al.* that ψ_2 state can be energetically selected through van Vleck-like mechanisms. They demonstrated that an anisotropy can be generated through perturbative inclusion of excited doublet in the low energy Hamiltonian, in powers of J/Δ where J is nearest-neighbour exchange and Δ is the energy gap between CEF ground doublet and first excited doublet [42]. Ref. [21] argues that this mechanism is not strong enough to be at play in $\text{Er}_2\text{Ti}_2\text{O}_7$. However, this remains to be explicitly determined both theoretically and experimentally.

In the next Chapter, we change gear from pyrochlore systems and consider a system of point dipoles on the FCC lattice. We show that, at the s-MFT level, an $O(3)$ symmetry emerges in this system and thermal and quantum fluctuations at $T = 0^+$ and $T = T_c^-$, respectively, select a [111] polarized state by breaking this symmetry.

Chapter 7

Emergent $O(3)$ symmetry breaking due to fluctuations in a system of point dipoles on FCC lattice

In this chapter, we study the order-by-disorder (ObD) phenomenon in a system of classical 3-component Heisenberg spins on the FCC lattice interacting via long-range magnetostatic dipole-dipole interaction. At the standard mean-field theory level, the system shows an emergent $O(3)$ symmetry. This symmetry breaks upon considering the fluctuation effects. It had been suggested via the results of Monte Carlo simulations [123] that the ObD selected state at $T \lesssim T_c$ regime is different from the the ObD selected state at $T = 0^+$. We investigate the ObD selection in this model at different temperature regimes using the E-TAP method, spin-wave theory and Monte Carlo simulations. We find that the ObD selection is the same in these two temperature regimes, contradicting a previous claim [123].

7.1 Introduction

In this chapter, we study one of the simplest Hamiltonians that shows the ObD phenomenon: classical Heisenberg spins on the FCC lattice interacting via magnetostatic long-range dipole-dipole interaction. The possibility of ordering in cubic dipolar systems has been discussed from variety of viewpoints [124]. It was demonstrated by several groups [36] that a system of point dipoles on FCC lattice enters a ferromagnetic phase at temperatures comparable to the dipolar energy scale. The candidate materials for these toy

models, FCC rare-earth salts, are observed to support this prediction. Further theoretical investigations [123] on FCC dipolar system shows the selection of the long-range ordered state along [111] cubic direction, is the result of thermally induced anisotropy and furthermore suggest that another transition at low temperature occurs in this system, that changes the direction of the magnetization from [111] to [100] as the temperature decreases (see Fig. 7.1). On the other hand, the spin wave theory study by Cohen and Keffer [124] suggest that the ground state of the system is polarized along the [111] direction.

By employing variety of methods, we reinvestigated the results presented by Ref. [123]. Our studies show that a system of dipolar spins on the FCC lattice enters and *remains* in a ferromagnetic state polarized in the [111] direction down to the lowest temperature. In what follows, in Section 7.2, we first present the result of our s-MFT study indicating the emergence of $O(3)$ symmetry. In Section 7.3, we show that considering fluctuations beyond s-MFT treatment selects a ferromagnetic state along [111] at all temperature regimes by generating a cubic anisotropy in a 3-vector model. In Section 7.3.1, we show that zero point fluctuations select [111] polarized state out of the $O(3)$ -degenerate manifold of states. In Section 7.3.2, we investigate the ObD selection at $T = T_c^-$. We show that the cubic anisotropy generated by fluctuations at this temperature regime also selects [111] polarized state. To confirm our findings from the spin wave theory at $T = 0^+$ and the E-TAP at $T = T_c^-$ as well as investigating the intermediate temperatures, i.e. $0 < T < T_c$, we performed Monte Carlo simulations. The results are presented in Section 7.3.3 and indicate that [111] polarized state is selected by ObD mechanism at all temperatures below T_c .

7.2 s-MFT and GL analysis

We considered the following Hamiltonian for dipolar spins on the FCC lattice:

$$\mathcal{H}^{\text{FCC}} = \mathcal{J}_{\text{dip}} \sum_{i,j} \frac{\mathbf{S}_i \cdot \mathbf{S}_j}{r_{ij}^3} - \frac{3(\mathbf{S}_i \cdot \mathbf{r}_{ij})(\mathbf{S}_j \cdot \mathbf{r}_{ij})}{r_{ij}^5}. \quad (7.1)$$

where \mathbf{r}_{ij} is the position vector connecting sites i and j in the FCC lattice and we consider $\mathcal{J}_{\text{dip}} = 1$. By employing the Ewald summation technique to account for the long-range dipolar interaction, we solved the s-MFT self-consistent equation

$$m_i = -\frac{\mathbf{h}_i}{|\mathbf{h}_i|} \left[\coth(\beta|\mathbf{h}_i|) - \frac{1}{\beta|\mathbf{h}_i|} \right] \quad (7.2)$$

where

$$h_i^\mu = \sum_{j,\nu} \mathcal{J}_{ij}^{\mu\nu} m_j^\nu. \quad (7.3)$$

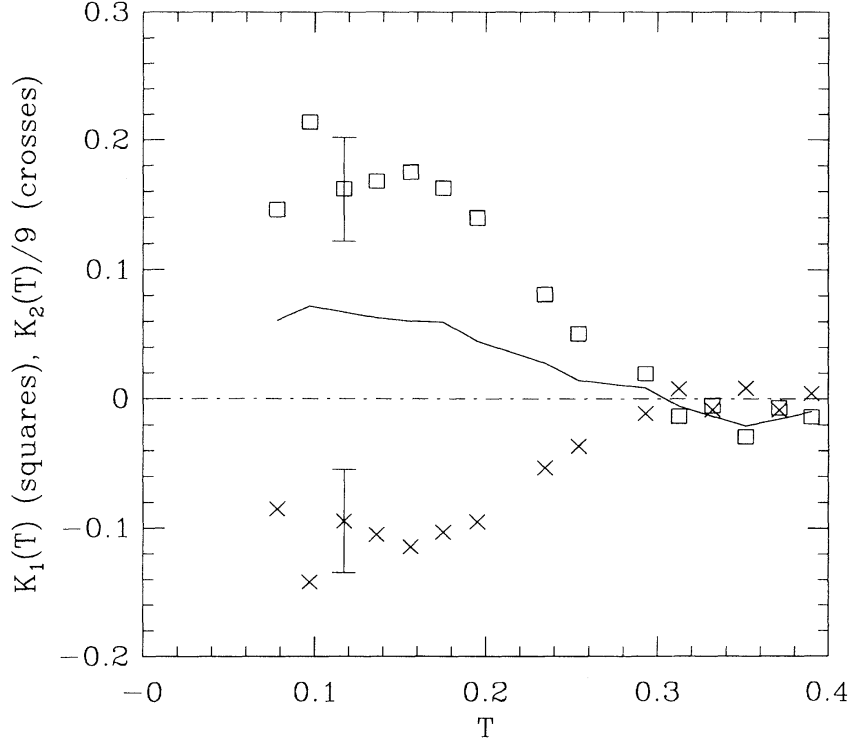


Figure 7.1: Reproduced from Ref. [123]. The anisotropy constants $K_1(T)$ (squares) and $K_2(T)/9$ (crosses) are plotted. K_1 and K_2 are the coefficients of the anisotropic fourth and sixth order terms in the free-energy allowed by cubic symmetry and are given by: $\mathcal{F}^{\text{aniso}}(\hat{M}) = K_1(T) \sum_{a,b;a \neq b} m_a^2 m_b^2 + K_2(T) m_0^2 m_1^2 m_2^2$ where \hat{M} and m_a with $a = 0, 1, 2$ are defined in Eqs. (7.10, 7.11), respectively. $\mathcal{F}^{\text{aniso}}([100]) = 0$ and $\mathcal{F}^{\text{aniso}}([111]) = K_1(T)/3 + K_2(T)/27$. The solid line shows the value of $K_1(T) + K_2(T)/9$. For $0.3 < T < 0.4$, $\mathcal{F}^{\text{aniso}}([111]) < 0$ and as a result $[111]$ polarization direction is the lower free energy state. However, for $T < 0.3$, the low energy state has polarization along $[100]$ direction since $\mathcal{F}^{\text{aniso}}([111]) > 0$.

We found the system orders ferromagnetically at $T_c^{\text{MF}}/\mathcal{J}_{\text{dip}} \approx 5.5$ and the free-energy of the system is independent of the polarization direction. This indicates the emergence of an $O(3)$ symmetry at the s-MFT level in the ordered phase. Since the Hamiltonian of the system possesses a cubic symmetry, we expect the $O(3)$ emergent symmetry to be broken by introducing fluctuations beyond s-MFT in the free-energy of the system. To investigate the possible outcomes of this symmetry breaking, we consider the Ginzburg-Landau (GL) free-energy for a system of classical 3-component Heisenberg spins on a lattice with cubic symmetry (FCC lattice in our case), given by [125] :

$$\mathcal{F}_{\text{GL}} = r \sum_{a=0}^2 m_a^2 + u \left(\sum_{a=0}^2 m_a^2 \right)^2 + v \sum_{a=0}^2 m_a^4 \quad (7.4)$$

where

$$m_a = \frac{1}{N} \sum_{i=1}^N \langle \mathbf{S}_i \cdot \hat{e}^a \rangle \quad (7.5)$$

and \hat{e}^a $a = 0, 1, 2$ are three cubic orthogonal Cartesian directions. Eq. (7.4) is the well-known n -vector model with $n = 3$ in this case. The details regarding different scenarios that may occur in different cases corresponding to various signs of u and v , were discussed in Chapter 4, Section 4.2. Expansion of the s-MFT free-energy (see Eq. (3.6)) up to quartic order shows that in this problem, the $u > 0$ and $v = 0$, at the s-MFT level. Consequently, we expect that the fluctuations generate cubic anisotropy with a $v \neq 0$ value that breaks the emergent $O(3)$ symmetry. If $v > 0$ in Eq. (7.4), the state polarized in the [111] direction will be selected by thermal fluctuations at $T \lesssim T_c$. On the other hand, if $v < 0$, thermal fluctuations select the [100] polarized state at $T = T_c^-$. Away from criticality i.e. away from $T = T_c^-$ regime, based on the cubic symmetry of the system, we also expect a cubic anisotropy to lift the accidental $O(3)$ degeneracy.

To expose the effect of thermal and quantum fluctuations in breaking the $O(3)$ symmetry in $T = 0^+$ regime, we use the spin wave theory. We then employ the E-TAP method and the Monte Carlo simulations to investigate the effect of thermal fluctuations at $T = T_c^-$ and $0^+ \leq T \leq T_c^-$, respectively.

7.3 The effect of fluctuations

7.3.1 Spin wave calculations

We use spin-wave theory to calculate the effect of fluctuations on the selection of the long-range ordered state among the $O(3)$ classically degenerate states at the s-MFT level in the $T = 0^+$ regime. As stated in Chapter 3, Section 3.4, we consider the polarization direction to be the z axis. To perform the spin wave calculations, one needs to find the Fourier transform of the Hamiltonian in Eq. (7.1) in a coordinate system where the z axis is the polarization direction. To do so, we first use the Ewald summation method in reciprocal space presented in Ref. [56] to find $\mathcal{J}_g^{\mu\nu}(\mathbf{k})$, the Fourier transform of $\mathcal{J}_{ij}^{\mu\nu}$ which is the bilinear spin-spin coupling matrix defined through the Hamiltonian of Eq. (7.1). We next find $\mathcal{J}^{\mu\nu}(\mathbf{k}) = \sum_{\alpha} R^{\mu\alpha} \mathcal{J}_g^{\alpha\nu}(\mathbf{k})$ where

$$R \equiv \begin{pmatrix} -\cos(\theta)\cos(\phi) & -\cos(\theta)\sin(\phi) & \sin(\theta) \\ \sin(\phi) & -\cos(\phi) & 0 \\ \sin(\theta)\cos(\phi) & \sin(\theta)\sin(\phi) & \cos(\theta) \end{pmatrix}. \quad (7.6)$$

$\mathcal{J}^{\mu\nu}(\mathbf{k})$ is Fourier transform of the coupling matrix in the coordinate system with polarization direction defined by θ and ϕ , the polar and azimuthal angles of the desired polarization direction, respectively. Considering Eq. (3.42) in Chapter 3, the dispersion relation then reads

$$\frac{\omega^2(\mathbf{k})}{S^2} = -\left(\mathcal{J}^{xy}(\mathbf{k})\right)^2 + \left(\mathcal{J}^{zz}(0)\right)^2 - \mathcal{J}^{zz}(0)\left(\mathcal{J}^{xx}(\mathbf{k}) + \mathcal{J}^{yy}(\mathbf{k})\right) + \mathcal{J}^{xx}(\mathbf{k})\mathcal{J}^{yy}(\mathbf{k}) \quad (7.7)$$

The free-energy corrections due to spin-wave theory for a given polarization direction specified by θ and ϕ is given by [126]

$$F_{\text{magnon}} = \sum_{\mathbf{k}} k_{\text{B}}T \ln\left[\sinh\left(\frac{\hbar\omega(\mathbf{k})}{2k_{\text{B}}T}\right)\right], \quad (7.8)$$

where the $\sum_{\mathbf{k}}$ is performed over the first Brillouin zone. Eq. (7.8) can consider thermal and quantum fluctuations at $T = 0^+$ and $T = 0$ respectively. Contour plot in Fig. 7.2, shows the value of F_{magnon} in the limit $T \rightarrow 0$, the zero point energy $E_0 = \sum_{\mathbf{k}} \hbar\omega(\mathbf{k})/2$, for different polarization direction in terms of polar and azimuthal angles, θ and ϕ , respectively. The minimum occurs at the angles corresponding to [111] directions indicating the classical $O(3)$ degeneracy is lifted as a result and the [111] polarized state is selected at $T = 0$. The result of the $O(3)$ symmetry breaking is the same at $\hbar \rightarrow 0$ limit i.e. $F_{\text{magnon}} = \sum_{\mathbf{k}} k_{\text{B}}T \ln(\hbar\omega(\mathbf{k}))$ has its minimum at θ and ϕ corresponding to [111] directions.

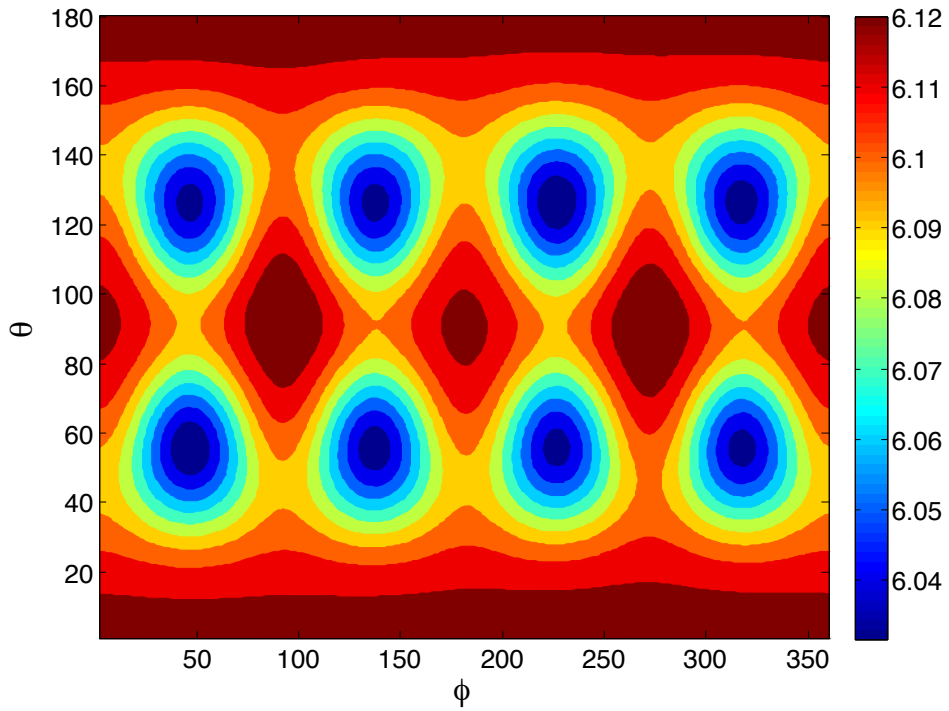


Figure 7.2: Contour plot of zero point energy, E_0 , for different polarization directions. As it can be seen in the figure, the minima occurs at the angles corresponding to [111] polarization directions. As a result, spin wave calculations shows that [111] is the state selected by ObD mechanism at $T = 0$.

We note that our spin wave calculation result, i.e. the selection of [111] polarized state by thermal and quantum fluctuations in $T = 0^+$ regime contradicts the result presented in Ref. [123] suggesting a [100] polarization direction in $T < 3T_c/4$ regime (see Fig. 7.1).

7.3.2 E-TAP

To analytically account for the fluctuation corrections to s-MFT free-energy at $T \lesssim T_c$, we employ the E-TAP method. Based on our GL theory analysis, we expect the $O(3)$ symmetry to break by a cubic anisotropy at the quartic order in the GL free-energy at $T = T_c^-$. According to our E-TAP calculations in Chapter 4, Section 4.3, the lowest order E-TAP term that generates the quartic order cubic anisotropy is given by

$$\Omega = -\frac{\beta}{4} \sum_{i,j} \sum_{\alpha\beta\gamma\delta} J_{ij}^{\alpha\gamma} J_{ij}^{\beta\delta} \chi_i^{\alpha\beta} \chi_j^{\gamma\delta}. \quad (7.9)$$

Here, $\chi_i^{\alpha\beta} = \langle S_i^\alpha S_i^\beta \rangle - \langle S_i^\alpha \rangle \langle S_i^\beta \rangle$ is the on-site susceptibility. We recall that $\chi_i^{\alpha\beta}$ can be calculated at $T = T_c^-$ in terms of $m_i^\mu = \langle S_i^\mu \rangle$ by using Eqs. (3.33, 3.36) from Section 3.3. Accordingly, we evaluate $\Omega(\theta, \phi)$ for different polarization directions. The $O(3)$ degeneracy is lifted upon considering the contribution of Ω to s-MFT free-energy. Fig. 7.3 shows the outcome of calculating Ω for different polarization directions. Considering the minima in the contour plot of this figure, the states with the lowest free-energy are the ones with polarization along $\langle 111 \rangle$ directions indicating the ObD selection at $T \lesssim T_c$.

7.3.3 Monte Carlo simulations

To complement our results obtained with spin wave theory and the E-TAP method and to investigate the intermediate temperature regime i.e. $0^+ < T < T_c$, we performed Monte Carlo simulations. We used Metropolis and heat bath algorithms in our simulations along with parallel tempering swaps. We performed our simulations for three system sizes $L = 4, 8, 12$ where L is the linear dimension of the system. For each system sizes about 10^8 spin flips per spin were attempted with an acceptance rate of about 50% for the Metropolis algorithm. Replica swaps were tried after every 10^3 spin slip attempts. To account for long range dipolar interaction, we employed the Ewald summation technique [56].

We aimed to study how fluctuations break the emergent $O(3)$ symmetry in the 3-vector model. Since the situation in this problem is similar to the one for 4-vector model presented

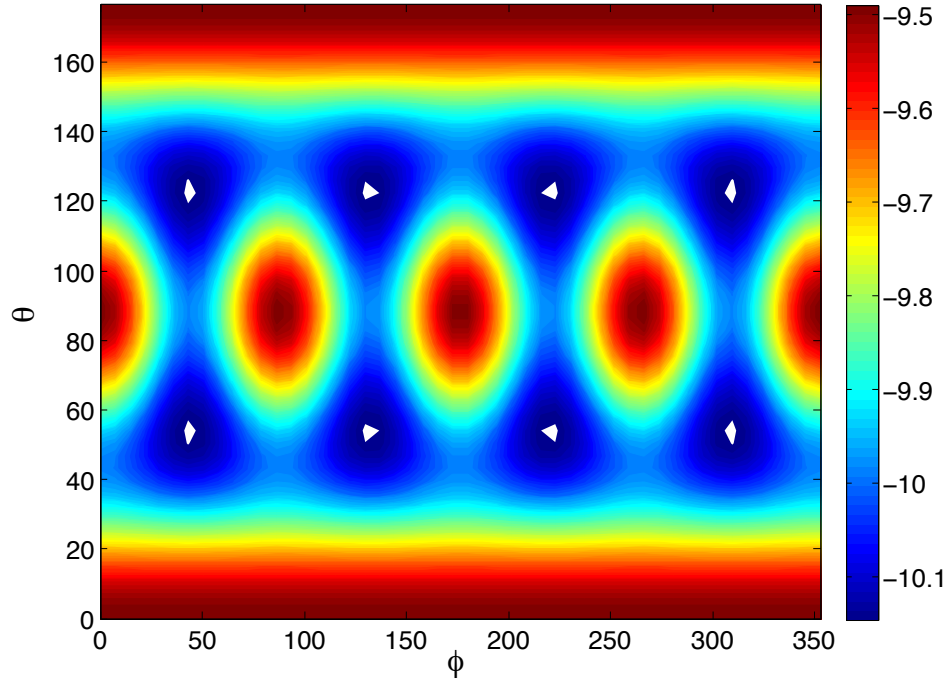


Figure 7.3: Contour plot of Ω for different polarization directions. The minima occurs at θ and ϕ corresponding to $[111]$ direction's polar and azimuthal angles. Consequently, the E-TAP calculations show that $[111]$ is the state selected by ObD mechanism at $T \lesssim T_c$ regime.

in Chapter 4, we utilized the same concepts in defining the necessary order parameters for this problem. First, we define M the order parameter that indicates ferromagnetic order:

$$M \equiv \left\langle \sqrt{\sum_{a=0}^2 m_a^2} \right\rangle \quad (7.10)$$

where

$$m_a = \frac{1}{N} \sum_{i=1}^N \mathbf{S}_i \cdot \hat{e}^a. \quad (7.11)$$

Here, \hat{e}^a with $a = 0, 1, 2$ are three cubic orthogonal directions and $\langle \dots \rangle$ represent Monte Carlo average. As the system enters the ordered phase, the M order parameter grows indicating the system orders ferromagnetically. However, the polarization of the ordered phase can not be determined by M . As a result, we need to define the *distance* parameters similar to d_{1k} and d_{4k} in Chapter 4 to identify the polarization of the ordered state. Guided by our spin wave and E-TAP calculations and to resolve the contradiction with the result of Ref. [123] on the polarization of the ordered phase at $T < 0.75T_c$, we define the distance parameters d_{100} and d_{111} below. Considering the unit sphere in 3D, there are six "[100] points" corresponding to [100] polarization direction including $(\pm 1; 0; 0)$, $(0; \pm 1; 0)$ and $(0; 0; \pm 1)$. Similarly, there are eight "[111] points" on the 2-sphere. Given a certain spin configuration obtained in our Monte Carlo simulation, we calculate $\hat{M} \equiv (m_0, m_1, m_2)/M$ where M and m_a with $a = 0, 1, 2$ are defined in Eqs. (7.10, 7.11), respectively. The d_{100} and d_{111} are then defined as the minimum Euclidean distance between point \hat{M} and all of the [100] and [111] points, respectively. The thermal average of $d_{100}(d_{111})$ is expected to decrease if the system orders in a state polarized along [100]([111]) direction. The details regarding calculation of these thermal average are presented in Chapter 4 for d_{1k} and d_{4k} which is applicable to the case of d_{100} and d_{111} .

The results of the simulations using Metropolis algorithm are presented in Fig. 7.4. The growth of M indicates the system enters a ferromagnetically ordered states. The decrease of d_{111} and increase of d_{100} which are enhanced as the system size increases, indicate the system polarizes along [111] direction. At low temperatures $T/\mathcal{J}_{\text{dip}} \leq 0.1$, however, it seems that the d_{111} and d_{100} are about to cross. This effect seems to strengthen as the system size is increased. To make sure, this effect is not an artifact of non-ergodicity at low temperatures¹, we repeat the simulations using the heat bath algorithm (see Section 3.2 in Chapter 3). We also utilize the parallel tempering method here where a replica swap

¹At low temperatures single spin update are less likely to be accepted, due to energy barriers between different microstates of the system. As a result, equilibrium is harder to reach.

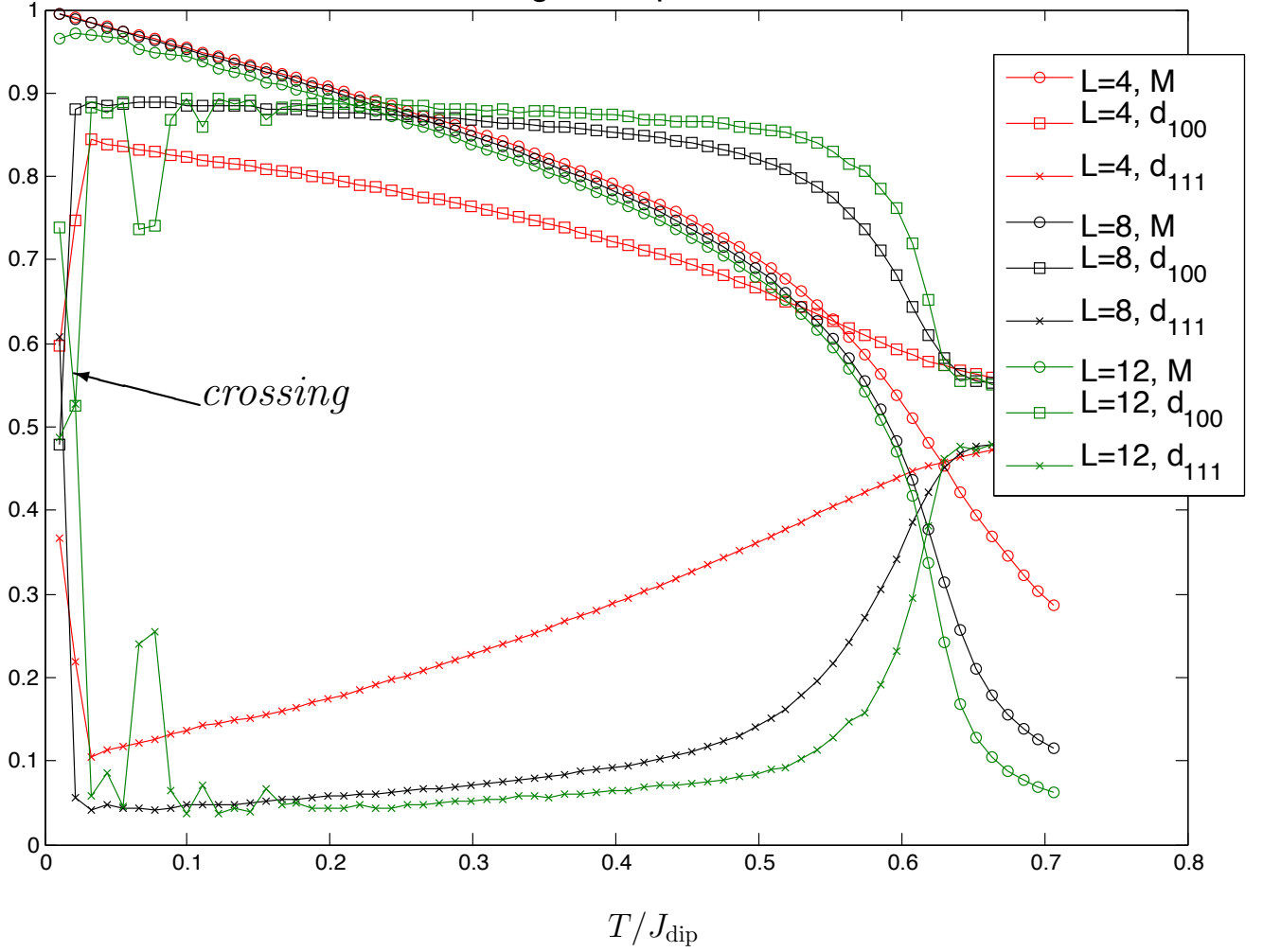


Figure 7.4: Metropolis algorithm results: Here, \mathcal{J}_{dip} is the strength of the dipolar interaction. M , d_{100} and d_{111} are shown for $L = 4, 8, 12$. The paramagnetic value of d_{100} and d_{111} correspond to minimum distance of a random point on 2-sphere from $[100]$ points and $[111]$ points, respectively.

is attempted in every 10^3 single spin update attempt. The results are shown in Fig. 7.5. The crossings between d_{100} and d_{111} observed in Metropolis simulations, do not appear in the heat bath ones, indicating previous poor equilibration. In order to make sure that the system, is not trapped in a local minimum of free-energy, we performed simulations with different initial conditions². However, the outcome did not change. The d_{100} increased as d_{111} decreased, indicating the system orders ferromagnetically and is polarized in [111] direction. This effect is also enhanced as the system size increased.

Performing both Metropolis and heat bath simulations, we observe no transition to a state polarized along [100] at $T < 0.75T_c$ as suggested in Ref. [123]. The system enters and stays in [111] polarized state at all temperature below T_c .

7.4 Conclusion and future Work

In our investigations regarding the problem of ObD selection in the FCC dipolar system, we find that the $O(3)$ symmetry observed in s-MFT treatment is broken by fluctuations which select a ferromagnetic state polarized along one of the [111] cubic directions. The system remains polarized in this direction down to low temperatures. Our current result is in contradiction with the results of Ref. [123] where they find a second transition to a ferromagnetic state polarized along [100] direction. Our results are supported by both spin wave theory, Monte Carlo simulations and E-TAP calculations.

To further investigate the potential pitfalls of this problem and to make sure there is no intermediate [100] polarized phase, one needs to utilize other types of updates (e.g. cluster updates). This establishes a plan for future continuation of this problem.

²Either all replicas were polarized in the same direction or all of them were random

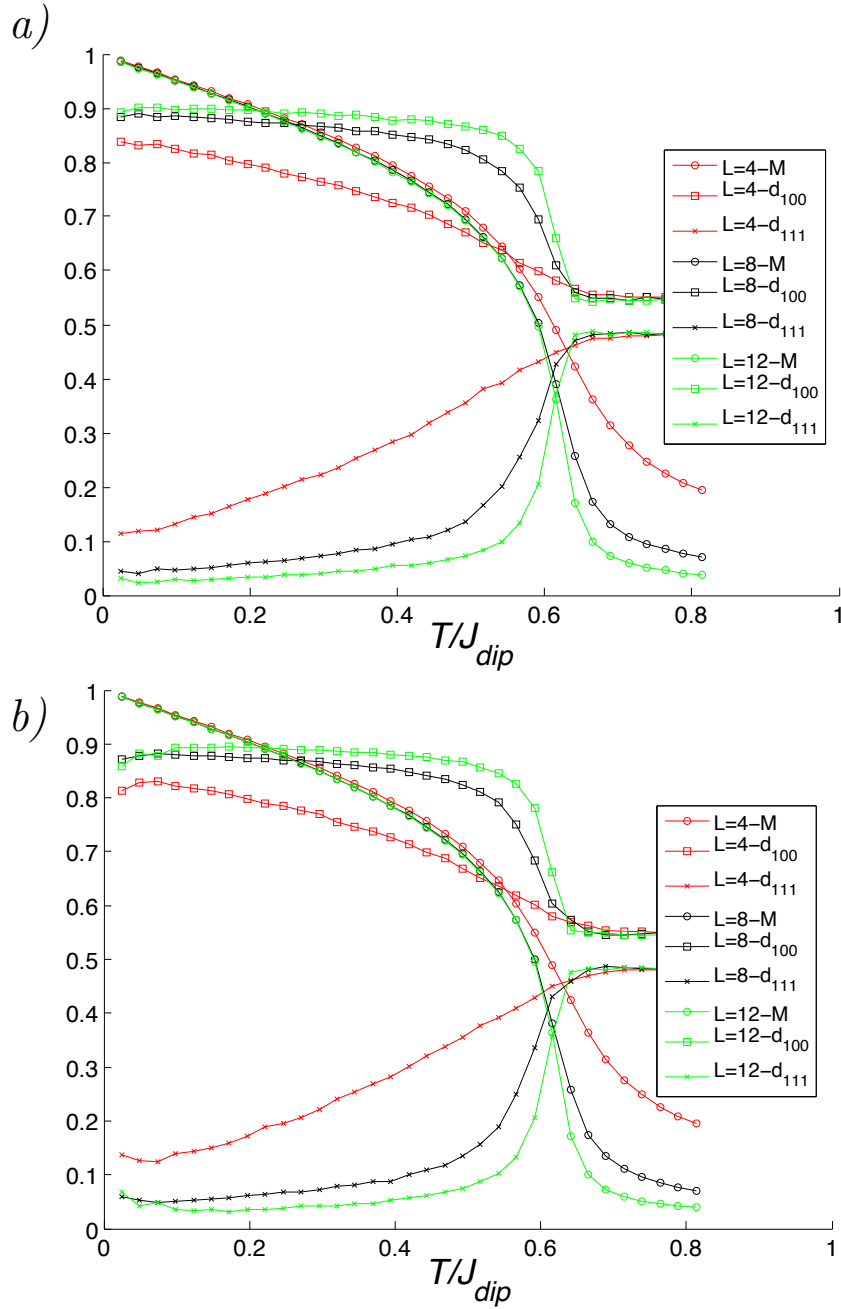


Figure 7.5: Heat bath algorithm : \mathcal{J}_{dip} is the dipolar interaction strength. M , d_{100} and d_{111} are shown for $L = 4, 8, 12$. The simulations started from *a)* random states and *b)* a [100] polarized states for all replicas. The paramagnetic value of d_{100} and d_{111} correspond to minimum distance of a random point on 2-sphere from [100] points and [111] points, respectively.

Chapter 8

Conclusion

In this thesis, we explored the phenomenon of order-by-disorder (ObD). This phenomenon had been mostly studied as a selection mechanism of *the ground state* of a system, out of a manifold of classically degenerate states. In this thesis, we looked at this phenomenon from a different perspective. We showed how fluctuations, close to a phase transition, can determine a long range ordered state. We considered a situation where degenerate soft modes of a system at criticality are related to each other by operation of an exact *accidental* symmetry at the standard mean-field theory (s-MFT) level. In such cases, fluctuations are capable of breaking this symmetry and can select a particular long-range ordered state. To study the physics beyond mean field approximation in $T = T_c^-$ regime, in this thesis, we employed Monte Carlo simulations as well as the E-TAP method. The E-TAP is an extended version of a method originally proposed by Thouless, Anderson and Palmer (TAP) to study fluctuations in spin glasses. The TAP method was then reformulated by Plefka and expanded upon by Georges and Yadidia for Ising model. In this thesis, we derived the Heisenberg model equivalent of the expansion of Georges and Yadidia. We used E-TAP to analytically specify the role of fluctuations at temperature regimes close to criticality. This is a high temperature expansion method that calculates fluctuations about a mean field theory solution. Beside E-TAP and Monte Carlo simulation, we used spin wave theory to investigate fluctuation effects at $T = 0^+$ temperatures.

We considered frustrated spins systems on pyrochlore and FCC lattices. In the former group, the spins interact via a rather complicated Hamiltonian that could include the most general nearest-neighbour symmetry allowed bilinear interactions (mg-Hamiltonian), long-range magnetostatic dipole-dipole interactions and second and/or third nearest-neighbour exchange interactions. While in the latter group, the Hamiltonian only consists of long-range magnetostatic dipole-dipole interactions. These two model Hamiltonians correspond

to two classes of magnetic materials, insulating rare-earth pyrochlore oxides and rare-earth FCC salts, respectively.

Our studies on pyrochlore systems were motivated by the recent experimental and theoretical works on $\text{Gd}_2\text{Ti}_2\text{O}_7$ and $\text{Er}_2\text{Ti}_2\text{O}_7$. In Chapter 4, we showed that a partially ordered state (POS) can occur in a pyrochlore system. At the s-MFT level, in a certain region of the parameter space of the mg-Hamiltonian amended to include long range dipolar interaction and/or second and/or third nearest-neighbours exchange interactions, an accidental $O(4)$ symmetry emerged. This symmetry generates a degeneracy between two types of POS, $1-\mathbf{k}$ and $4-\mathbf{k}$ states. We demonstrated that fluctuations break this symmetry by introducing a cubic anisotropy in a 4-vector model. Consequently, the degeneracy between POS's were lifted and according to microscopic details either $1-\mathbf{k}$ or $4-\mathbf{k}$ states were selected. We used Monte Carlo simulations and E-TAP method to study fluctuations. Our results address the long standing problem of the $4-\mathbf{k}$ spin configuration of the intermediate phase of $\text{Gd}_2\text{Ti}_2\text{O}_7$. However, the low temperature spin configuration of this compound still remains an enigma. Our results suggest a $2-\mathbf{k}$ state as a possible candidate for $\text{Gd}_2\text{Ti}_2\text{O}_7$'s low temperature phase which contradicts the existing result. However, further experiments are required to address this issue. Based on our Ginzburg-Landau analysis, we predicted that the critical behaviour of $\text{Gd}_2\text{Ti}_2\text{O}_7$ should be classified under the 3D $n = 4$ cubic universality class. Performing new experiments and conducting new numerical studies (i.e. Monte Carlo simulations) seem to be a daunting task to confirm this prediction. On the experimental side, the difficulty occurs since the value of critical exponents of 3D $n = 4$ cubic universality class is very close to the ones that belong to other 3D universality classes. An obstacle in conducting Monte Carlo studies in these systems stems from the presence of the long-range dipolar interaction which creates limitation for simulating larger system sizes, necessary to study criticality. We note that in the case of $1-\mathbf{k}$ selection where one expects a fluctuation induced first order transition from paramagnetic phase to $1-\mathbf{k}$ state, the same problem exists. However, one can avoid the problem by using second and third nearest-neighbours interactions instead of long-range dipolar one. This can be the topic for a future research project.

In Chapter 5, we studied the mg-Hamiltonian in a certain region of its parameter space known as Γ_5 region. At the s-MFT level, $U(1)$ symmetry emerges in this region. For a specific part of the Γ_5 region (where the coupling $J_{zz} = 0$), we showed that fluctuations introduce a hexagonal anisotropy and break the $U(1)$ symmetry, by using E-TAP method up to order β^6 . We obtained the phase diagram resulting from the ObD selection in this part of the parameter space. Our study in this chapter was focused on developing the E-TAP method to calculate the hexagonal anisotropy by means of a diagrammatic approach. This project is in its early stage of development in the context of frustrated systems.

The results obtained in this chapter needs to be benchmarked by performing Monte Carlo simulations which does not seem too demanding in terms of computational resources. Since we performed our E-TAP calculations for a $J_{zz} = 0$ part of the Γ_5 region, a possible extension of the project could be to obtain the E-TAP corrections for $J_{zz} \neq 0$ region. This is a demanding project in terms of analytical complications involved in calculating different terms in E-TAP expansion. However, it is not impossible to do and the efforts puts into this direction can also be steered towards developing a computer program capable of calculating different terms in E-TAP expansion.

In continuation of our investigation in Chapter 5, on ObD generated hexagonal anisotropy in lifting the accidental $U(1)$ degeneracy, in Chapter 6, we focused on mg-Hamiltonian with its parameters tuned to a specific point in the Γ_5 region. This model is obtained using experimental data to describe rare-earth pyrochlore oxide $\text{Er}_2\text{Ti}_2\text{O}_7$. Due to the importance of long-range dipolar interaction in this group of materials, we studied a model including this interaction as well as the mg-Hamiltonian corresponding to $\text{Er}_2\text{Ti}_2\text{O}_7$. Using Monte Carl simulations, we demonstrated that this model goes through a continuous phase transition from paramagnetic phase to a long-range ordered phase, which can be classified under 3D XY universality class. The ObD mechanism selects the long-range ordered phase, the so called ψ_2 state, which is the same with and without the presence of the long-range dipolar interaction. However, the transition temperature to ψ_2 increases when the long-range dipolar interaction is considered. This remains to be confirmed by studying how the long-range dipolar interaction affects the energy of the ψ_2 state.

In Chapter 7, we changed gear from pyrochlore structure to FCC lattice. We considered a system of point dipoles on FCC lattice sites interacting via the long-range dipolar interaction. This is one the simplest models that exhibit the ObD phenomenon. The materials described by this model are the rare-earth FCC salts. These material order ferromagnetically at low temperatures and so does the system of FCC point dipoles on FCC lattice. At the s-MFT level, an $O(3)$ symmetry emerges. Employing the E-TAP method, spin wave theory and Monte Carlo simulations, we studied the effect of fluctuations in this system. We found that fluctuations break the accidental $O(3)$ symmetry by generating a cubic anisotropy in a 3-vector model and select a state polarized along $[111]$ cubic direction down to low temperatures. However, the selected direction is a matter of debate at the moment. Early Monte Carlo studies by Bouchaud and Zérah, suggest that the polarization direction changes from $[111]$ to $[100]$ at low temperatures. Our results do not support their conclusion. To further confirm this issue, Monte Carlo simulation with advanced updating techniques can be helpful. The investigations presented in this chapter may also be considered as the primary step before studying a Hamiltonian including single site anisotropy which represents a system of nanoparticles on FCC lattice

At the end, we hope that our investigation on ObD problem at criticality open a new avenue in the study of the effect of fluctuations in frustrated systems. From a broader methodological perspective, our E-TAP method for spin models with anisotropic interactions could be applied to other magnetically frustrated systems where the question of selection of the long-range order at T_c is of interest. This is useful in particular, if the low-temperature state is separated by a phase transition from the state selected at T_c . In such a case, an understanding of *the ground state* at $T = 0^+$ can *not* be leveraged to explain the situation at T_c . In addition, the E-TAP analytical description of fluctuations at the microscopic level may help shed light on the role of individual symmetry-allowed interactions in an ObD selection near critical temperature. As another methodological extension, the E-TAP method can be modified to include quantum mechanical effects which broadens the reach of this method in studying phenomena that may occur close to criticality.

Part III

APPENDICES

Appendix A

Pyrochlore Lattice

The pyrochlore lattice is a non-Bravais lattice with a tetrahedral basis on the sites of a FCC lattice. In this thesis we choose the following conventions. $\mathbf{R}_i \equiv \mathbf{r}_i - \mathbf{r}^\alpha$ are the FCC lattice position vectors and \mathbf{r}_i are pyrochlore lattice position vectors. The vector \mathbf{r}^α specifies the bases' positions in the pyrochlore lattice and are given by:

$$\mathbf{r}^0 = (0, 0, 0) \quad (\text{A.1a})$$

$$\mathbf{r}^1 = \left(\frac{1}{\sqrt{2}}, \frac{1}{\sqrt{2}}, 0\right) \quad (\text{A.1b})$$

$$\mathbf{r}^2 = \left(\frac{1}{\sqrt{2}}, 0, \frac{1}{\sqrt{2}}\right) \quad (\text{A.1c})$$

$$\mathbf{r}^3 = \left(0, \frac{1}{\sqrt{2}}, \frac{1}{\sqrt{2}}\right). \quad (\text{A.1d})$$

The above coordinates are expressed in units of r_{nn} , the nearest-neighbor distance in pyrochlore structure.

The local coordinate system on each sublattice are defined below:

$$x_0^{\text{local}} = \frac{1}{\sqrt{6}}(-1, -1, 2) \quad (\text{A.2a})$$

$$y_0^{\text{local}} = \frac{1}{\sqrt{2}}(1, -1, 0) \quad (\text{A.2b})$$

$$z_0^{\text{local}} = \frac{1}{\sqrt{3}}(1, 1, 1) \quad (\text{A.2c})$$

$$x_1^{\text{local}} = \frac{1}{\sqrt{6}}(1, 1, 2) \quad (\text{A.3a})$$

$$y_1^{\text{local}} = \frac{1}{\sqrt{2}}(-1, 1, 0) \quad (\text{A.3b})$$

$$z_1^{\text{local}} = \frac{1}{\sqrt{3}}(-1, -1, 1) \quad (\text{A.3c})$$

$$x_2^{\text{local}} = \frac{1}{\sqrt{6}}(1, -1, -2) \quad (\text{A.4a})$$

$$y_2^{\text{local}} = \frac{1}{\sqrt{2}}(-1, -1, 0) \quad (\text{A.4b})$$

$$z_2^{\text{local}} = \frac{1}{\sqrt{3}}(-1, 1, -1) \quad (\text{A.4c})$$

$$x_3^{\text{local}} = \frac{1}{\sqrt{6}}(-1, 1, -2) \quad (\text{A.5a})$$

$$y_3^{\text{local}} = \frac{1}{\sqrt{2}}(1, 1, 0) \quad (\text{A.5b})$$

$$z_3^{\text{local}} = \frac{1}{\sqrt{3}}(1, -1, -1) \quad (\text{A.5c})$$

Appendix B

Partially Ordered State in s-MFT

In this appendix we show that, at the standard mean field theory (s-MFT) level, the $1\text{-}\mathbf{k}$ and $4\text{-}\mathbf{k}$ states, introduced in Chapter 4, have the same free energy with and without considering the effect of the crystal electric field in the pyrochlore lattice.

B.1 Defining primary tools

We begin by defining the orientation of the moments, $\hat{e}_{\mathbf{k}_a}^\alpha$, on a typical tetrahedron that makes up a $1\text{-}\mathbf{k}$ state. Here, $\alpha = 0, \dots, 3$ corresponds to one of the four bases (sublattices) of the pyrochlore structure (see Eq. (A.1)) and \mathbf{k}_a refers to ordering wave vector of the corresponding $1\text{-}\mathbf{k}$ state. $\hat{e}_{\mathbf{k}_a}^\alpha$'s are given in Table B.1 and are expressed in global Cartesian coordinates.

\mathbf{k}_a	sublattice 0	sublattice 1	sublattice 2	sublattice 3
$\mathbf{k}_0 = (\frac{1}{2}, \frac{1}{2}, \frac{1}{2})$	$\hat{e}_{\mathbf{k}_0}^0 = (0, 0, 0)$	$\hat{e}_{\mathbf{k}_0}^1 = (\frac{-1}{\sqrt{2}}, \frac{1}{\sqrt{2}}, 0)$	$\hat{e}_{\mathbf{k}_0}^2 = (\frac{1}{\sqrt{2}}, 0, \frac{-1}{\sqrt{2}})$	$\hat{e}_{\mathbf{k}_0}^3 = (0, \frac{-1}{\sqrt{2}}, \frac{1}{\sqrt{2}})$
$\mathbf{k}_1 = (-\frac{1}{2}, -\frac{1}{2}, \frac{1}{2})$	$\hat{e}_{\mathbf{k}_1}^0 = (\frac{1}{\sqrt{2}}, \frac{-1}{\sqrt{2}}, 0)$	$\hat{e}_{\mathbf{k}_1}^1 = (0, 0, 0)$	$\hat{e}_{\mathbf{k}_1}^2 = (0, \frac{1}{\sqrt{2}}, \frac{1}{\sqrt{2}})$	$\hat{e}_{\mathbf{k}_1}^3 = (\frac{-1}{\sqrt{2}}, 0, \frac{-1}{\sqrt{2}})$
$\mathbf{k}_2 = (-\frac{1}{2}, \frac{1}{2}, -\frac{1}{2})$	$\hat{e}_{\mathbf{k}_2}^0 = (\frac{-1}{\sqrt{2}}, 0, \frac{1}{\sqrt{2}})$	$\hat{e}_{\mathbf{k}_2}^1 = (0, \frac{-1}{\sqrt{2}}, \frac{-1}{\sqrt{2}})$	$\hat{e}_{\mathbf{k}_2}^2 = (0, 0, 0)$	$\hat{e}_{\mathbf{k}_2}^3 = (\frac{1}{\sqrt{2}}, \frac{1}{\sqrt{2}}, 0)$
$\mathbf{k}_3 = (\frac{1}{2}, -\frac{1}{2}, -\frac{1}{2})$	$\hat{e}_{\mathbf{k}_3}^0 = (0, \frac{1}{\sqrt{2}}, \frac{-1}{\sqrt{2}})$	$\hat{e}_{\mathbf{k}_3}^1 = (\frac{1}{\sqrt{2}}, 0, \frac{1}{\sqrt{2}})$	$\hat{e}_{\mathbf{k}_3}^2 = (\frac{-1}{\sqrt{2}}, \frac{-1}{\sqrt{2}}, 0)$	$\hat{e}_{\mathbf{k}_3}^3 = (0, 0, 0)$

Table B.1: Spin configurations of a single tetrahedron in $1\text{-}\mathbf{k}$ states

The orientation of the rest of the moments in a $1\text{-}\mathbf{k}$ state can be obtained from a single tetrahedron configuration using the following equation:

$$\hat{e}_{\mathbf{k}_a}(\mathbf{r}_i) = \hat{e}_{\mathbf{k}_a}^\alpha \cos(\mathbf{k}_a \cdot \mathbf{R}_i) \quad (\text{B.1})$$

where $\mathbf{R}_i \equiv \mathbf{r}_i - \mathbf{r}^\alpha$ are the FCC lattice position vectors, \mathbf{r}_i are pyrochlore lattice position vectors. The vector \mathbf{r}^α are defined in Appendix A. The spin orientations corresponding to the $4\text{-}\mathbf{k}$ states can be expressed in terms of linear combinations of the four $1\text{-}\mathbf{k}$ states:

$$\hat{e}_{4\mathbf{k}}(\mathbf{r}_i) \equiv \sum_{a=0}^3 \hat{\psi}_a \hat{e}_{\mathbf{k}_a}(\mathbf{r}_i). \quad (\text{B.2})$$

Here $\hat{\psi}_a = \pm 1/2$ conveniently keeps $\hat{e}_{4\mathbf{k}}(\mathbf{r}_i)$ normalized (except for the sites with zero moments) and generate all possible $4\text{-}\mathbf{k}$ states.

B.2 No crystal electric field

Having defined the $1\text{-}\mathbf{k}$ and $4\text{-}\mathbf{k}$ states, we now proceed to show that both the $1\text{-}\mathbf{k}$ and $4\text{-}\mathbf{k}$ states have the same s-MFT free energy. The general form of the s-MFT free energy for a classical 3-component spin, \mathbf{S}_i at site i reads [57]:

$$F = -\frac{1}{2} \sum_{i,j} m_i^\mu J_{ij}^{\mu\nu} m_j^\nu - \frac{1}{\beta} \sum_i \ln \left(4\pi \frac{\sinh(\beta h_i)}{\beta h_i} \right). \quad (\text{B.3})$$

$J_{ij}^{\mu\nu}$ is the bilinear spin-spin exchange coupling matrix defined through the Hamiltonian of Eq. (4.1) in Chapter 4. The magnetic moment, \mathbf{m}_i for both $1\text{-}\mathbf{k}$ and $4\text{-}\mathbf{k}$ states at site \mathbf{r}_i is obtained from the s-MFT self-consistent (Langevin function) equation,

$$\mathbf{m}_i = -\frac{\mathbf{h}_i}{h_i} \left[\coth(\beta h_i) - \frac{1}{\beta h_i} \right] \quad (\text{B.4})$$

where

$$h_i \equiv |\mathbf{h}_i| = \left| \sum_{j,\nu} J_{ij} m_j^\nu \right|. \quad (\text{B.5})$$

In what follows, we compare the free energy, F , within (s-MFT), of a $1\text{-}\mathbf{k}$ state, with 4-component order parameter, $\boldsymbol{\psi} = (|\boldsymbol{\psi}|, 0, 0, 0)$, with the free energy of a $4\text{-}\mathbf{k}$ state, with

4-component order parameter $\boldsymbol{\psi} = (|\boldsymbol{\psi}|/2, |\boldsymbol{\psi}|/2, |\boldsymbol{\psi}|/2, |\boldsymbol{\psi}|/2)$. We thus have $|\mathbf{m}_i| = |\boldsymbol{\psi}|$ which is also confirmed numerically by solving Eq. (B.4). We define for a 1- \mathbf{k} state:

$$\mathbf{m}_i = |\boldsymbol{\psi}| \hat{e}_{\mathbf{k}_a}(\mathbf{r}_i) \equiv \mathbf{m}_{\mathbf{k}_a}(\mathbf{r}_i) \quad (\text{B.6})$$

while we have for a 4- \mathbf{k} state:

$$\mathbf{m}_i = |\boldsymbol{\psi}| \hat{e}_{4\mathbf{k}}(\mathbf{r}_i) = \sum_{a=1}^4 \hat{\psi}_a \mathbf{m}_{\mathbf{k}_a}(\mathbf{r}_i) \equiv \mathbf{m}_{4\mathbf{k}}(\mathbf{r}_i). \quad (\text{B.7})$$

In Eq. (B.3), we are employing implicit summation convention for repeated Greek superscripts μ and ν which represent Cartesian coordinates.

We now show that both terms in Eq. (B.3) are the same for 1- \mathbf{k} and 4- \mathbf{k} states and thus, at a given temperature, the free-energy of 1- \mathbf{k} and 4- \mathbf{k} is the same at the s-MFT level.

First Term of Eq. (B.3): The first term, $F_1 \equiv -\frac{1}{2} \sum_{i,j} m_i^\mu J_{ij}^{\mu\nu} m_j^\nu$, reads for a typical 1- \mathbf{k} state:

$$F_1(1k) \equiv -\frac{1}{2} \sum_{ij} m_{\mathbf{k}_a}^\mu(\mathbf{r}_i) J_{ij}^{\mu\nu} m_{\mathbf{k}_a}^\nu(\mathbf{r}_j) \quad (\text{B.8})$$

Using Eqs. (B.1, B.6) we have:

$$F_1(1k) = -\frac{1}{2} \sum_{\alpha\beta} m_{\mathbf{k}_a}^\mu(\mathbf{r}^\alpha) J_{\alpha\beta}^{\mu\nu}(\mathbf{k}_a) m_{\mathbf{k}_a}^\nu(\mathbf{r}^\beta) \quad (\text{B.9})$$

where α and β are sublattice labels and $J_{\alpha\beta}^{\mu\nu}(\mathbf{k}_a)$ is the Fourier transform of $J_{ij}^{\mu\nu}$. Similarly, using Eqs. (B.7, B.8), F_1 for a 4- \mathbf{k} state can be written as:

$$F_1(4k) = -\frac{1}{2} \sum_{ij} \sum_{ab} \hat{\psi}_a \hat{\psi}_b m_{\mathbf{k}_a}^\mu(\mathbf{r}_i) J_{ij}^{\mu\nu} m_{\mathbf{k}_b}^\nu(\mathbf{r}_j). \quad (\text{B.10})$$

Using Eq. (B.1) we obtain:

$$F_1(4k) = -\frac{1}{2} \sum_{ab,\alpha\beta} \hat{\psi}_a \hat{\psi}_b m_{\mathbf{k}_a}^\mu(\mathbf{r}^\alpha) J_{\alpha\beta}^{\mu\nu}(\mathbf{k}_a) m_{\mathbf{k}_b}^\nu(\mathbf{r}^\beta) \delta_{ab}. \quad (\text{B.11})$$

Consequently,

$$F_1(4k) = -\frac{1}{2} \sum_{a;\alpha\beta} (\hat{\psi}_a)^2 m_{\mathbf{k}_a}^\mu(\mathbf{r}^\alpha) J_{\alpha\beta}^{\mu\nu}(\mathbf{k}_a) m_{\mathbf{k}_a}^\nu(\mathbf{r}^\beta) \quad (\text{B.12})$$

and using Eq. (B.9), we find:

$$F_1(4k) = \sum_a (\hat{\psi}_a)^2 F_1(1k). \quad (\text{B.13})$$

Considering that for all a , $\hat{\psi}_a = \pm \frac{1}{2}$, and all $F_1(1k)$ are the same, we thus have:

$$F_1(4k) = F_1(1k). \quad (\text{B.14})$$

Second Term of Eq. (B.3): In this term, the only variable that depends on different spin configurations is the magnitude of local field, h_i , in Eq. (B.5), which we focus on. Using Eq. (B.6), the local field, \mathbf{h}_i , experienced by a moment at site \mathbf{r}_i in a $1\text{-}\mathbf{k}$ state, is given by:

$$h_{\mathbf{k}_a}^\mu(\mathbf{r}_i) \equiv \sum_{j\nu} J_{ij}^{\mu\nu} m_{\mathbf{k}_a}^\nu(\mathbf{r}_j), \quad (\text{B.15})$$

while for a $4\text{-}\mathbf{k}$ state we have

$$h_{4k}^\mu(\mathbf{r}_i) \equiv \sum_{j\nu} J_{ij}^{\mu\nu} m_{4k}^\nu(\mathbf{r}_j) = \sum_a \hat{\psi}_a h_{\mathbf{k}_a}^\mu(\mathbf{r}_i). \quad (\text{B.16})$$

where $m_{4k}^\nu(\mathbf{r}_j) = \sum_a \hat{\psi}_a m_{\mathbf{k}_a}^\nu(\mathbf{r}_j)$. Within s-MFT, the local field at each site is antiparallel to the moment at that site. As a result, $\mathbf{h}_{\mathbf{k}_a}(\mathbf{r}_i)$ can be written as

$$\mathbf{h}_{\mathbf{k}_a}(\mathbf{r}_i) = C \mathbf{m}_{\mathbf{k}_a}(\mathbf{r}_i). \quad (\text{B.17})$$

Here, C is the same constant for each of the $1\text{-}\mathbf{k}$ states with $\mathbf{k} \equiv \mathbf{k}_a$ ($a = 0, 1, 2, 3$), since all of $1\text{-}\mathbf{k}$ states have the same free energy by definition.

Similarly, for the $4\text{-}\mathbf{k}$ state, using Eqs. (B.16, B.17), we find

$$\mathbf{h}_{4k}(\mathbf{r}_i) = C \sum_a \hat{\psi}_a \mathbf{m}_{\mathbf{k}_a}(\mathbf{r}_i) = C \mathbf{m}_{4k}(\mathbf{r}_i). \quad (\text{B.18})$$

Since we have $|\boldsymbol{\psi}|$ the same for both $1\text{-}\mathbf{k}$ and $4\text{-}\mathbf{k}$ states by construct, Eq. (B.18) shows that the magnitude of the local field is the same for $1\text{-}\mathbf{k}$ and $4\text{-}\mathbf{k}$ at the lattice sites with nonzero moments at a given temperature T . We note that, the theory is internally consistent, since we have taken $|\boldsymbol{\psi}|$ to be the same for both $1\text{-}\mathbf{k}$ and $4\text{-}\mathbf{k}$ states which is confirmed numerically as mentioned earlier. As a result, the second term in Eq. (B.3) is the same for $1\text{-}\mathbf{k}$ and $4\text{-}\mathbf{k}$.

Based on Eqs. (B.14, B.18) and Eq. (B.3), we therefore find that the s-MFT free energy is the same for the $1\text{-}\mathbf{k}$ and $4\text{-}\mathbf{k}$ states.

B.3 With crystal electric field

The discussion in the previous subsection, as well as in Chapter 4, has assumed for simplicity that the spin degrees of freedom, \mathbf{S}_i at each site i , is a classical vector of fixed length. As a result, the s-MFT treatment leads for the self-consistent equation for \mathbf{m}_i to the Langevin function in Eq. (B.4). Had we assumed a quantum \mathbf{S}_i , Eq. (B.4) would be replaced $\mathbf{m}_i = -\frac{\mathbf{h}_i}{h_i} B_S(h_i)$, where $B_S(x) = \frac{2S+1}{2S} \coth(\frac{2S+1}{2S}x) - \frac{1}{2} \coth(\frac{x}{2S})$ is the Brillouin function. In this case, one can repeat the argument of the Section B.2 and, again, show that the 1- \mathbf{k} and 4- \mathbf{k} states are degenerate.

One may then ask whether the single-ion anisotropy, arising from the crystal electrical field (CEF) effect, may change the conclusion that the 1- \mathbf{k} and 4- \mathbf{k} states are degenerate. Again, such a question can be asked for either classical or quantum spins \mathbf{S}_i . We now proceed to briefly show that introducing a crystal field anisotropy does not lift the degeneracy between the 1- \mathbf{k} and 4- \mathbf{k} states.

At the s-MFT level, the Hamiltonian including crystal electric field or single ion anisotropy (H_{CEF}) can be written as:

$$H_{\text{MF}} = \sum_{i=1}^N \left[\mathbf{h}_i \cdot \mathbf{S}_i + H_{\text{CEF}}(\mathbf{S}_i) - \frac{1}{2} \mathbf{h}_i \cdot \mathbf{m}_i \right], \quad (\text{B.19})$$

where H_{CEF} can be expressed in terms of Stevens' operators according to the symmetry of pyrochlore structure[11]:

$$H_{\text{CEF}}(\mathbf{S}_i) = \sum_{n=2,4,6} \sum_{m=0}^6 B_n^m O_n^m(\mathbf{S}_i). \quad (\text{B.20})$$

We consider \mathbf{S}_i expressed in terms of its components in the local [111] coordinate system.

The s-MFT free energy can be written as

$$F = -\frac{1}{\beta} \sum_{i=1}^N \ln(Z_i), \quad (\text{B.21})$$

where

$$Z_i = \text{Tr}[\exp(-\beta \mathbf{h}_i \cdot \mathbf{S}_i - \beta H_{\text{CEF}}(\mathbf{S}_i) + \frac{\beta}{2} \mathbf{h}_i \cdot \mathbf{m}_i)]. \quad (\text{B.22})$$

In what follows, we aim to compare the s-MFT free energy of 1- \mathbf{k} and 4- \mathbf{k} states using Eq. (B.21) without explicitly finding its global minimum. In Eq. (B.22), \mathbf{S}_i can be treated as

a classical vector or a quantum mechanical operator. However, we show that the outcome is independent of this choice. The result of performing the Tr in Eq. (B.22) can be written in general form of

$$\exp\left(\frac{\beta}{2}\mathbf{h}_i \cdot \mathbf{m}_i\right)\mathcal{G}(h_i^x, h_i^y, h_i^z, \beta). \quad (\text{B.23})$$

Since we are comparing the free energy of the 1- \mathbf{k} and 4- \mathbf{k} states, \mathbf{h}_i and \mathbf{m}_i are known for every i . So, we have

$$\exp\left(\frac{\beta}{2}\mathbf{h}_i \cdot \mathbf{m}_i\right) = \exp\left(\frac{\beta C|\psi|^2}{2}\right) \equiv \tilde{C}, \quad (\text{B.24})$$

which is the same for both 1- \mathbf{k} and 4- \mathbf{k} states. Here, C is the same constant in Eqs. (B.17, B.18). As a result, Eq. (B.23) can be rewritten as

$$\tilde{C}\tilde{\mathcal{G}}(h_i, \theta_i, \phi_i), \quad (\text{B.25})$$

where θ_i and ϕ_i are the polar and azimuthal angles of \mathbf{h}_i in the local [111] frame of coordinates. We dropped β from the argument of $\tilde{\mathcal{G}}$ for simplicity. Now we show the $\tilde{\mathcal{G}}$ is the same for both 1- \mathbf{k} and 4- \mathbf{k} states. According to Eq. (B.18), h_i is the same for both 1- \mathbf{k} and 4- \mathbf{k} states. Considering Table B.1 and Eq. (B.2), $\forall i$, $\theta_i = \pi/2$ for both of these states. On the other hand, ϕ_i can only have the following values: $\{\frac{\pi}{2}, \frac{3\pi}{2}, \frac{\pi}{6}, \frac{5\pi}{6}, \frac{7\pi}{6}, \frac{11\pi}{6}\}$ for both 1- \mathbf{k} and 4- \mathbf{k} states. Although for 1- \mathbf{k} and 4- \mathbf{k} states, these angles are distributed differently over the lattice, all of them are present in a typical 1- \mathbf{k} and 4- \mathbf{k} states. Since there is a sum over all lattice sites in Eq. (B.21), the outcome of this equation is the same for the 1- \mathbf{k} and 4- \mathbf{k} states. Consequently, including the crystal electric field in the s-MFT Hamiltonian does not differentiate between 1- \mathbf{k} and 4- \mathbf{k} states, free-energy-wise.

We numerically confirmed this result by minimizing Eq. (B.21) and solving the resulting s-MFT self-consistent equation where \mathbf{S}_i were spin-7/2 quantum mechanical operators and B_n^m coefficients in Eq. (B.20), were chosen in accordance with the experimental values for $\text{Gd}_2\text{Ti}_2\text{O}_7$ from Ref. [48]. We found that the 1- \mathbf{k} and 4- \mathbf{k} states have identical paramagnetic critical transition temperature, T_c , and identical free energy below T_c .

B.4 Emergent $O(4)$ symmetry up to quartic order in s-MFT

In this section we demonstrate that the free energy within the s-MFT treatment is $O(4)$ symmetric up to quartic order in the ψ_a 's. To do this, we expand the s-MFT free energy,

Eq. (B.3), in powers of h_i :

$$F = \sum_{n=0}^{\infty} \sum_i \frac{1}{n!} \left. \frac{\partial^n F}{\partial h_i^n} \right|_{h_i=0} h_i^n \quad (\text{B.26})$$

where h_i is defined in Eq. (B.5). Considering the pyrochlore structure, \sum_i is equivalent to $\sum_{\alpha=0}^3 \sum_{\mathbf{R}_i}$, where α is the sublattice label and \mathbf{R}_i is the FCC lattice position vector. As a result, h_i can be relabelled as $h^\alpha(\mathbf{R}_i)$. This notation makes the book-keeping clearer in what follows. We will focus on the $n = 4$ term because, based on our Ginzburg-Landau symmetry analysis in Chapter 4, the quadratic term is $O(4)$ invariant.

For $T \lesssim T_c$ and in a region of parameter space with $\{\frac{1}{2}\frac{1}{2}\frac{1}{2}\}$ ordering wave vectors, $\mathbf{h}^\alpha(\mathbf{R}_i)$ can be written as

$$\mathbf{h}^\alpha(\mathbf{R}_i) = \sum_a \hat{\psi}_a \mathbf{h}_{\mathbf{k}_a}(\mathbf{r}_i), \quad (\text{B.27})$$

where $\mathbf{r}_i = \mathbf{R}_i + \mathbf{r}^\alpha$. Using Eqs. (B.1, B.6, B.15) we have

$$\mathbf{h}_{\mathbf{k}_a}(\mathbf{r}_i) = |\mathbf{h}_{\mathbf{k}_a}(\mathbf{r}_i)| \hat{e}_{\mathbf{k}_a}^\alpha \cos(\mathbf{k}_a \cdot \mathbf{R}_i), \quad (\text{B.28})$$

where according to the arguments presented in Section B.2, $|\mathbf{h}_{\mathbf{k}_a}(\mathbf{r}_i)|$ is the same for all sites with nonzero moments. So $|\mathbf{h}_{\mathbf{k}_a}(\mathbf{r}_i)| \equiv h$. The fourth order term in h_i arising in Eq. (B.26), can be written as $\propto \sum_{\mathbf{R}_i} \sum_{\alpha=0}^3 |\mathbf{h}^\alpha(\mathbf{R}_i)|^4$. We now proceed to show that this term is $O(4)$ invariant.

Using Eqs. (B.27, B.28), we have:

$$\sum_{\mathbf{R}_i} \sum_{\alpha=0}^3 |\mathbf{h}^\alpha(\mathbf{R}_i)|^4 = \sum_{\mathbf{R}_i} \sum_{\alpha} h^4 \left(\sum_{b=0}^3 \hat{\psi}_b^2 + \sum_{b_1 < b_2} 2 \hat{\psi}_{b_1} \hat{\psi}_{b_2} \left(\hat{e}_{\mathbf{k}_{b_1}}^\alpha \cdot \hat{e}_{\mathbf{k}_{b_2}}^\alpha \right) \cos(\mathbf{k}_{b_1} \cdot \mathbf{R}_i) \cos(\mathbf{k}_{b_2} \cdot \mathbf{R}_i) \right)^2 \quad (\text{B.29})$$

$$\sum_{\mathbf{R}_i} \sum_{\alpha=0}^3 |\mathbf{h}^\alpha(\mathbf{R}_i)|^4 = \frac{N h^4}{4} \sum_{\alpha=0}^3 \left[\left(\sum_{b=0}^3 \hat{\psi}_b^2 \right)^2 + \sum_{b_1 < b_2} \hat{\psi}_{b_1}^2 \hat{\psi}_{b_2}^2 \right], \quad (\text{B.30})$$

$$\sum_{\mathbf{R}_i} \sum_{\alpha=0}^3 |\mathbf{h}^\alpha(\mathbf{R}_i)|^4 = \frac{3N h^4}{4 |\psi|^4} \left(\sum_{b=0}^3 \psi_b^2 \right)^2. \quad (\text{B.31})$$

In Eq. (B.29), we used the relation that $\hat{e}_{\mathbf{k}_{b_1}}^\alpha \cdot \hat{e}_{\mathbf{k}_{b_2}}^\alpha = -1/2$ for $b_1 \neq b_2 \neq \alpha$ (see Table B.1). We use momentum conservation going from Eq. (B.29) to Eq. (B.30). In Eq. (B.31), we used the relation $\psi_b = |\psi| \hat{\psi}_b$. N is the number of sites.

In consequence, the s-MFT free-energy is $O(4)$ invariant up to quartic order.

Appendix C

Second nearest-neighbour effect on the selection of partially ordered states at T_c^{MF}

Because they are often of considerable strength, we focused in the Chapter 4 on the dipole-induced (hhh) degeneracy-lifting into $(\frac{1}{2}\frac{1}{2}\frac{1}{2})$. Yet, there are some rare-earth pyrochlore oxides, such as $\text{Yb}_2\text{Ti}_2\text{O}_7$ and $\text{Pr}_2(\text{Sn,Zr})_2\text{O}_7$, where the magnetic moment is sufficiently small that the dipolar interactions, \mathcal{H}_{dip} , may not be the leading perturbation to \mathcal{H}_{nn} . Rather, the second nearest-neighbour interactions, \mathcal{H}_2 might well be. It is therefore of interest to consider the problem of the pyrochlore lattice with magnetic transition metal ions where dipolar interactions are definitely negligible compared to superexchange. We thus consider below the case $J_{\text{dip}} = 0$, but $J_2 \neq 0$. Also, for completeness, we consider a different, but equivalent, representation of the anisotropic exchange couplings in \mathcal{H}_{nn} [44].

The nearest-neighbour Hamiltonian, Eq. (4.1) in Chapter 4, can be linearly transformed to Eq. (5.1)(see Appendix F):

$$\begin{aligned} \mathcal{H}_{\text{nn}} = & \sum_{\langle i,j \rangle} \{ J_{zz} S_i^z S_j^z - J_{\pm} (S_i^+ S_j^- + S_i^- S_j^+) \\ & + J_{\pm\pm} (\gamma_{ij} S_i^+ S_j^+ + \gamma_{ij}^* S_i^- S_j^-) \\ & + J_{z\pm} [S_i^z (\zeta_{ij} S_j^+ + \zeta_{ij}^* S_j^-) + i \leftrightarrow j] \}, \end{aligned} \quad (\text{C.1})$$

where the 4×4 matrix ζ is given by [44]:

$$\zeta = \begin{pmatrix} 0 & -1 & e^{i\pi/3} & e^{-i\pi/3} \\ -1 & 0 & e^{-i\pi/3} & e^{i\pi/3} \\ e^{i\pi/3} & e^{-i\pi/3} & 0 & -1 \\ e^{-i\pi/3} & e^{i\pi/3} & -1 & 0 \end{pmatrix}, \quad (\text{C.2})$$

and $\gamma = -\zeta^*$. We note that the sublattice convention for the Hamiltonian of Eq. (C.1) and the definition of corresponding local coordinates are different from what were presented in Appendix A. The corresponding details are available in Ref. [44].

This representation has appeared in a number of recent publications on pyrochlore magnets [21, 44, 127]. In what follows, we first consider only a nearest-neighbour Hamiltonian, \mathcal{H}_{nn} . We identify the critical modes at T_c [57]. These modes specify the ordering wave vector that first become soft (critical) as the temperature is decreased. As discussed in the main body of the paper, we obtain a line-degeneracy with ordering wave vectors $\{hhh\}$ with arbitrary h in a certain region of the parameter space coloured dark in Fig. (C.1). Adding the beyond-nearest-neighbour interactions such as ferromagnetic second- and/or antiferromagnetic third-nearest-neighbours and/or long-range dipolar interaction, lifts this degeneracy and favours $\{\frac{1}{2}\frac{1}{2}\frac{1}{2}\}$ as ordering wave vectors [57, 82, 85, 86].

As stated above, we considered in the Chapter 4 long-range dipole-dipole interactions as a source of the selection of a $(\frac{1}{2}\frac{1}{2}\frac{1}{2})$ ordering wave vector. Here, we instead consider a ferromagnetic second nearest-neighbour interaction as perturbation. We repeat all calculations leading to the computation of the TAP correction Ω in Eq. (4.5). The results are illustrated in Fig. C.1. In this case, we observe regions corresponding to $\mathbf{k} = 0$ and $\mathbf{k} = (\frac{1}{2}\frac{1}{2}\frac{1}{2})$ ordering wave vectors. Using the E-TAP method, we identify subregions corresponding to $1\text{-}\mathbf{k}$ and $4\text{-}\mathbf{k}$ states in the $\mathbf{k} = (\frac{1}{2}\frac{1}{2}\frac{1}{2})$ region (see Fig. C.1 caption). The terms obtained in Eqs. (4.7, 4.8, 4.9) can raise/lower the free energy of the $1\text{-}\mathbf{k}$ state with respect to $4\text{-}\mathbf{k}$ thus breaking the degeneracy. We also, observe a region in parameter space in which the ordering wave vector is incommensurate (specified in Fig. C.1). The study of this region is beyond the scope of the present work.

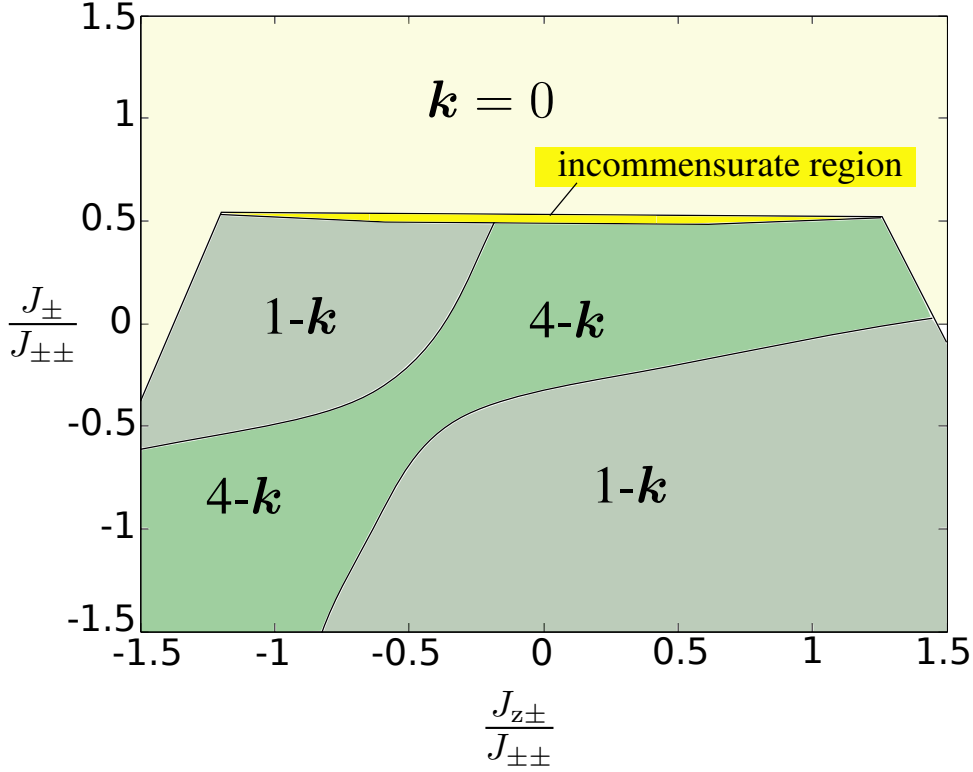


Figure C.1: Ordering wave vectors at $T = T_c$. The area denoted by $1\text{-}\mathbf{k}$ and $4\text{-}\mathbf{k}$ has $(\frac{1}{2}\frac{1}{2}\frac{1}{2})$ ordering wave vector. The first order E-TAP correction (Eq. (4.5)), leads to the selection of either a $4\text{-}\mathbf{k}$ or $1\text{-}\mathbf{k}$ state (with corresponding labeled regions in the phase diagram depending whether the free energy is lower for $4\text{-}\mathbf{k}$ or $1\text{-}\mathbf{k}$ ordered phase). This phase diagram corresponds to $\mathcal{H} = \mathcal{H}_{\text{nn}} + \mathcal{H}_2$ where $J_2/J_{\pm\pm} = -0.02$, $J_{zz} = 0$ and $\mathcal{H}_2 = \sum_{\langle\langle i,j \rangle\rangle} J_2 \mathbf{S}_i \cdot \mathbf{S}_j$.

Appendix D

ψ_2 and ψ_3 states

As stated in Chapters 5, the ψ_2 states have spin configurations with $\mathbf{k} = 0$ ordering wave vector and with the following spin orientations on a tetrahedron expressed in the global (Cartesian) reference frame

$$\hat{e}_0^1 = \frac{1}{\sqrt{6}}(-1, -1, 2) \quad (\text{D.1a})$$

$$\hat{e}_1^1 = \frac{1}{\sqrt{6}}(1, 1, 2) \quad (\text{D.1b})$$

$$\hat{e}_2^1 = \frac{1}{\sqrt{6}}(1, -1, -2) \quad (\text{D.1c})$$

$$\hat{e}_3^1 = \frac{1}{\sqrt{6}}(-1, 1, -2) \quad (\text{D.1d})$$

Here the subscripts correspond to sublattice labels in the pyrochlore lattice and the superscripts refer to different symmetry-related ψ_2 states. $\{\hat{e}_i^2\}$ and $\{\hat{e}_i^3\}$, $i = 0, \dots, 3$, can be obtained from Eq. (D.1) by C_3 rotations with respect to the $\langle 111 \rangle$ direction. ψ_3 states can be obtained from the ψ_2 ones, by a $\pi/6$ rotation of each spin about its local $[111]$ axis.

Appendix E

Diagrammatic Approach in E-TAP

In this appendix, we focus on the problem of the s-MFT $U(1)$ degeneracy of the Γ_5 manifold. Below, we calculate the degeneracy-lifting contributions from $\langle U^2 \rangle$ and $\langle U^2 T_2 \rangle$ in Eqs. (3.27b, 3.27d) which correspond to β^2 and β^4 terms in E-TAP expansion, to demonstrate the general idea of our diagrammatic method mentioned in Chapter 5. Higher order terms can be calculated using a similar procedure.

E.1 $\langle U^2 \rangle$ calculation

Using Eq. (3.25), we have

$$\langle U^2 \rangle = \frac{1}{2^2} \sum_{\langle i_1, j_1 \rangle} \sum_{\langle i_2, j_2 \rangle} J_{i_1 j_1}^{\alpha_1 \beta_1} J_{i_2 j_2}^{\alpha_2 \beta_2} \langle \delta S_{i_1}^{\alpha_1} \delta S_{j_1}^{\beta_1} \delta S_{i_2}^{\alpha_2} \delta S_{j_2}^{\beta_2} \rangle, \quad (\text{E.1})$$

where the summations are performed over lattice sites and summation is implied for Greek superscripts. To proceed, we need to specify all the possible pairings of the factors δS_{i_t} , δS_{j_t} , $t = 1, 2$ in the $\langle \delta S_{i_1}^{\alpha_1} \delta S_{j_1}^{\beta_1} \delta S_{i_2}^{\alpha_2} \delta S_{j_2}^{\beta_2} \rangle$. Considering Eq. (3.31), the only nonzero pairings of site indices in Eq. (E.1) are $i_1 = i_2$, $j_1 = j_2$ and $i_1 = j_2$, $j_1 = i_2$, with the constraint $i_1 \neq j_1$ and $i_2 \neq j_2$ imposed by the Hamiltonian; $J_{ii}^{\alpha\beta} = 0$ for all α and β . This leads to:

$$\langle U^2 \rangle = \frac{1}{2} \sum_{\langle i, j \rangle} J_{ij}^{\alpha_1 \beta_1} J_{ij}^{\alpha_2 \beta_2} \langle \delta S_i^{\alpha_1} \delta S_i^{\alpha_2} \rangle \langle \delta S_j^{\beta_1} \delta S_j^{\beta_2} \rangle. \quad (\text{E.2})$$

We now introduce a diagrammatic method to compute Eq. (E.2). In this equation, for a given i, j, α_t and β_t with $t = 1, 2$, $J_{ij}^{\alpha_1 \beta_1} J_{ij}^{\alpha_2 \beta_2} \langle \delta S_i^{\alpha_1} \delta S_i^{\alpha_2} \rangle \langle \delta S_j^{\beta_1} \delta S_j^{\beta_2} \rangle$ can be represented

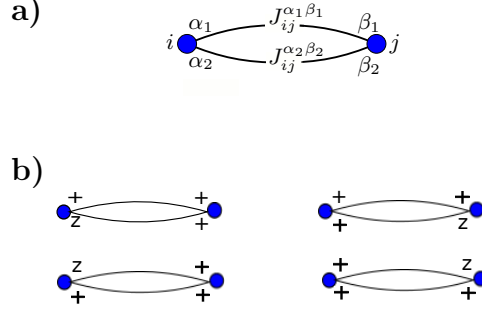


Figure E.1: **a)** Diagrammatic representation of the term $J_{ij}^{\alpha_1 \beta_1} J_{ij}^{\alpha_2 \beta_2} \langle \delta S_i^{\alpha_1} \delta S_i^{\alpha_2} \rangle \langle \delta S_j^{\beta_1} \delta S_j^{\beta_2} \rangle$ in Eq. (E.2). **b)** All diagrams corresponding to $\alpha_i, \beta_i = z, +$, $i = 1, 2$ with z appearing only once among the Greek superscripts. The same number of diagrams are present for the case where $\alpha_i, \beta_i = z, -$. Again z appears only once.

by a diagram of the form illustrated in Fig. E.1a. In this figure, the vertex labels match the labels of the lattice sites that the diagram covers. Each vertex represents an average of the form $\langle \delta S_i^{\alpha_1} \dots \delta S_i^{\alpha_t} \rangle$ where t is the number of bonds (solid lines) connected to that vertex. In the case of Eq. (E.2) as indicated in Fig. E.1a, the averages are $\langle \delta S_i^{\alpha_1} \delta S_i^{\alpha_2} \rangle$ and $\langle \delta S_j^{\beta_1} \delta S_j^{\beta_2} \rangle$. The bonds represent the elements of the coupling matrix, $J_{ij}^{\alpha \beta}$. It is straightforward combinatorics to take into account only the terms that contribute to the degeneracy-lifting factors, $\cos(3\phi)$ or $\cos(6\phi)$. We next proceed to demonstrate this point.

Based on the symmetry analysis of Section 5.2.1, $\langle U^2 \rangle$ can only contribute degeneracy-lifting terms of the general form of $m_z |m_{xy}|^3 \cos(3\phi)$ where the factor of $\cos(3\phi)$ is generated by the anisotropic couplings $j_{\pm\pm}$ and $j_{z\pm}$ in Eq. (5.1c). We recall that $j_{\pm\pm}$ and $j_{z\pm}$ each contributes a factor $e^{\pm 2i\phi}$ and $e^{\pm i\phi}$ in the power counting method. The $-2i\phi$ and $-i\phi$ corresponds to presence of $(\delta S^-)^2$ and δS^- in Eq. (E.2), respectively, which in turn, implies the presence of $J_{ij}^{- -} \equiv j_{\pm\pm} \gamma_{ij}^*$ or $J_{ij}^{z -} \equiv j_{z\pm} \zeta_{ij}^*$ matrix elements in $J_{ij}^{\alpha_1 \beta_1} J_{ij}^{\alpha_2 \beta_2} \langle \delta S_i^{\alpha_1} \delta S_i^{\alpha_2} \rangle \langle \delta S_j^{\beta_1} \delta S_j^{\beta_2} \rangle$. So for a given i and j , only the following combination of terms can generate $\cos(3\phi)$:

$$J_{ij}^{++} J_{ij}^{z+} \langle \delta S_i^+ \delta S_i^+ \rangle \langle \delta S_j^z \delta S_j^+ \rangle + J_{ij}^{--} J_{ij}^{z-} \langle \delta S_i^- \delta S_i^- \rangle \langle \delta S_j^z \delta S_j^- \rangle, \quad (\text{E.3})$$

where the first term generates the $e^{3i\phi}$ contribution to $\cos(3\phi)$ while the second term generates $e^{-3i\phi}$. All possible ways of generating the factor $e^{3i\phi}$ is illustrated in Fig. E.1b, which is the same as the number of ways of generating $e^{-3i\phi}$. Ultimately, Eq. (E.2) can be

rewritten as:

$$\langle U^2 \rangle = 2j_{\pm\pm}j_{z\pm} \left(\langle \delta S^z \delta S^+ \rangle \langle \delta S^+ \delta S^+ \rangle \sum_{ij} \gamma_{ij} \zeta_{ij} + \text{h.c.} \right). \quad (\text{E.4})$$

Based on Eqs. (3.33, 3.36) and recalling from Section 5.2 that \mathbf{m} and ϕ do not require site indices in the Γ_5 manifold, we dropped the site labels of δS 's in Eq. (E.2). The lattice sum, $\sum_{\langle i,j \rangle} \gamma_{ij} \zeta_{ij}$, can be carried out using a computer program for different lattice sizes with linear dimension L . Up to sixth order in the β expansion, the lattice sums *per site* for different terms in Eqs. (3.27) are independent of L for $L \geq 2$. Accordingly, we have

$$\frac{1}{N} \sum_{\langle i,j \rangle} \gamma_{ij} \zeta_{ij} = -6. \quad (\text{E.5})$$

Using Eqs. (3.33, 3.36), the averages in Eq. (E.4) can be written as

$$\langle \delta S^z \delta S^+ \rangle = \frac{18}{45} m_z m_+ + \dots \quad (\text{E.6})$$

$$\langle \delta S^+ \delta S^+ \rangle = \frac{18}{45} m_+^2 + \dots \quad (\text{E.7})$$

where to the lowest order of interest in \mathbf{m} which in this case is the fourth order according to GL analysis in Chapter 5, we keet $\lambda^\alpha \simeq 3m^\alpha$ and neglect all the higher order terms. Finally Eq. (E.4) gives

$$\begin{aligned} \langle U^2 \rangle / N &= (-0.96 m_z m_+^3 + \text{h.c.}) j_{\pm\pm} j_{z\pm} \\ &= -1.92 j_{\pm\pm} j_{z\pm} m_z |m_{xy}|^3 \cos(3\phi). \end{aligned} \quad (\text{E.8})$$

We note that Eq. (E.8) contributes to the g_0 in Eq. (5.6) which, in turn, is necessary to calculate $f(j_{\pm\pm}, j_{z\pm})$ in Eq. (5.10). All other terms in Eq. (3.27) involving solely powers of U and no T_n can be calculated in a similar way. The number of diagrams increases as one considers higher order terms in the β expansion of Eq. (5.9). As a result, finding the number and type of nonzero average of the form of Eq. (3.30) is most easily done using a computer program. The details of this type of calculations are presented in Section E.3. Some of the diagrams that appear at higher order in the β expansion are illustrated in Fig. E.2.

E.2 $\langle U^2 T_2 \rangle$ calculation

Due to the presence of T_n , in this case $n = 2$, this kind of averages need to be carried out slightly differently in comparison with averages containing only powers of U . The difference

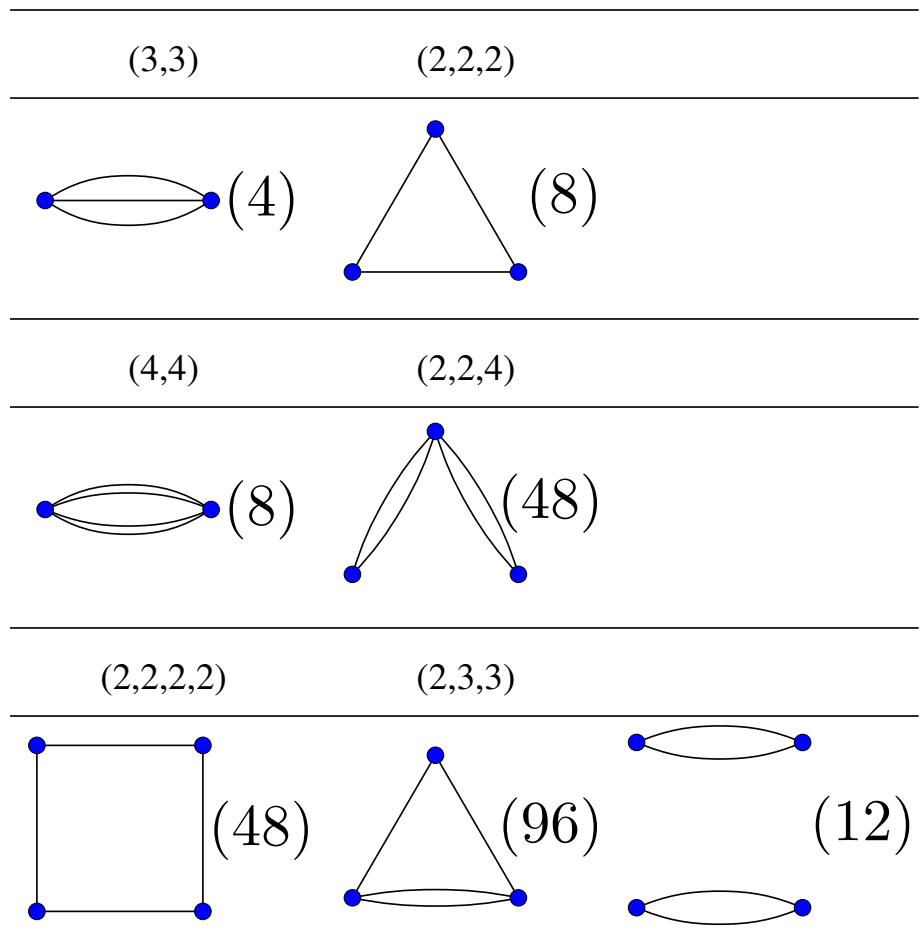


Figure E.2: The figure is made by of Alexander G. R. Day. For details, see the text in Section E.3. We also note that the contribution of disconnected diagrams (e.g. the diagram at the bottom right corner) in Eq. (3.27) adds up to zero.

comes from the presence of the factor $\partial^n \lambda_i / \partial \beta^n$ in Eq. (3.28). Considering Eq. (3.27a), we obtain the following relation

$$\frac{\partial \lambda^\alpha}{\partial \beta} = \frac{\partial \langle H \rangle}{\partial m^\alpha} = \frac{\partial^2 (\beta G(\beta))}{\partial m^\alpha \partial \beta}, \quad (\text{E.9})$$

From Eq. (E.9), one can write

$$\frac{\partial^n \lambda^\alpha}{\partial \beta^n} = \frac{\partial^{n+1} (\beta G(\beta))}{\partial m^\alpha \partial \beta^n}. \quad (\text{E.10})$$

Using Eq. (3.28), $\langle U^2 T_2 \rangle$ can therefore be written as:

$$\langle U^2 T_2 \rangle = \frac{1}{2^2} \sum_{i_1 j_1} \sum_{i_2 j_2} \sum_k J_{i_1 j_1}^{\alpha_1 \beta_1} J_{i_2 j_2}^{\alpha_2 \beta_2} \frac{\partial^2 \lambda_k^{\alpha_3}}{\partial \beta^2} \langle \delta S_{i_1}^{\alpha_1} \delta S_{j_1}^{\beta_1} \delta S_{i_2}^{\alpha_2} \delta S_{j_2}^{\beta_2} \delta S_k^{\alpha_3} \rangle. \quad (\text{E.11})$$

Using Eq. (E.10), we have

$$\frac{\partial^2 \lambda_k^{\alpha_3}}{\partial \beta^2} = \frac{\partial^3 (\beta G(\beta))}{\partial m^\alpha \partial \beta^2} = -\frac{\partial \langle U^2 \rangle}{\partial m^{\alpha_3}}. \quad (\text{E.12})$$

The term $\langle \delta S_{i_1}^{\alpha_1} \delta S_{j_1}^{\beta_1} \delta S_{i_2}^{\alpha_2} \delta S_{j_2}^{\beta_2} \delta S_k^{\alpha_3} \rangle$ in Eq. (E.11) can be dealt with as described previously in Section 3.3 in Chapter 3. The outcome reads

$$\langle \delta S_{i_1}^{\alpha_1} \delta S_{j_1}^{\beta_1} \delta S_{i_2}^{\alpha_2} \delta S_{j_2}^{\beta_2} \delta S_k^{\alpha_3} \rangle = 4 \langle \delta S_{i_1}^{\alpha_1} \delta S_{i_1}^{\alpha_2} \rangle \langle \delta S_k^{\alpha_3} \delta S_k^{\beta_1} \delta S_k^{\beta_2} \rangle, \quad (\text{E.13})$$

where the factor of 4 comes from the number of different ways of pairing site indices yielding non-vanishing results. On the other hand,

$$\langle U^2 \rangle = \frac{1}{2} \sum_{ij} J_{ij}^{\alpha_1 \beta_1} J_{ij}^{\alpha_2 \beta_2} \langle \delta S_i^{\alpha_1} \delta S_i^{\alpha_2} \rangle \langle \delta S_j^{\beta_1} \delta S_j^{\beta_2} \rangle, \quad (\text{E.14})$$

and, in turn,

$$\frac{\partial \langle U^2 \rangle}{\partial m_k^{\alpha_3}} = \frac{\partial \lambda_k^{\alpha_3}}{\partial m_k^{\alpha_3}} \sum_{ij} J_{ij}^{\alpha_1 \beta_1} J_{ij}^{\alpha_2 \beta_2} \frac{\partial \langle \delta S_i^{\alpha_1} \delta S_i^{\alpha_2} \rangle}{\partial \lambda_k^{\alpha_3}} \langle \delta S_j^{\beta_1} \delta S_j^{\beta_2} \rangle, \quad (\text{E.15})$$

where $\frac{\partial \lambda_k^{\alpha_3}}{\partial m_k^{\alpha_3}} \simeq 3$. Here, we ignored higher order terms which do not contribute to the degeneracy lifting terms of fourth or sixth order in components of \mathbf{m} . The $\frac{\partial \langle \delta S_i^{\alpha_1} \delta S_i^{\alpha_2} \rangle}{\partial \lambda_k^{\alpha_3}}$ expression can be calculated using Eq. (3.34). Substituting Eqs. (E.13, E.15) in Eq.

(E.11), we obtain the final expression which can be represented by a "fused" diagram shown in Fig. E.3. This diagram has a new type of vertex represented with a red square. This vertex is labeled with only one site index and its mathematical expression is:

$$\langle \delta S_k^{\alpha_3} \delta S_k^{\beta_1} \delta S_k^{\beta_2} \rangle \langle \delta S_k^{\alpha_3} \delta S_k^{\gamma_1} \delta S_k^{\gamma_2} \rangle, \quad (\text{E.16})$$

where again there is a sum over repeated Greek superscripts.

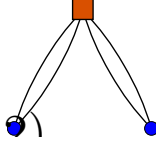


Figure E.3: The figure is made by of Alexander G. R. Day. Diagram corresponding to $\langle U^2 T_2 \rangle$. The vertex represented by red square represents the following: $\langle \delta S_k^{\alpha_3} \delta S_k^{\beta_1} \delta S_k^{\beta_2} \rangle \langle \delta S_k^{\alpha_3} \delta S_k^{\gamma_1} \delta S_k^{\gamma_2} \rangle$.

As a result, the final expression reads:

$$\langle U^2 T_2 \rangle = -\frac{\partial \lambda_k^{\alpha_3}}{\partial m_k^{\alpha_3}} \sum_{ijk} J_{ik}^{\alpha_1 \beta_1} J_{ik}^{\alpha_2 \beta_2} J_{jk}^{\alpha_3 \beta_3} J_{jk}^{\alpha_4 \beta_4} \langle \delta S_i^{\alpha_1} \delta S_i^{\alpha_2} \rangle \langle \delta S_k^{\alpha_3} \delta S_k^{\beta_1} \delta S_k^{\beta_2} \rangle \langle \delta S_k^{\alpha_3} \delta S_k^{\beta_3} \delta S_k^{\beta_4} \rangle \langle \delta S_j^{\alpha_3} \delta S_j^{\alpha_4} \rangle. \quad (\text{E.17})$$

From this point on, one can follow the procedure presented previously for the $\langle U^n \rangle$ terms to obtain the final results. All other averages similar to $\langle U^2 T_2 \rangle$ can be calculated following the above recipe.

E.3 On diagrams

In what follows, we make a few comments about different diagrams that appear in the E-TAP expansion.

First we focus on diagrams corresponding to $\langle U^n \rangle$ with $n = 2, 3, \dots$, in Eq. (3.27). The diagrams for $n = 3, 4$ are illustrated in Fig. E.2. In this figure, blue circles represent a given lattice site and the number of lines (bonds) connected to the circles is the number of paired δS 's at that lattice site. The connectivity indicated above each diagram is written in

the form of $(\alpha_1, \dots, \alpha_m)$ where m is the number of vertices and α_i is the number of bonds connected to vertex i . The number of times that each diagram appears in the process of pairing δS 's, referred to as diagram count, is indicated in parentheses to the right of each diagram in Fig. E.2. The diagrams are distinguished by their connectivity and their adjacency matrix eigenvalues [121]. The adjacency matrix M is a $m \times m$ matrix where m is the number of vertices appearing in the diagram. Its matrix elements M_{ij} ($0 < i, j \leq m$) corresponds to the number of bonds connecting the i -th vertex to the j -th vertex. We count these diagrams using a computer program in which we generate all possible diagrams given a certain number of vertices and a given connectivity. Then, we remove all diagrams that include any onsite interactions which are forbidden since there is no onsite interaction in the Hamiltonian of Eq. (5.1). For the remaining diagrams, we build their adjacency matrix which we then diagonalize. M is a symmetric matrix and thus has a set of real eigenvalues which defines a graph equivalence class. Graph with the same adjacency matrix eigenvalues correspond to graphs with the same topology. The number of graph with a given topology is noted in parentheses to the right of the graph in Fig. E.2.

The fifth and sixth order terms of the E-TAP expansion in β , contain, respectively, 9 and 26 types of connected diagrams. We note that the contribution of disconnected diagrams in Eq. (3.27) adds up to zero [121].

The so-called fused diagrams appear in terms of the form $\langle U^m T_n \rangle$ and $\langle T_n \rangle$, where $m, n \geq 2$ and are positive integers. They are constructed by fusing the diagrams similar to the ones in Fig. E.2 together. An example of such a diagram and the corresponding details of its definition is given in the caption of Fig E.3.

We also note that some of the diagrams do not cover lattice sites beyond one tetrahedron, for example the triangular diagram and the two site diagram in the top row of Fig. E.2.

Appendix F

Transformation Matrix Between Different Representations of mg-Hamiltonian

The Hamiltonians presented in Eqs. (4.1, 5.1) can be transformed to each other using the following linear transformation:

$$\begin{pmatrix} 1 & -10 & -2 & 4\sqrt{2} \\ 0 & -\frac{2}{3} & \frac{2}{3} & \frac{4\sqrt{2}}{3} \\ 0 & \frac{8}{3} & \frac{4}{3} & -\frac{4\sqrt{2}}{3} \\ 0 & 4\sqrt{2} & 0 & -2 \end{pmatrix} \begin{pmatrix} J_{zz} \\ J_{\pm} \\ J_{\pm\pm} \\ J_{z\pm} \end{pmatrix} = \begin{pmatrix} \mathcal{J}_{\text{Ising}} \\ \mathcal{J}_{\text{iso}} \\ \mathcal{J}_{\text{pd}} \\ \mathcal{J}_{\text{DM}} \end{pmatrix} \quad (\text{F.1})$$

where $\mathcal{J}_{\text{DM}} > 0$ corresponds to *indirect* DM interaction. We note that in order to derive this transformation matrix, one needs to take into account the proper sublattice convention and local coordinates definition for Eq. (5.1) presented in Ref. [44].

Part IV

Bibliography

Bibliography

- [1] N. W. Ashcroft and N. D. Mermin. *Solid State Physics*. Brooks/Cole Cengage Learning, 1976.
- [2] R. M. White. *Quantum theory of magnetism*. Springer, 1983.
- [3] L. Onsager. Crystal statistics. i. a two-dimensional model with an order-disorder transition. *Physical Review*, 65:117, 1944.
- [4] P. Stasiak. *Theoretical studies of frustrated magnets with dipolar interactions*. PhD thesis, University of Waterloo, 2009.
- [5] H. Nakayama, M. Althammer, Y.T. Chen, K. Uchida, Y. Kajiwara, D. Kikuchi, T. Ohtani, S. Geprägs, M. Opel, S. Takahashi, et al. Viewpoint: Insulating magnets control neighbors conduction. *Phys. Rev. Lett*, 110:206601, 2013.
- [6] N. Ohlsson, M. R. Krishna, and S. Kröll. Quantum computer hardware based on rare-earth-ion-doped inorganic crystals. *Optics communications*, 201:71, 2002.
- [7] J. Wesenberg and K. Mølmer. Robust quantum gates and a bus architecture for quantum computing with rare-earth-ion-doped crystals. *Physical Review A*, 68:012320, 2003.
- [8] J. H. Wesenberg, K. Mølmer, L. Rippe, and S. Kröll. Scalable designs for quantum computing with rare-earth-ion-doped crystals. *Physical Review A*, 75:012304, 2007.
- [9] B. Kraus, W. Tittel, N. Gisin, M. Nilsson, S. Kröll, and J.I. Cirac. Quantum memory for nonstationary light fields based on controlled reversible inhomogeneous broadening. *Physical Review A*, 73:020302, 2006.
- [10] L. Balents. Spin liquids in frustrated magnets. *Nature*, 464:199, 2010.

- [11] J. S. Gardner, M. J. P. Gingras, and J. E. Greedan. Magnetic pyrochlore oxides. *Rev. Mod. Phys.*, 82:53, 2010.
- [12] Toulouse G. *Commun Phys (London)*, 2:115, 1977.
- [13] J. Villain. Spin glass with non-random interactions. *Journal of Physics C: Solid State Physics*, 10:1717, 1977.
- [14] C. Lacroix, P. Mendels, and F. Mila, editors. *Introduction to Frustrated Magnetism*. Springer, 2011. Chapter 12.
- [15] R.M.F. Houtappel. Order-disorder in hexagonal lattices. *Physica*, 16(5):425 – 455, 1950.
- [16] G. H. Wannier. Antiferromagnetism. the triangular Ising net. *Phys. Rev.*, 79:357–364, 1950.
- [17] P. A. Lee, N. Nagaosa, and X.-G. Wen. Doping a mott insulator: Physics of high-temperature superconductivity. *Reviews of Modern Physics*, 78:17, 2006.
- [18] C. Lacroix, P. Mendels, and F. Mila. *Introduction to Frustrated Magnetism*. Springer, 2011. Chapter 1.
- [19] J. R. Stewart, G. Ehlers, A. S. Wills, S. T. Bramwell, and J. S. Gardner. Phase transitions, partial disorder and multi- k structures in $\text{Gd}_2\text{Ti}_2\text{O}_7$. *Journal of Physics: Condensed Matter*, 16:L321, 2004.
- [20] M. E. Zhitomirsky, M. V. Gvozdikova, P. C. W. Holdsworth, and R. Moessner. Quantum order by disorder and accidental soft mode in $\text{Er}_2\text{Ti}_2\text{O}_7$. *Phys. Rev. Lett.*, 109:077204, 2012.
- [21] L. Savary, K. A Ross, B. D. Gaulin, J. P. C. Ruff, and L. Balents. Order by quantum disorder in $\text{Er}_2\text{Ti}_2\text{O}_7$. *Physical review letters*, 109(16), 2012.
- [22] J. Villain, R. Bidaux, J.-P. Carton, and R. Conte. Order as an effect of disorder. *Journal de Physique*, 41:1263, 1980.
- [23] A. Niederberger. *Disorder-induced order with ultra-cold atoms*. PhD thesis, Institut de Ciéncias Fotòniques, 2010.
- [24] J. N. Reimers, A. J. Berlinsky, and A.-C. Shi. Mean-field approach to magnetic ordering in highly frustrated pyrochlores. *Phys. Rev. B*, 43:865, 1991.

- [25] C. L. Henley. Ordering due to disorder in a frustrated vector antiferromagnet. *Phys. Rev. Lett.*, 62:2056–2059, 1989.
- [26] T. Yildirim. Ordering due to disorder in frustrated quantum magnetic systems. *Turkish Journal of Physics*, 23:47, 1999.
- [27] E. F. Shender. *Sov. Phys. JETP*, 56:178, 1982.
- [28] M. Millonas, editor. *Fluctuations and Order*. Springer, 1996. Chapter 16.
- [29] S. Sachdev. Kagome and triangular lattice Heisenberg antiferromagnets: Ordering from quantum fluctuations and quantum-disordered ground states with unconfined bosonic spinons. *Phys. Rev. B*, 45:12377, 1992.
- [30] P. Stasiak, P. A. McClarty, and M. J. P. Gingras. Order-by-disorder in the xy pyrochlore antiferromagnet revisited. *ArXiv e-prints* , 2011.
- [31] A. W. C. Wong, Z. Hao, and M. J. P. Gingras. Ground state phase diagram of generic pyrochlore magnets with quantum fluctuations. *Phys. Rev. B*, 88:144402, 2013.
- [32] J. Oitmaa, R. R. P. Singh, B. Javanparast, A. G. R. Day, B. V. Bagheri, and M. J. P. Gingras. Phase transition and thermal order-by-disorder in the pyrochlore antiferromagnet $\text{Er}_2\text{Ti}_2\text{O}_7$: A high-temperature series expansion study. *Phys. Rev. B*, 88:220404, 2013.
- [33] H. Yan, O. Benton, L. D. C. Jaubert, and N. Shannon. Living on the edge: ground-state selection in quantum spin-ice pyrochlores. *ArXiv e-prints* , 2013.
- [34] G.-W. Chern. Pyrochlore antiferromagnet with antisymmetric exchange interactions: critical behavior and order from disorder. *arXiv preprint arXiv:1008.3038*, 2010.
- [35] B. Javanparast, Z. Hao, M. Enjalran, and M. J. P. Gingras. Fluctuation-driven selection at criticality in a frustrated magnetic system: the case of multiple-k partial order on the pyrochlore lattice. *ArXiv e-prints* , 2013.
- [36] M. R. Roser and L. R. Corruccini. Dipolar ferromagnetic order in a cubic system. *Phys. Rev. Lett.*, 65:1064–1067, 1990.
- [37] J. Jensen and A. R. Mackintosh. *Rare Earth Magnetism*. Clarendon Press. Oxford, 1991.

- [38] M. T. Hutchings. Point charge calculations of energy levels of magnetic ions in crystal electric fields. *Solid State Physics, Advances in Research and Application*, 16:227, 1964.
- [39] M. J. P. Gingras and P. A. McClarty. Quantum spin ice: A search for gapless quantum spin liquids in pyrochlore magnets. *ArXiv e-prints*, 2013.
- [40] P. Santini, S. Carretta, G. Amoretti, R. Caciuffo, N. Magnani, and G. H. Lander. Multipolar interactions in f-electron systems: The paradigm of actinide dioxides. *Rev. Mod. Phys.*, 81:807, 2009.
- [41] J. D. Thompson, P. A. McClarty, H. M. Rønnow, L. P. Regnault, A. Sørge, and M. J. P. Gingras. Rods of neutron scattering intensity in $\text{Yb}_2\text{Ti}_2\text{O}_7$: Compelling evidence for significant anisotropic exchange in a magnetic pyrochlore oxide. *Phys. Rev. Lett.*, 106:187202, 2011.
- [42] P. A. McClarty, S. H. Curnoe, and M. J. P. Gingras. Energetic selection of ordered states in a model of the $\text{Er}_2\text{Ti}_2\text{O}_7$ frustrated pyrochlore xy antiferromagnet. *Journal of Physics: Conference Series*, 145:012032, 2009.
- [43] M. Elhajal, B. Canals, R. Sunyer, and C. Lacroix. Ordering in the pyrochlore antiferromagnet due to Dzyaloshinsky-Moriya interactions. *Phys. Rev. B*, 71:094420, 2005.
- [44] K. A. Ross, L. Savary, B. D. Gaulin, and L. Balents. Quantum excitations in quantum spin ice. *Phys. Rev. X*, 1:021002, 2011.
- [45] S. H. Curnoe. Structural distortion and the spin liquid state in $\text{Tb}_2\text{Ti}_2\text{O}_7$. *Phys. Rev. B*, 78:094418, 2008.
- [46] H. R. Molavian, M. J. P. Gingras, and B. Canals. Dynamically induced frustration as a route to a quantum spin ice state in $\text{Tb}_2\text{Ti}_2\text{O}_7$ via virtual crystal field excitations and quantum many-body effects. *Phys. Rev. Lett.*, 98:157204, 2007.
- [47] T. Fennell, M. Kenzelmann, B. Roessli, M. K. Haas, and R. J. Cava. Power-law spin correlations in the pyrochlore antiferromagnet $\text{Tb}_2\text{Ti}_2\text{O}_7$. *Phys. Rev. Lett.*, 109:017201, 2012.
- [48] V. N. Glazkov, M. E. Zhitomirsky, A. I. Smirnov, H.-A. Krug von Nidda, A. Loidl, C. Marin, and J.-P. Sanchez. Single-ion anisotropy in the gadolinium pyrochlores studied by electron paramagnetic resonance. *Phys. Rev. B*, 72:020409, 2005.

- [49] M. R. Roser and L. R. Corruccini. Magnetic susceptibilities of rare-earth ions in an unusual tetrahedral site. *Phys. Rev. B*, 41:2359, 1990.
- [50] M. R. Roser, J. Xu, S. J. White, and L.R. Corruccini. Magnetic order in three rare-earth elpasolite compounds $\text{Cs}_2\text{NaRCl}_6$. *Physical Review B*, 45:12337, 1992.
- [51] K. R. Lea, M. J. M. Leask, and W. P. Wolf. The raising of angular momentum degeneracy of f-electron terms by cubic crystal fields. *Journal of Physics and Chemistry of Solids*, 23:1381, 1962.
- [52] C. J. O'Connor, R. L. Carlin, and R. W. Schwartz. Electron paramagnetic resonance study of Er^{3+} and Gd^{3+} in $\text{Cs}_2\text{NaLnCl}_6$. *J. Chem. Soc., Faraday Trans. 2*, 73:361, 1977.
- [53] B. D. Dunlap and G. K. Shenoy. Crystal-field analysis for the susceptibility of lanthanide compounds of the form $\text{Cs}_2\text{NaLnCl}_6$. *Physical Review B*, 12:2716, 1975.
- [54] W. Gong, H. Li, Z. Zhao, and J. Chen. Ultrafine particles of Fe, Co, and Ni ferromagnetic metals. *Journal of Applied Physics*, 69:5119, 1991.
- [55] M. Woińska, J. Szczytko, A. Majhofer, J. Gosk, K. Dziatkowski, and A. Twardowski. Magnetic interactions in an ensemble of cubic nanoparticles: A monte carlo study. *Physical Review B*, 88:144421, 2013.
- [56] M. Enjalran and M. J. P. Gingras. Theory of paramagnetic scattering in highly frustrated magnets with long-range dipole-dipole interactions: The case of the $\text{Tb}_2\text{Ti}_2\text{O}_7$ pyrochlore antiferromagnet. *Phys. Rev. B*, 70:174426, 2004.
- [57] M. Enjalran and M. J. P. Gingras. Theory of two-step magnetic ordering phenomena in a geometrically frustrated Heisenberg pyrochlore antiferromagnet with long range dipolar interactions. *ArXiv e-prints*, 2003.
- [58] D. P Landau and K. Binder. *A guide to Monte Carlo simulations in statistical physics*. Cambridge university press, 2009.
- [59] N. Metropolis, A. W. Rosenbluth, M. N. Rosenbluth, A. H. Teller, and E. Teller. Equation of state calculations by fast computing machines. *The journal of chemical physics*, 21:1087, 1953.
- [60] W. K. Hastings. Monte carlo sampling methods using markov chains and their applications. *Biometrika*, 57:97, 1970.

- [61] J. A. Olive, A. P. Young, and D. Sherrington. Computer simulation of the three-dimensional short-range Heisenberg spin glass. *Physical Review B*, 34:6341, 1986.
- [62] P. Stasiak and M. J. P. Gingras. Evidence for a finite-temperature spin glass transition in a diluted dipolar Heisenberg model in three dimensions. *arXiv preprint arXiv:0912.3469*, 2009.
- [63] E. Marinari and G. Parisi. Simulated tempering: A new monte carlo scheme. *Europhys. Lett.*, 19(451):451, 1992.
- [64] P. M. Chaikin and T. C. Lubensky. *Principles of Condensed Matter Physics*. Perseus Publishing, 1994. Chapter 5.
- [65] N. Goldenfeld. *Lectures on Phase Transitions and The Renormalization Group*. Cambridge University Press, 1992. Chapter 6, Sections 3 and 4.
- [66] D. J. Thouless, P. W. Anderson, and R. G. Palmer. Solution of a 'solvable model of a spin glass'. *Phil. Mag.*, 35:593, 1977.
- [67] M. Opper and D. Saad. *Advanced Mean Field Methods: Theory and Practice*. The MIT Press, 2001. Chapter 2.
- [68] A. Georges and J. S. Yedidia. How to expand around mean-field theory using high-temperature expansions. *J. Phys. A: Mathematical and General*, 24:2173, 1991.
- [69] A. G. Del Maestro. *Quantum Spin Fluctuations in the Heisenberg-Like Pyrochlore Antiferromagnet Gadolinium Titanate*. University of Waterloo, 2003.
- [70] J. Jensen and A. R. Mackintosh. *Rare Earth Magnetism: Structures and Excitations*. Clarendon Press, Oxford, 1991.
- [71] J. Rossat-Mignod. Magnetic structures. In K. Sköld and D. L. Price, editors, *Methods of Experimental Physics*, volume 23c, page 69. Academic Press, New York, 1987.
- [72] M. B. Salamon, Shantanu Sinha, J. J. Rhyne, J. E. Cunningham, Ross W. Erwin, Julie Borchers, and C. P. Flynn. Long-range incommensurate magnetic order in a dy-y multilayer. *Phys. Rev. Lett.*, 56:259, 1986.
- [73] T. Chattopadhyay. Modulated magnetic phases. *International Journal of Modern Physics B*, 7:3225, 1993.

- [74] A. Schröder, J. G. Lussier, B. D. Gaulin, J. D. Garrett, W. J. L. Buyers, L. Rebelsky, and S. M. Shapiro. Incommensurate magnetic order in the heavy fermion superconductor. *Phys. Rev. Lett.*, 72:136, 1994.
- [75] M. Raichle, M. Reehuis, G. André, L. Capogna, M. Sofin, M. Jansen, and B. Keimer. Incommensurate spin-density modulation in a copper oxide chain compound with commensurate charge order. *Phys. Rev. Lett.*, 101:047202, 2008.
- [76] E. M. Forgan, E. P. Gibbons, K. A. McEwen, and D. Fort. Observation of a quadruple-q magnetic structure in neodymium. *Phys. Rev. Lett.*, 62:470, 1989.
- [77] T. Okubo, Trung Hai Nguyen, and H. Kawamura. Cubic and noncubic multiple-q states in the Heisenberg antiferromagnet on the pyrochlore lattice. *Phys. Rev. B*, 84:144432, 2011.
- [78] A. Farkas, B. D. Gaulin, Z. Tun, and B. Briat. Magnetic phase transitions in CsCoBr₃. *Journal of Applied Physics*, 69:6167, 1991.
- [79] M. Mekata, N. Yaguchi, T. Takagi, T. Sugino, S. Mitsuda, H. Yoshizawa, N. Hosoi, and T. Shinjo. Successive magnetic ordering in CuFeO₂—a new type of partially disordered phase in a triangular lattice antiferromagnet. *Journal of the Physical Society of Japan*, 62:4474, 1993.
- [80] R. Movshovich, M. Jaime, S. Mentink, A. A. Menovsky, and J. A. Mydosh. Second low-temperature phase transition in frustrated UNi₄b. *Phys. Rev. Lett.*, 83:2065, 1999.
- [81] E. Granado, J. W. Lynn, R. F. Jardim, and M. S. Torikachvili. Two-dimensional magnetic correlations and partial long-range order in geometrically frustrated Sr₂YRuO₆. *Phys. Rev. Lett.*, 110:017202, 2013.
- [82] O. Cépas and B. S. Shastry. Field-driven transitions in the dipolar pyrochlore antiferromagnet Gd₂Ti₂O₇. *Phys. Rev. B*, 69:184402, 2004.
- [83] N. P. Raju, M. Dion, M. J. P. Gingras, T. E. Mason, and J. E. Greedan. Transition to long-range magnetic order in the highly frustrated insulating pyrochlore antiferromagnet Gd₂Ti₂O₇. *Phys. Rev. B*, 59:14489, 1999.
- [84] J. D. M. Champion, A. S. Wills, T. Fennell, S. T. Bramwell, J. S. Gardner, and M. A. Green. Order in the Heisenberg pyrochlore: The magnetic structure of Gd₂Ti₂O₇. *Phys. Rev. B*, 64:140407, 2001.

- [85] O. Cépas, A. P. Young, and B. S. Shastry. Degeneracy and strong fluctuation-induced first-order phase transition in the dipolar pyrochlore antiferromagnet. *Phys. Rev. B*, 72:184408, 2005.
- [86] A. S. Wills, M.E. Zhitomirsky, B. Canals, J. P. Sanchez, P. Bonville, P. Dalmas de Réotier, and A. Yaouanc. Magnetic ordering in $\text{Gd}_2\text{Sn}_2\text{O}_7$: the archetypal Heisenberg pyrochlore antiferromagnet. *Journal of Physics: Condensed Matter*, 18:L37, 2006.
- [87] A. P. Ramirez, B. S. Shastry, A. Hayashi, J. J. Krajewski, D. A. Huse, and R. J. Cava. Multiple field-induced phase transitions in the geometrically frustrated dipolar magnet: $\text{Gd}_2\text{Ti}_2\text{O}_7$. *Phys. Rev. Lett.*, 89:067202, 2002.
- [88] P. Bonville, J. A. Hodges, M. Ocio, J. P. Sanchez, P. Vulliet, S. Sosin, and D. Braithwaite. Low temperature magnetic properties of geometrically frustrated $\text{Gd}_2\text{Sn}_2\text{O}_7$ and $\text{Gd}_2\text{Ti}_2\text{O}_7$. *Journal of Physics: Condensed Matter*, 15:7777, 2003.
- [89] O. A. Petrenko, M. R. Lees, G. Balakrishnan, and D. McK Paul. Magnetic phase diagram of the antiferromagnetic pyrochlore $\text{Gd}_2\text{Ti}_2\text{O}_7$. *Phys. Rev. B*, 70:012402, 2004.
- [90] S. S. Sosin, L. A. Prozorova, A. I. Smirnov, A. I. Golov, I. B. Berkutov, O. A. Petrenko, G. Balakrishnan, and M. E. Zhitomirsky. Magnetocaloric effect in pyrochlore antiferromagnet $\text{Gd}_2\text{Ti}_2\text{O}_7$. *Phys. Rev. B*, 71:094413, 2005.
- [91] S. S. Sosin, L. A. Prozorova, A. I. Smirnov, A. I. Golov, I. B. Berkutov, O. A. Petrenko, G. Balakrishnan, and M. E. Zhitomirsky. Adiabatic demagnetization of a pyrochlore antiferromagnet $\text{Gd}_2\text{Ti}_2\text{O}_7$. *Journal of Magnetism and Magnetic Materials*, 290-291:709, 2005.
- [92] A. Yaouanc, P. Dalmas de Réotier, V. Glazkov, C. Marin, P. Bonville, J. A. Hodges, P. C. M. Gubbens, S. Sakarya, and C. Baines. Magnetic density of states at low energy in geometrically frustrated systems. *Phys. Rev. Lett.*, 95:047203, 2005.
- [93] P Dalmas de Réotier, V Glazkov, C Marin, A Yaouanc, PCM Gubbens, S Sakarya, P Bonville, A Amato, C Baines, and PJC King. Studies of $\text{R}_2\text{Ti}_2\text{O}_7$ (Gd and Yb); new results. *Physica B - Condensed Matter*, 374:145, 2006.
- [94] S. R. Dunsiger, R. F. Kiefl, J. A. Chakhalian, J. E. Greedan, W. A. MacFarlane, R. I. Miller, G. D. Morris, A. N. Price, N. P. Raju, and J. E. Sonier. Magnetic field dependence of muon spin relaxation in geometrically frustrated $\text{Gd}_2\text{Ti}_2\text{O}_7$. *Phys. Rev. B*, 73:172418, 2006.

- [95] Da-qian Liao, M. R. Lees, D. W. Baker, D. McK. Paul, and G. Balakrishnan. Magnetic order in geometrically frustrated $\text{Gd}_2(\text{Ti}_{1-x}\text{Zr}_x)_2\text{O}_7$ ($x= 0.02$ and 0.15) single crystals. *Phys. Rev. B*, 83:064403, 2011.
- [96] O. A. Petrenko, M. R. Lees, G. Balakrishnan, V. N. Glazkov, and S. S. Sosin. Transition to long-range magnetic order in the highly frustrated insulating pyrochlore antiferromagnet $\text{Gd}_2\text{Ti}_2\text{O}_7$. *Phys. Rev. B*, 85:180412, 2012.
- [97] J. S. Gardner, S. R. Dunsiger, B. D. Gaulin, M. J. P. Gingras, J. E. Greedan, R. F. Kiefl, M. D. Lumsden, W. A. MacFarlane, N. P. Raju, J. E. Sonier, I. Swainson, and Z. Tun. Cooperative paramagnetism in the geometrically frustrated pyrochlore antiferromagnet $\text{Tb}_2\text{Ti}_2\text{O}_7$. *Phys. Rev. Lett.*, 82:1012, 1999.
- [98] Sylvain Petit, Pierre Bonville, Julien Robert, Claudia Decorse, and Isabelle Mirebeau. Spin liquid correlations, anisotropic exchange, and symmetry breaking in $\text{Tb}_2\text{Ti}_2\text{O}_7$. *Phys. Rev. B*, 86:174403, 2012.
- [99] K. Fritsch, K. A. Ross, Y. Qiu, J. R. D. Copley, T. Guidi, R. I. Bewley, H. A. Dabkowski, and B. D. Gaulin. Antiferromagnetic spin ice correlations at $(1/2, 1/2, 1/2)$ in the ground state of the pyrochlore magnet $\text{Tb}_2\text{Ti}_2\text{O}_7$. *Phys. Rev. B*, 87:094410, 2013.
- [100] T. Taniguchi, H. Kadowaki, H. Takatsu, B. Fåk, J. Ollivier, T. Yamazaki, T. J. Sato, H. Yoshizawa, Y. Shimura, T. Sakakibara, T. Hong, K. Goto, L. R. Yaraskavitch, and J. B. Kycia. Coexisting magnetic order and cooperative paramagnetism in the stuffed pyrochlore $\text{Tb}_{2+x}\text{Ti}_{2-2x}\text{Nb}_x\text{O}_7$. *Phys. Rev. B*, 87:060408, 2013.
- [101] S. Guitteny, J. Robert, P. Bonville, J. Ollivier, C. Decorse, P. Steffens, M. Boehm, H. Mutka, I. Mirebeau, and S. Petit. Anisotropic propagative excitations and quadrupolar effects in $\text{Tb}_2\text{Ti}_2\text{O}_7$. *Phys. Rev. Lett.*, 111:087201, 2013.
- [102] A. Pelissetto and E. Vicari. Critical phenomena and renormalization-group theory. *Physics Reports*, 368:549, 2002.
- [103] M. Ferer, J. P. Van Dyke, and W. J. Camp. Effect of a cubic crystal field on the critical behavior of a 3d model with Heisenberg exchange coupling: A high-temperature series investigation. *Phys. Rev. B*, 23:2367, 1981.
- [104] K. E. Newman and E. K. Riedel. Cubic n -vector model and randomly dilute Ising model in general dimensions. *Phys. Rev. B*, 25:264, 1982.

- [105] M. Caselle and M. Hasenbusch. The stability of the $O(N)$ invariant fixed point in three dimensions. *Journal of Physics A: Mathematical and General*, 31:4603, 1998.
- [106] J. M. Carmona, A. Pelissetto, and E. Vicari. n -component Ginzburg-Landau hamiltonian with cubic anisotropy: A six-loop study. *Phys. Rev. B*, 61:15136, 2000.
- [107] K. Binder. Theory of first-order phase transitions. *Reports on Progress in Physics*, 50:783, 1987.
- [108] T. Plefka. Convergence condition of the tap equation for the infinite-ranged Ising spin glass model. *Journal of Physics A: Mathematical and General*, 15:1971, 1982.
- [109] M. J. P. Gingras, B. C. den Hertog, M. Faucher, J. S. Gardner, S. R. Dunsiger, L. J. Chang, B. D. Gaulin, N. P. Raju, and J. E. Greedan. Thermodynamic and single-ion properties of Tb^{3+} within the collective paramagnetic-spin liquid state of the frustrated pyrochlore antiferromagnet $Tb_2Ti_2O_7$. *Phys. Rev. B*, 62:6496, 2000.
- [110] Ross Stewart, private communication.
- [111] A. Poole, A. S. Wills, and E. Lelievre-Berna. Magnetic ordering in the xy pyrochlore antiferromagnet $Er_2Ti_2O_7$: a spherical neutron polarimetry study. *Journal of Physics: Condensed Matter*, 19(45):452201, 2007.
- [112] J. D. M. Champion, M. J. Harris, P. C. W. Holdsworth, A. S. Wills, G. Balakrishnan, S. T. Bramwell, E. Čížmár, T. Fennell, J. S. Gardner, J. Lago, D. F. McMorrow, M. Orendáč, A. Orendáčová, D. McK. Paul, R. I. Smith, M. T. F. Telling, and A. Wildes. $Er_2Ti_2O_7$: Evidence of quantum order by disorder in a frustrated antiferromagnet. *Phys. Rev. B*, 68:020401, 2003.
- [113] J. D. M. Champion and P. C. W. Holdsworth. Soft modes in the easy plane pyrochlore antiferromagnet. *Journal of Physics: Condensed Matter*, 16:S665, 2004.
- [114] J. P. C. Ruff, J. P. Clancy, A. Bourque, M. A. White, M. Ramazanoglu, J. S. Gardner, Y. Qiu, J. R. D. Copley, M. B. Johnson, H. A. Dabkowska, and B. D. Gaulin. Spin waves and quantum criticality in the frustrated xy pyrochlore antiferromagnet $Er_2Ti_2O_7$. *Phys. Rev. Lett.*, 101:147205, 2008.
- [115] P. Dalmas de Réotier, A. Yaouanc, Y. Chapuis, S. H. Curnoe, B. Grenier, E. Ressouche, C. Marin, J. Lago, C. Baines, and S. R. Giblin. Magnetic order, magnetic correlations, and spin dynamics in the pyrochlore antiferromagnet $Er_2Ti_2O_7$. *Phys. Rev. B*, 86:104424, 2012.

- [116] C. Pinettes, B. Canals, and C. Lacroix. Classical Heisenberg antiferromagnet away from the pyrochlore lattice limit: Entropic versus energetic selection. *Phys. Rev. B*, 66:024422, 2002.
- [117] H. R. Molavian, P.A. McClarty, and M. J. P. Gingras. Towards an effective spin hamiltonian of the pyrochlore spin liquid Tb₂Ti₂O₇. *ArXiv e-prints*, 2009.
- [118] L. Savary and L. Balents. Coulombic quantum liquids in spin-1/2 pyrochlores. *Phys. Rev. Lett.*, 108:037202, 2012.
- [119] J. Lou, A. W. Sandvik, and L. Balents. Emergence of $u(1)$ symmetry in the 3d xy model with Z_q anisotropy. *Phys. Rev. Lett.*, 99:207203, 2007.
- [120] D. J. Thouless, P. W. Anderson, and R. G. Palmer. Solution of 'solvable model of a spin glass'. *Philosophical Magazine*, 35:593, 1977.
- [121] J. Oitmaa, C. Hamer, and W. Zheng. *Series Expansion Methods For Strongly Interacting Lattice Models*. Cambridge University Press, 2006.
- [122] R. Siddharthan, B. S. Shastry, A. P. Ramirez, A. Hayashi, R. J. Cava, and S. Rosenkranz. Ising pyrochlore magnets: Low-temperature properties, ice rules, and beyond. *Phys. Rev. Lett.*, 83:1854, 1999.
- [123] J. P. Bouchaud and P. G. Z erah. Dipolar ferromagnetism: a monte carlo study. *Phys. Rev. B*, 47:9095, 1993.
- [124] M. H. Cohen and F. Keffer. Dipolar ferromagnetism at 0k. *Phys. Rev.*, 99:1135–1140, 1955.
- [125] M. Plischke and B. Bergersen. *Equilibrium statistical physics*. World Scientific, 2006.
- [126] A. Auerbach. *Interacting electrons and quantum magnetism*. Springer, 1994.
- [127] S.-B. Lee, S. Onoda, and L. Balents. Generic quantum spin ice. *Phys. Rev. B*, 86:104412, 2012.